DISSERTATION

Scalable Parallel
Micromagnetic Solvers
for Magnetic Nanostructures

ausgeführt zum Zwecke der Erlangung des akademischen Grades
eines Doktors der technischen Wissenschaften

unter der Leitung von
Univ.Prof. Dipl.-Ing. Dr.techn. Josef Fidler und
Univ.Doz. Dipl.-Ing. Dr.techn. Thomas Schrefl
Institut für Festkörperphysik / E138

eingereicht an der Technischen Universität Wien
Fakultät für Naturwissenschaften und Informatik

durch

Werner Scholz
Matr.Nr. 9426502
Wiedner Hauptstraße 79/4
1040 Wien

Wien, am 18. Februar 2003   _____

Abstract

A parallel finite element micromagnetics package has been implemented, which is highly scalable, easily portable and combines different solvers for the micromagnetic equations. The implementation is based on the standard Galerkin discretization on tetrahedral meshes with linear basis functions. A static energy minimization, a dynamic time integration and the nudged elastic band method have been implemented.

The static energy minimization method is used for the investigation of domain wall pinning processes in SmCo permanent magnets. The pinning of magnetic domain walls on the precipitation structure and the influence of material parameters, cell structure, and cell geometry are studied in detail. The thickness of the coherent precipitation plays an important role, since it has to be thicker than the domain wall width for effective pinning, but it must not be too thick, which would allow the reversal of the whole intercellular structure. Nucleation and magnetization reversal processes in FePt nanoparticles are investigated for particles with single and multiple easy axes. The results show a strong reduction of coercivity if more misaligned easy axes within a particle are assumed and the particle size is reduced.

The static as well as the dynamic properties of the magnetic vortex state of soft magnetic nanodots are studied using the time integration of the dynamic Landau-Lifshitz-Gilbert equation. A phase diagram of the magnetic ground state of magnetic nanodots has been obtained and a comparison with an analytical vortex model and experimental results is given. Vortex precession and radial excitation modes are calculated and their eigenfrequencies measured. Finally, the properties of elliptical and rectangular permalloy nanoparticles are studied. The shape and the demagnetizing field play an important role in the magnetization reversal process. In chains of these particles magnetostatic coupling leads to stable magnetization configurations with antiparallel magnetization in neighboring particles.

Kurzfassung

Ein paralleles finite Elemente Programmpaket für mikromagnetische Probleme wurde implementiert, das sehr effizient skaliert, leicht portierbar ist und verschiedene Lösungsverfahren für die mikromagnetischen Gleichungen kombiniert. Die Implementierung basiert auf der Galerkin Diskretisierung auf Tetraedergittern mit linearen Basisfunktionen. Eine statische Energieminimierungs-, eine dynamische Zeitintegrations- und eine Gummibandmethode wurden implementiert.

Die statische Energieminimierungsmethode wurde für die Untersuchung des Domänenwandhaftens in SmCo Permanentmagneten verwendet. Das Haften magnetischer Domänenwände an der Ausscheidungsphase und der Einfluß der Materialparameter, der Zellstruktur und der Zellgeometrie werden detailliert erörtert. Die Dicke der Ausscheidungsphase spielt eine wichtige Rolle, da sie für effektives Haften einerseits dicker als die Domänenwandbreite sein muß, aber andererseits nicht zu dick sein darf, um nicht ein vollständiges Ummagnetisieren der Zwischenphase zu ermöglichen. Nukleations und Ummagnetisierungsprozesse in FePt Nanoteilchen mit einer und mehreren leichten Richtungen werden untersucht. Die Ergebnisse zeigen eine starke Reduktion des Koerzitivfeldes, wenn mehrere verdrehte leichte Achsen innerhalb eines Teilchens angenommen werden und die Teilchengröße reduziert wird.

Die statischen und dynamischen Eigenschaften von magnetischen Wirbelzuständen in weichmagnetischen scheibchenförmigen Nanoteilchen werden mit Hilfe der Integration der Landau-Lifshitz-Gilbert Gleichung untersucht. Ein Phasendiagramm der magnetischen Grundzustände der Nanoteilchen wird erstellt und Vergleiche mit einem analytischen Modell und experimentellen Untersuchungen durchgeführt. Vortex-Präzessions- und radiale Moden werden berechnet und ihre Eigenfrequenzen bestimmt. Schließlich werden die Eigenschaften von elliptischen und rechteckigen Nanoteilchen studiert. Die Form und das entmagnetisierende Feld spielen eine wichtige Rolle beim Ummagnetisierungsprozeß. In Ketten von solchen Teilchen führt magnetostatische Kopplung zu stabilen Magnetisierungskonfigurationen mit antiparalleler Magnetisierung in benachbarten Teilchen.

Contents

Introduction

The effects of magnetism and magnetic materials have been exploited since the invention of the magnetic compass for navigation in the 10th century in China. It took until the 13th century, that this commercially and strategically important tool became known in Europe, and Charles Augustine de Coulomb made the first quantitative investigations only in the 18th century. However, after the pioneering work of Ampère and Faraday and the formulation of the theory of electrodynamics by Maxwell many new applications emerged.

The progress in the field of permanent magnets is very well illustrated by the maximum energy density product $(BH)_{max}$. By the end of the 19th century magnetic steels with a $(BH)_{max} \approx 2$ kJ/m^3 were available. AlNiCo precipitation hardened magnets, which were discovered by Mishima in 1931, lead to energy density products as high as 90 kJ/m^3 by 1955. After the second world war hardferrites (ceramic oxides) were developed, and they are still commonly used because of the great abundance of their raw materials and low price. A major breakthrough was the discovery of magnetocrystalline anisotropy in rare-earth intermetallic compounds in the 1960s. Strnat et al. [1] found, that the combination of the high magnetic moment of iron and cobalt together with the high magnetocrystalline anisotropy caused by rare-earth elements gives permanent magnetic materials with excellent properties and energy density products of up to 90 kJ/m^3. Especially SmCo based materials retain a high magnetic ordering temperature, which makes them suitable for high temperature applications. Therefore, the HITEMAG project [2], whose aim is the development and optimization of permanent magnetic materials for application temperatures of up to 500 °C, concentrated on SmCo based precipitation hardened materials. As part of this project micromagnetic simulations have been carried out and the results are

presented in Sec. 7.

The highest energy density products so far have been obtained with rare-earth iron based permanent magnets. In 1984 Sagawa et al. [3], Croat et al. [4] and Hadjipanayis et al. [5] obtained energy density products of up to 300 kJ/m^3 for a material based on $Nd_2Fe_{14}B$. In the following years continuing improvement of the production route has resulted in energy density products in excess of 400 kJ/m^3 [6].

A very similar development can be observed in the area of magnetic recording. In 1956 IBM introduced the 305 RAMAC (Random Access Method for Accounting and Control) with a capacity of 5 MB. It was the first magnetic storage device, which stored digital information by writing magnetization patterns on a "hard disk" with a thin film of granular magnetic material instead of magnetic tapes. One of the major advantages was, that any position on the disk could be directly accessed by the read/write heads and it was not necessary to wind a tape any more. Since then many new discoveries and developments have improved computer hard disks.

The areal density determines the amount of information, which can be stored on a given area of a hard disk. This figure of merit measures the performance of hard disk media in a similar way like the energy density product for permanent magnetic materials discussed above. And it has shown a similar development during the last 20 years.

In 1985 the typical areal density in mass production was 20 MB/in^2 (megabits per square inch). The industry trend showed a typical increase of about 27 % per year. In 1992 it exceeded 100 MB/in^2 and the annual growth rate jumped to approximately 50 % per year. Starting with the introduction of giant magnetoresistive read-write heads in 1997 the areal density has been doubling every year [7]. Present-day drives have an areal density of about 30 GB/in^2 and read-write heads based on the extraordinary magnetoresistance effect will allow data densities beyond 100 GB/in^2 [8, 9].

As an alternative to these thin film granular magnetic storage media ferromagnetic nanostructures are considered for the basic information storage elements in magnetic random access memories (MRAM), high density magnetic storage media, and magnetic sensors. These structures can be produced using well established techniques for semiconductors but they have several ad-

vantages over today's semiconductor based materials including nonvolatility, nondestructive readout, radiation hardness, low voltage, and unlimited read and write endurance [10, 11]. Therefore, the magnetic properties, switching behavior, and switching dynamics of magnetic nanostructures are of great interest, and the results for cylindrical nanodots and elliptical nanoelements are presented in Sec. 9 and Sec. 10, respectively.

Both research areas, permanent magnets and magnetic storage media, have made tremendous progress during the last decades and they have become key technologies in today's information society. In order to keep the pace of these developments and push the limits, many research projects are carried out worldwide and this thesis is one small contribution.

Chapter 1

Motivation

The properties of modern magnetic materials are strongly influenced by their microstructure. The continuing improvement of the properties of SmCo based magnets has been made possible by additives like Cu and Zr and a refined processing route and heat treatment, which have a great impact on the resulting cellular precipitation structure [12]. The typical size of the cells is in the order of 100 nm with an intercellular phase of around 10 nm. The particle size in magnetic recording tapes is of the same order of magnitude. The typical grain size in current hard disk storage media is about 8 nm with an intergranular region of about 2 nm for exchange decoupling of the grains.

These structures are so small that quantum mechanical effects like exchange have to be taken into account. However, they are too large for a pure quantum mechanical description, which would exceed the capabilities of today's ab-initio computational models. On this intermediate level between the macroscopic world and a description with atomic resolution, micromagnetic models have proved to be a useful tool [13]. These computational models provide great freedom in the choice of experiment conditions and in the variation of material parameters. In addition to measurements of the remanent magnetization and the coercive field, it is possible to study the details of the magnetization distribution and the magnetization reversal processes, which are difficult to investigate experimentally. In this thesis temperature dependent effects have not been considered explicitly, but they are included in the temperature dependent material parameters. Also eddy current effects,

which should be taken into account in materials with high conductivity and in high speed switching experiments, are only implicitly included in the Gilbert damping constant.

In various fields of computer aided engineering like structural analysis, fluid dynamics, and electromagnetic field computation, as well as micromagnetics [14] the finite element method has been successfully applied. Especially its flexibility in modeling arbitrary geometries has made it very popular. In the light of the importance of the microstructure of magnetic materials the finite element method has been chosen for the implementation of a micromagnetic model.

There are several commercial and open source micromagnetics packages available (cf. App. A), however all of them use the finite difference method. In addition, the work on this thesis required static energy minimization methods for the study of SmCo permanent magnets as well as dynamic time integration methods for the investigation of the magnetization dynamics in magnetic nanoparticles.

Therefore, a finite element micromagnetics package has been implemented which combines several unique features:

It is

- entirely based on portable, free, open source software packages,

- highly portable to different hardware platforms, which range from simple PCs to massively parallel supercomputers,

- highly optimized and scalable,

- well integrated, combining static energy minimization, dynamic time integration, and nudged elastic band methods.

An introduction to the finite element method is given in chapter 2. The basic micromagnetic equations and their discretization in the context of the finite element method are outlined in chapter 3, while the appropriate solution methods are described in chapter 4. The details of the implementation of the micromagnetics package are discussed in chapter 5 and the optimization strategies are explained in chapter 6.

This micromagnetics model has been applied to study domain wall pinning effects in SmCo permanent magnets. The results are presented in chapter 7. Nucleation and magnetization reversal processes in FePt nanoparticles for magnetic storage media are studied in chapter 8, while the static and dynamic properties of permalloy nanodots are investigated in chapter 9. Finally, in chapter 10 the properties of elliptical and rectangular permalloy nanoparticles and the influence of magnetostatic coupling in chains of particles are examined. This thesis is completed by an appendix including a list of publicly available micromagnetics packages, the list of software packages, which has been used for the implementation of the parallel code, and a list of typical material parameters.

Chapter 2

The Finite Element Method

For the calculation of the demagnetizing field a hybrid finite element/ boundary element method is used as explained in Sec. 3.4. This method requires the solution of a Poisson and a Laplace equation. Therefore the former is used in this chapter as an example for a short introduction to the finite element method [15].

2.1   Poisson Problem

We want to calculate a numerical solution U, which approximates the true solution u of the Poisson (boundary value) problem (P) in the solution domain $\Omega \subset \mathbb{R}^3$ with closed boundary Γ. Dirichlet boundary conditions apply on $\Gamma_D \subset \Gamma$ and Neumann boundary conditions apply on $\Gamma_N := \Gamma \backslash \Gamma_D$.

The Poisson problem (P) is defined as follows: Given $f \in L^2(\Omega)$, $u_D \in H^1(\Omega)$, and $g \in L^2(\Gamma_N)$, we are searching for the solution $u \in H^1(\Omega)$, which satisfies the Poisson equation

$$-\Delta u = f \quad \text{in } \Omega \tag{2.1}$$

with Dirichlet boundary conditions

$$u = u_D \quad \text{on } \Gamma_D \tag{2.2}$$

and Neumann boundary conditions

$$\frac{\partial u}{\partial n} = g \quad \text{on } \Gamma_N \quad . \tag{2.3}$$

2.2   The Weak Formulation

The weak formulation of the boundary value problem (P) is then obtained by the multiplication of Eq. (2.1) with $w \in H_D^1(\Omega) := \{w \in H^1(\Omega)|w = 0 \text{ on } \Gamma_D\}$ and integration over Ω:

$$-\int_\Omega \Delta u \cdot w \, dv = \int_\Omega f \cdot w \, dv \quad . \tag{2.4}$$

Integration by parts gives

$$\int_\Omega \nabla u \cdot \nabla w \, dv - \int_{\Gamma_N} \frac{\partial u}{\partial n} \cdot w \, da = \int_\Omega f \cdot w \, dv \tag{2.5}$$

and substitution of the boundary conditions and rearrangement leads to

$$\int_\Omega \nabla u \cdot \nabla w \, dv = \int_\Omega f \cdot w \, dv + \int_{\Gamma_N} g \cdot w \, da \quad . \tag{2.6}$$

Now we incorporate the (possibly inhomogeneous) Dirichlet boundary conditions

$$\int_\Omega \nabla u \cdot \nabla w \, dv - \int_\Omega \nabla u_D \cdot \nabla w \, dv = \int_\Omega f \cdot w \, dv + \int_{\Gamma_N} g \cdot w \, da - \int_\Omega \nabla u_D \cdot \nabla w \, dv \tag{2.7}$$

and substitute the homogeneous solution $v \in H_D^1(\Omega)$, which is given by $v = u - u_D$ and satisfies $v = 0$ on Γ_D. This gives us the weak formulation of the Poisson problem P which reads: Find $v \in H_D^1(\Omega)$ such that

$$\int_\Omega \nabla v \cdot \nabla w \, dv = \int_\Omega f \cdot w \, dv + \int_{\Gamma_N} g \cdot w \, da - \int_\Omega \nabla u_D \cdot \nabla w \, dv \quad . \tag{2.8}$$

2.3   Galerkin Discretization

In order to solve the Poisson problem numerically we have to discretize the weak formulation of the Poisson equation (Eq. (2.8)) and restrict the solution space of the numerical solution U to a finite dimensional subspace S of $H^1(\Omega)$. Accordingly $U_D \in S_D := S \cap H_D^1$ approximates u_D on Γ_D. The discretized problem P_S can then be written as: Find $V \in S_D$ such that

$$\int_\Omega \nabla V \cdot \nabla W \, dv = \int_\Omega f \cdot W \, dv + \int_{\Gamma_N} g \cdot W \, da - \int_\Omega \nabla U_D \cdot \nabla W \, dv \quad (2.9)$$

with $W \in S_D$.

If we assume that $(\eta_1, \ldots, \eta_N)$ is a basis of the N-dimensional space S and $S_D := S \cap H_D^1$ a M-dimensional subspace then we can rewrite Eq. (2.9)

$$\int_\Omega \nabla V \cdot \nabla \eta_j \, dv = \int_\Omega f \cdot \eta_j \, dv + \int_{\Gamma_N} g \cdot \eta_j \, da - \int_\Omega \nabla U_D \cdot \nabla \eta_j \, dv \, (\eta_j \in S_D) \quad .$$
$$(2.10)$$

If we now make a series expansion of V and U_D in terms of η_k

$$V = \sum_{k=1}^M x_k \eta_k \, (\eta_k \in S_D) \quad \text{and} \quad U_D = \sum_{k=1}^N U_k \eta_k \, (\eta_k \in S) \quad , \quad (2.11)$$

then we obtain

$$\int_\Omega \nabla \sum_k x_k \eta_k \cdot \nabla \eta_j \, dv = \int_\Omega f \cdot \eta_j \, dv + \int_{\Gamma_N} g \cdot \eta_j \, da - \int_\Omega \nabla \sum_{k=1}^N U_k \eta_k \cdot \nabla \eta_j \, dv$$
$$(2.12)$$

which can be rewritten as

$$\sum_k x_k \int_\Omega \nabla \eta_k \cdot \nabla \eta_j \, dv = \int_\Omega f \cdot \eta_j \, dv + \int_{\Gamma_N} g \cdot \eta_j \, da - \sum_{k=1}^N U_k \int_\Omega \nabla \eta_k \cdot \nabla \eta_j \, dv$$
$$(2.13)$$

and finally simplified to a system of linear equations

$$Ax = b \quad (2.14)$$

where the "stiffness matrix" is given by

$$A_{jk} = \int_{\Omega} \nabla \eta_j \cdot \nabla \eta_k \, dv \qquad (2.15)$$

and the "right hand side" by

$$b_j = \int_{\Omega} f \cdot \eta_j \, dv + \int_{\Gamma_N} g \cdot \eta_j \, da - \sum_{k=1}^{N} U_k \int_{\Omega} \nabla \eta_k \cdot \nabla \eta_j \, dv \quad . \qquad (2.16)$$

The stiffness matrix is sparse, symmetric, and positive definite. Thus, Eq. (2.14) has exactly one solution $x \in \mathbb{R}^M$, which gives the Galerkin solution

$$U = U_D + V = \sum_{j=1}^{N} U_j \eta_j + \sum_{k=1}^{M} x_k \eta_k \quad . \qquad (2.17)$$

2.4 Mesh Generation

The finite element method requires the discretization of the spatial domain Ω with "finite elements" – a regular triangulation $\mathcal{T}$. For two dimensional problems triangles and rectangles, in three dimensions tetrahedral (cf. Fig. 2.1) and hexahedral elements are commonly used. Also a mixture of different types of elements is possible, but after the evaluation of various other implementations and for simplicity a tetrahedral discretization has been implemented.

As compared to finite difference methods [17] the finite element mesh may be entirely unstructured, which makes the modeling of complicated geometries and irregular microstructures more convenient. Still, a "regular" triangulation of a three dimensional body of arbitrary shape with tetrahedral elements is required to meet several conditions, which have been defined by Ciarlet [18]:

- The nodes of the mesh lie on the vertices of the tetrahedra.

- The elements of the triangulation do not overlap.

- No node lies on an edge of a tetrahedron.
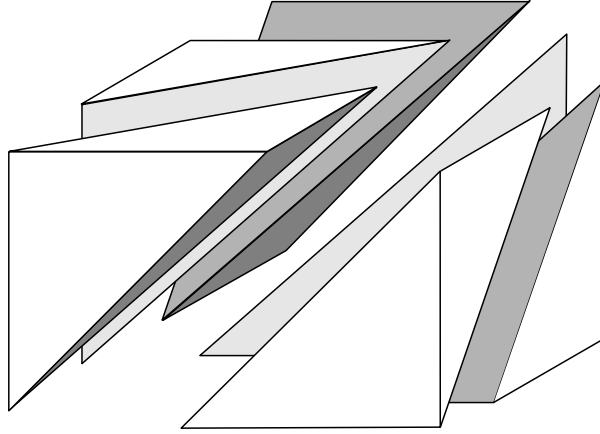
Figure 2.1: Kuhn triangulation of a cube into six tetrahedral finite elements (exploded view) [16].

- Each face on the surface of the body belongs either to Γ_D or Γ_N.

If we assume, that the domain Ω has a surface Γ of flat polygons, it is possible to find a triangulation $\mathcal{T}$ with (tetrahedral) finite elements T, which cover Ω:

$$\Omega = \bigcup_{T \in \mathcal{T}} T \tag{2.18}$$

However, the creation of the geometrical model and its triangulation are still very demanding tasks, which require sophisticated (commercial) tools. PATRAN by MSC.SOFTWARE [19] and GID [20] are suitable software packages, which have been used to create the models for this thesis, and for which import filters have been implemented.

The resolution of the finite element mesh – the maximum size of the finite elements – is determined by the smallest features which might occur in the solution of the PDE. These features have to be properly resolved and the approximation of the exact solution by the test functions has to be sufficiently accurate to give meaningful results.

In micromagnetics these limits are defined by three typical lengths:

1.

$$l_{\text{bex}} = \sqrt{A/K_1} \quad , \quad \delta_{\text{BW}} = \pi l_{\text{bex}}$$

δ_{BW} is the width of Bloch type magnetic domain walls (typically found

in bulk hard magnets), A is the exchange constant and K_1 is the magnetocrystalline anisotropy constant. [21]

2.

$$l_{\text{nex}} = \sqrt{2\mu_0 A / J_{\text{s}}^2} \quad , \quad \delta_{\text{NW}} = \pi l_{\text{nex}}$$

δ_{NW} is the width of Néel walls (typically found in soft magnetic materials and thin films), J_{s} is the saturation polarization.

3.

$$l_{\text{thex}} = \sqrt{\frac{A}{J_{\text{s}} H_{\text{th}}}} \quad , \quad H_{\text{th}} = \sqrt{\frac{2\alpha k_{\text{B}} T}{\Delta t \gamma J_{\text{s}} l^3}}$$

l_{thex} is the thermal exchange length with the thermal field H_{th}, which depends on the Gilbert damping constant α, the temperature T, time step of the numerical time integration scheme Δt, the gyromagnetic ratio γ, and the spatial correlation length l (which equals the cell size) [22].

Material parameters of various ferromagnets can be found in App. C in Tab. C.1.

In the most general case, the maximum cell size of the finite element mesh has to be smaller than the minimum of the three lengths defined above [23]. In Sec. 7.3.4 the influence of the mesh size on the pinning field of SmCo permanent magnets is studied in more detail.

However, if the structure of the solution is roughly known, it is possible to use an "adapted" mesh for the simulations. It has a high resolution (small elements) in areas with very small features (domain walls) and a low resolution (large elements) in other areas where the solution (magnetization) is very uniform. As a result, the number of nodes (and therefore the number of unknowns) is reduced and the time required for the simulation can be greatly reduced. This technique has been used for the calculation of the equilibrium magnetization distribution in soft magnetic nanodots. The results are presented in Sec. 9.

For dynamic time dependent problems a rigid adapted mesh is often not suitable, because the solution changes over time and the smallest features of the solution move through the mesh. If they leave the high resolution mesh

and reach areas with larger finite elements, artificial pinning on the mesh will occur and give wrong results. Thus, an adaptive mesh refinement method is required, which changes the structure of the mesh during the simulation and adapts the resolution of the mesh to the solution. It can be shown, that these methods lead to (almost) optimal complexity and give most accurate results with the smallest numerical (computational) effort [24]. Adaptive mesh refinement methods are still a very active research area, and they have been successfully applied also in numerical micromagnetics [25, 26, 27, 28, 29].

2.5   Stiffness Matrix and Right Hand Side

When a regular triangulation $\mathcal{T}$ has been generated for the domain Ω, the space S of the numerical solution U has to be defined. A common choice of basis functions for the spline spaces S and S_D are "hat functions" (Fig. 2.2), which are defined for every node (x_j, y_j, z_j) of the finite element mesh as

$$\eta_j(x_k, y_k, z_k) = \delta_{jk} \quad (j, k = 1, \ldots, N) \quad . \tag{2.19}$$

We are using isoparametric elements, i.e. we use the same polynomials (linear basis functions) for the approximation of the geometry and the solution. If we define

$$S_D := \operatorname{span}\{\eta_j | (x_j, y_j, z_j) \notin \Gamma_D\} \tag{2.20}$$

then

$$U_D \in S_D$$

and we can calculate the stiffness matrix A_{jk} (Eq. (2.15)) and the right hand side b_j (Eq. (2.16)) as a sum over all elements T and surface triangles E on Γ_N

$$A_{jk} = \sum_{T \in \mathcal{T}} \int_T \nabla \eta_j \cdot \nabla \eta_k \, dv \tag{2.21}$$

and

$$b_j = \sum_{T \in \mathcal{T}} \int_T f \cdot \eta_j \, dv + \sum_{E \subset \Gamma_N} \int_E g \cdot \eta_j \, da - \sum_{k=1}^N U_k \int_\Omega \nabla \eta_j \cdot \nabla \eta_k \, dv \quad . \tag{2.22}$$
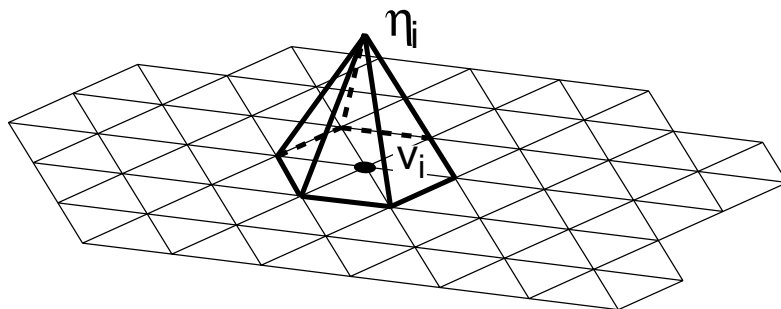
Figure 2.2: Hat function (linear basis function) for a triangulation in 2D.

It is most convenient to calculate the stiffness matrix on an element by element basis (local or element matrices) and finally assemble the contributions from the local matrices to the global stiffness matrix.

If we assume that the four vertices of a tetrahedral element T are given by (x_j, y_j, z_j) with $j = 1, \ldots, 4$, then the volume $|T|$ of the element is given by

$$|T| = \frac{1}{6} \det \begin{pmatrix} 1 & x_j & y_j & z_j \\ 1 & x_{j+1} & y_{j+1} & z_{j+1} \\ 1 & x_{j+2} & y_{j+2} & z_{j+2} \\ 1 & x_{j+3} & y_{j+3} & z_{j+3} \end{pmatrix} \tag{2.23}$$

where the local numbering $j = 1, \ldots, 4$ is chosen in such a way, that the right hand side of Eq. (2.23) is positive.

The corresponding basis functions are given by

$$\eta_j(x_k, y_k, z_k) = \delta_{jk} \quad , \quad j, k = 1, \ldots, 4 \quad .$$

Thus, η_j can also be written as

$$\eta_j(x, y, z) = \det \begin{pmatrix} 1 & x & y & z \\ 1 & x_{j+1} & y_{j+1} & z_{j+1} \\ 1 & x_{j+2} & y_{j+2} & z_{j+2} \\ 1 & x_{j+3} & y_{j+3} & z_{j+3} \end{pmatrix} / \det \begin{pmatrix} 1 & x_j & y_j & z_j \\ 1 & x_{j+1} & y_{j+1} & z_{j+1} \\ 1 & x_{j+2} & y_{j+2} & z_{j+2} \\ 1 & x_{j+3} & y_{j+3} & z_{j+3} \end{pmatrix}$$
$$\tag{2.24}$$

and

$$\nabla \eta_j(x, y, z) = \frac{1}{6|T|} \cdot$$

$$\begin{pmatrix} y_{j+2}z_{j+1} - y_{j+3}z_{j+1} - y_{j+1}z_{j+2} + y_{j+3}z_{j+2} + y_{j+1}z_{j+3} - y_{j+2}z_{j+3} \\ -x_{j+2}z_{j+1} + x_{j+3}z_{j+1} + x_{j+1}z_{j+2} - x_{j+3}z_{j+2} - x_{j+1}z_{j+3} + x_{j+2}z_{j+3} \\ x_{j+2}y_{j+1} - x_{j+3}y_{j+1} - x_{j+1}y_{j+2} + x_{j+3}y_{j+2} + x_{j+1}y_{j+3} - x_{j+2}y_{j+3} \end{pmatrix}$$

$$(2.25)$$

where all indices are understood modulo 4.

As a result we can easily calculate the stiffness matrix entries

$$A_{jk} = \sum_{T \in \mathcal{T}} \int_T \nabla \eta_j (\nabla \eta_k)^T \, dv \quad . \tag{2.26}$$

For the right hand side of Eq. (2.16) we need to evaluate $\int_T f \cdot \eta_j \, dv$. If we use the value of f in the center of gravity (x_S, y_S, z_S) of T, we can make the approximation

$$\int_T f \cdot \eta_j \, dv \approx \frac{|T|}{4} f(x_S, y_S, z_S) \quad . \tag{2.27}$$

The second term of the right hand side (Eq. (2.16)) can be evaluated in a similar way. However, Neumann boundary conditions will not be required in the following.

Finally, the Dirichlet boundary conditions have to be incorporated. One straight forward and easy to implement method is to replace all rows of the stiffness matrix A_{jk}, which correspond to Dirichlet boundary nodes, with zero and a single one in the main diagonal. On the right hand side, the entries of the Dirichlet nodes are replaced with their boundary values.

Chapter 3

Finite Element Micromagnetics

The total energy of a micromagnetic system is given by the Gibbs free energy E_{tot}, which depends on the magnetic polarization, the external field and some (temperature dependent) material parameters. It includes macroscopic contributions such as the Zeeman energy and the magnetostatic energy as well as microscopic contributions like the magnetocrystalline anisotropy energy and the exchange energy. This highlights the intermediate level of micromagnetics as a continuum theory again, which bridges the gap between the macroscopic world and microstructural and quantum mechanical effects.

The external field is independent of the magnetization distribution and the exchange and anisotropy energy are short range interactions, which depend only on the local magnetization distribution. Thus, they can be computed very efficiently. However, the magnetostatic field is a long-range interaction, which is the most expensive part in terms of memory requirements and computation time. Its calculation is usually based on a magnetic vector [30] or scalar potential (cf. Sec. 3.4). In addition, it is an open boundary problem, for which various methods have been developed [31, 32].

3.1 Gibbs Free Energy

The total Gibbs free energy is given by [33, 34]

$$E_{\text{tot}} \;\; = \;\; \int_{\Omega} \left(w_{\text{exch}} + w_{\text{ani}} + w_{\text{ext}} + w_{\text{demag}} \right) \, dv \;\; = \tag{3.1}$$

$$= \int_\Omega \Bigg(A\Big((\nabla \boldsymbol{u}_x)^2 + (\nabla \boldsymbol{u}_y)^2 + (\nabla \boldsymbol{u}_z)^2 \Big) +$$

$$K_1(1 - (\boldsymbol{a} \cdot \boldsymbol{u})^2) - \boldsymbol{J} \cdot \boldsymbol{H}_{\text{ext}} - \frac{1}{2}\boldsymbol{J} \cdot \boldsymbol{H}_{\text{demag}} \Bigg) dv \quad ,$$

where

$$\boldsymbol{J}(\boldsymbol{x}, t) = J_{\text{s}}(\boldsymbol{x}) \cdot \boldsymbol{u}(\boldsymbol{x}, t) \quad , \quad |\boldsymbol{u}| = 1 \tag{3.2}$$

describes the magnetic polarization as a function of space and time. A is the exchange constant, K_1 is the first magnetocrystalline anisotropy constant and $\boldsymbol{a}$ the unit vector parallel to the easy axis, $\boldsymbol{H}_{\text{ext}}$ the external field, and $\boldsymbol{H}_{\text{demag}}$ the demagnetizing field.

In thermodynamic equilibrium a micromagnetic system tries to reach a state with minimum total energy. The aim of micromagnetic theory is to find the magnetic polarization in equilibrium. Brown proposed a variational method [33], which is based on the calculation of the variational derivative of the total energy with respect to the magnetic polarization. In equilibrium (in an energy minimum) the coefficients of the linear term vanish for any variation $\delta \boldsymbol{u}$

$$\frac{\delta E_{\text{tot}}}{\delta \boldsymbol{u}} = 0 \quad . \tag{3.3}$$

This leads to Brown's equations

$$\boldsymbol{u} \times \Big(2A\Delta\boldsymbol{u} + 2K_1\boldsymbol{a}(\boldsymbol{u} \cdot \boldsymbol{a}) + J_{\text{s}}\boldsymbol{H}_{\text{ext}} + J_{\text{s}}\boldsymbol{H}_{\text{demag}} \Big) = 0 \tag{3.4}$$

Thus, in equilibrium the magnetic polarization $\boldsymbol{J}$ is parallel to an "effective field"

$$\boldsymbol{H}_{\text{eff}} = \frac{2A}{J_{\text{s}}}\Delta\boldsymbol{u} + \frac{2K_1}{J_{\text{s}}}\boldsymbol{a}(\boldsymbol{u} \cdot \boldsymbol{a}) + \boldsymbol{H}_{\text{ext}} + \boldsymbol{H}_{\text{demag}} \tag{3.5}$$

and the torque which acts on the polarization vanishes

$$\boldsymbol{J} \times \boldsymbol{H}_{\text{eff}} = 0 \quad . \tag{3.6}$$

Since any contribution parallel to the polarization $\boldsymbol{J}$ does not add to the torque, it does not make any difference if the magnetic field $\boldsymbol{H}$ or the magnetic induction $\boldsymbol{B} = \mu_0\boldsymbol{H} + \boldsymbol{J}$ is used for the effective field.

3.2 Gilbert Equation of Motion

The minimization of Eq. (3.1) can find an equilibrium magnetization distribution. However, the energy landscape of micromagnetic systems is usually very complicated and contains many local maxima, minima, and saddle points. Therefore, the choice of the initial magnetization distribution has a strong influence on the result. A more physical approach to the problem and a more realistic approach of the system to its equilibrium in a local minimum is provided by a dynamic description of the path through the energy landscape.

The motion of a magnetic moment in a magnetic field is mainly governed by its Larmor precession around the local magnetic field. The damping of the precession causes the relaxation to equilibrium. There are many processes which contribute to the damping in a magnetic solid like magnon-magnon and magnon-phonon interactions, interactions between localized and itinerant electrons and eddy currents, for example [35, 36, 37].

The *Gilbert equation* [38, 39] describes the precession and combines all damping effects in a phenomenological damping term with a single damping constant α

$$\frac{d\boldsymbol{J}}{dt} = -\gamma \boldsymbol{J} \times \boldsymbol{H} + \frac{\alpha}{J_\mathrm{s}} \boldsymbol{J} \times \frac{d\boldsymbol{J}}{dt} \quad , \tag{3.7}$$

where $\gamma = 2.210173 \times 10^5 \frac{\mathrm{m}}{\mathrm{As}}$ is the gyromagnetic ratio.

This formulation is equivalent to the *Landau-Lifshitz-Gilbert (LLG) equation*

$$\frac{d\boldsymbol{J}}{dt} = -\gamma' \boldsymbol{J} \times \boldsymbol{H} - \frac{\alpha\gamma'}{J_\mathrm{s}} \boldsymbol{J} \times (\boldsymbol{J} \times \boldsymbol{H}) \quad , \tag{3.8}$$

with

$$\gamma' = \frac{\gamma}{1 + \alpha^2} \quad . \tag{3.9}$$

The intrinsic timescale is determined by the Larmor frequency $\omega = \gamma \boldsymbol{H}_\mathrm{eff}$, which is usually in the order of GHz (cf. Sec. 9.4). Thus, the precession time is smaller than a nanosecond, which requires time steps in the order of picoseconds or even less. This limits the maximum simulated time to about 100 ns.

3.3 Discretization

In the following sections we will discretize the contributions to the total energy with the finite element method as shown in Sec. 2. For static energy minimization methods as well as for the calculation of the effective field Eq. (3.14) we have to calculate the derivative of the total energy with respect to the local magnetic polarization $\boldsymbol{J}$. In the following sections we will also derive these gradients.

First we have to define the discrete approximation of the magnetic polarization $\boldsymbol{J}(\boldsymbol{x})$ (Eq. (3.2)) by

$$\boldsymbol{J}(\boldsymbol{x}) \approx J_{\mathrm{s}}(\boldsymbol{x}) \sum_i \boldsymbol{u}_i \eta_i \approx \sum_i J_{\mathrm{s},i} \boldsymbol{u}_i \eta_i = \sum_i \boldsymbol{J}_i \quad , \tag{3.10}$$

where η_i denotes the basis function (hat function) at node i of the finite element mesh. The material parameters A, K, and J_{s} are defined element by element and they are assumed to be constant within each element. However, the magnetic polarization which depends on the saturation polarization J_{s} is defined on the nodes. Thus, we have to introduce the node based discrete approximation $J_{\mathrm{s},i}$ of the saturation polarization $J_{\mathrm{s}}(\boldsymbol{x})$ as

$$J_{\mathrm{s},i} = \frac{\int_\Omega J_{\mathrm{s}}(\boldsymbol{x}) \eta_i \, dv}{\int_\Omega \eta_i \, dv} = \frac{1}{4 V_i} \sum_{T \in \mathcal{T} \mid i \in T} J_{\mathrm{s},i} |T| \quad , \tag{3.11}$$

where V_i denotes the volume, which is assigned to node i of the mesh. It is given by

$$V_i = \int_\Omega \eta_i \, dv = \frac{1}{4} \sum_{T \in \mathcal{T} \mid i \in T} |T| \quad . \tag{3.12}$$

Since $\boldsymbol{J}$ is a vector with three Cartesian components we have three times the number of nodes unknowns to calculate.

For a given basis η_i the total energy can be expanded as

$$E_{\mathrm{tot}} = \int_\Omega w_{\mathrm{tot}}(\boldsymbol{J}) \, dv \tag{3.13}$$

and we get for the effective field using the box scheme [40]

$$\boldsymbol{H}_{i,\text{eff}} = - \left(\frac{\delta E_{\text{tot}}}{\delta \boldsymbol{J}} \right)_i \approx -\frac{1}{V_i} \frac{\partial E_{\text{tot}}}{\partial \boldsymbol{J}_i} = -\frac{1}{V_i J_{\text{s},i}} \frac{\partial E_{\text{tot}}}{\partial \boldsymbol{u}_i} \quad . \tag{3.14}$$

3.3.1   Exchange Energy

The exchange energy for one Cartesian component is given by

$$E_{\text{exch}} = \int_\Omega \sum_j A (\nabla u_j \eta_j)^2 \, dv \quad . \tag{3.15}$$

For the gradient we obtain

$$\frac{\partial E_{\text{exch}}}{\partial u_i} = \int_\Omega \sum_j A \frac{\partial}{\partial u_i} (\nabla u_j \eta_j)^2 \, dv \tag{3.16}$$

$$\frac{\partial}{\partial u_i} (\nabla u_j \eta_j)^2 = 2 u_j \nabla \eta_j \cdot \frac{\partial u_j \nabla \eta_j}{\partial u_i} = \tag{3.17}$$

$$= 2 u_j \nabla \eta_j \cdot \nabla \eta_j \delta_{ij} = \tag{3.18}$$

$$= 2 u_j \nabla \eta_j \cdot \nabla \eta_i \quad . \tag{3.19}$$

Finally, the gradient of the exchange energy is given by

$$\frac{\partial E_{\text{exch}}}{\partial u_i} = 2A \int_\Omega \sum_j u_j \nabla \eta_j \cdot \nabla \eta_i \, dv \quad , \tag{3.20}$$

which can be written as a linear system of equations with the coefficient matrix

$$G_{\text{exch},ij} = 2A \int_\Omega \nabla \eta_j \cdot \nabla \eta_i \, dv \quad . \tag{3.21}$$

The gradient can then be simply calculated as

$$\boldsymbol{g}_{\text{exch}} = G_{\text{exch}} \cdot \boldsymbol{u} \quad . \tag{3.22}$$

The expressions for the x, y, and z-component are identical and there are no mixed terms.

This exchange energy matrix is proportional to the stiffness matrix of the Laplacian operator Eq. (2.15), which is also obvious from Brown's equation Eq. (3.4) and the effective field Eq. (3.5).

3.3.2 Magnetocrystalline Anisotropy Energy

The magnetocrystalline anisotropy energy for uniaxial anisotropy is given by

$$E_{\text{ani}} = \int_{\Omega} \sum_{j} K_1 (1 - (\boldsymbol{a} \cdot \boldsymbol{u}_j \eta_j)^2) \, dv \quad . \tag{3.23}$$

The gradient is given by

$$\frac{\partial E_{\text{ani}}}{\partial u_{i,l}} = \int_{\Omega} \sum_{j} K_1 \frac{\partial}{\partial u_{i,l}} \left(1 - \left(\sum_{k}^{\{x,y,z\}} (a_k \cdot u_{j,k} \eta_j) \right)^2 \right) dv \tag{3.24}$$

$$\frac{\partial}{\partial u_{i,l}} \left(\sum_{k}^{\{x,y,z\}} (a_k \cdot u_{j,k} \eta_j) \right)^2 = 2 \sum_{k}^{\{x,y,z\}} (a_k \cdot u_{j,k} \eta_j) \cdot \sum_{m}^{\{x,y,z\}} (a_m \delta_{ij} \delta_{lm} \eta_j) =$$

$$= 2 \sum_{k}^{\{x,y,z\}} (a_k \cdot u_{j,k} \eta_j) \cdot a_l \eta_i \tag{3.25}$$

and we get the result

$$\frac{\partial E_{\text{ani}}}{\partial u_{i,l}} = -2K_1 a_l \int_{\Omega} \sum_{j} \sum_{k}^{\{x,y,z\}} a_k u_{j,k} \eta_j \cdot \eta_i \, dv \quad . \tag{3.26}$$

This can be rewritten in matrix notation as

$$\boldsymbol{g}_{\text{ani}} = G_{\text{ani}} \cdot \boldsymbol{u} \tag{3.27}$$

with

$$G_{\text{ani},i,l} = -2K_1 a_l \int_{\Omega} \sum_{k}^{\{x,y,z\}} a_k \eta_j \cdot \eta_i \, dv \quad . \tag{3.28}$$

3.3.3 Zeeman Energy

The Zeeman energy of a magnetic body $\boldsymbol{J}(\boldsymbol{x})$ in an external field $\boldsymbol{H}_{\text{ext}}(\boldsymbol{x})$ is simply given by

$$E_{\text{ext}} = \int_{\Omega} w_{\text{ext}}(\boldsymbol{J}) \, dv \quad = \quad \int_{\Omega} (-\boldsymbol{J} \cdot \boldsymbol{H}_{\text{ext}}) \, dv \; = \tag{3.29}$$

$$= \quad \int_{\Omega} \sum_{j} J_{\text{s},j} \sum_{k}^{\{x,y,z\}} u_{j,k} \eta_j H_{\text{ext},k} \, dv \quad . \tag{3.30}$$

For the gradient we find

$$\frac{\partial E_{\text{ext}}}{\partial u_{i,l}} \quad = \quad -\int_{\Omega} \sum_{j} J_{\text{s},j} \frac{\partial}{\partial u_{i,l}} \sum_{k}^{\{x,y,z\}} u_{j,k} \eta_j H_{\text{ext},k} \, dv \; = \tag{3.31}$$

$$= \quad \int_{\Omega} \sum_{j} -J_{\text{s},j} \sum_{k}^{\{x,y,z\}} \delta_{ij} \delta_{lk} \eta_j H_{\text{ext},k} \, dv \; = \tag{3.32}$$

$$= \quad -J_{\text{s},i} \int_{\Omega} \eta_i H_{\text{ext},l} \, dv \quad . \tag{3.33}$$

Since we know the external field explicitly, we can just simply add it to the other contributions to the effective field.

3.4 Demagnetizing Field and Magnetostatic Energy

The demagnetizing field is a little more complicated to handle, because it is an "open boundary problem" with one of its boundary conditions at infinity. In order to overcome this problem Fredkin and Koehler [41, 14, 42] proposed a hybrid finite element/boundary element method, which requires no finite elements outside the magnetic domain Ω.

Since we assume no free currents in our system, we can calculate the demagnetizing field using a magnetic scalar potential $\varphi(\boldsymbol{x})$. It has to satisfy

$$\Delta \varphi \quad = \quad \nabla \cdot \boldsymbol{J}(\boldsymbol{x}) \quad \text{for } \boldsymbol{x} \in \Omega \tag{3.34}$$

$$\Delta\varphi \;=\; 0 \quad \text{for } \boldsymbol{x} \notin \Omega \tag{3.35}$$

with the boundary conditions at the boundary Γ of Ω

$$\text{Div } \varphi = 0 \tag{3.36}$$

and

$$\text{Div } \frac{\partial\varphi}{\partial\boldsymbol{n}} = -\boldsymbol{n}\cdot\boldsymbol{J} \quad . \tag{3.37}$$

In addition it is required that $\varphi \to 0$ for $|\boldsymbol{x}| \to \infty$. The weak formulation of $\nabla\cdot\boldsymbol{J}$ is simply given by

$$\int_\Omega \nabla\cdot\boldsymbol{J}\,dv = \int_\Omega \sum_j \sum_k^{\{x,y,z\}} \nabla_k u_{j,k}\eta_j = \int_\Omega \sum_j \sum_k^{\{x,y,z\}} u_{j,k}\nabla_k\eta_j \quad , \tag{3.38}$$

which can again be written in matrix-vector format as

$$\boldsymbol{d} = D\cdot\boldsymbol{u} \tag{3.39}$$

with

$$D_{j,3j+k} = \int_\Omega u_{j,k}\nabla_k\eta_j \quad , \tag{3.40}$$

where k stands for the three Cartesian components $\{x,y,z\}$.

The main idea now is to split the magnetic scalar potential φ into φ_1 and φ_2. Then the problem can be reformulated for these potentials as

$$\Delta\varphi_1 = \nabla\cdot\boldsymbol{J} \tag{3.41}$$

with the boundary condition

$$\frac{\partial\varphi_1}{\partial\boldsymbol{n}} = \boldsymbol{n}\cdot\boldsymbol{J} \quad . \tag{3.42}$$

In addition $\varphi_1(\boldsymbol{x}) = 0$ for $\boldsymbol{x} \notin \Omega$.

As a result, we find for φ_2

$$\Delta\varphi_2 = 0 \tag{3.43}$$

with

$$\text{Div } \varphi_2 = \varphi_1 \tag{3.44}$$

and

$$\text{Div } \frac{\partial \varphi_2}{\partial \boldsymbol{n}} = 0 \quad . \tag{3.45}$$

It is required that $\varphi_2 \to 0$ for $|\boldsymbol{x}| \to \infty$.

Potential theory tells us that

$$\varphi_2(\boldsymbol{x}) = \frac{1}{4\pi} \int_\Gamma \varphi_1(\boldsymbol{y}) \frac{\partial G(\boldsymbol{x}, \boldsymbol{y})}{\partial \boldsymbol{n}(\boldsymbol{y})} \, da \quad , \tag{3.46}$$

where $G(\boldsymbol{x}, \boldsymbol{y}) = 1/|\boldsymbol{x} - \boldsymbol{y}|$ is the Green function.

φ_1 can be easily calculated using the standard finite element method as explained in Sec. 2.

The (numerically expensive) evaluation of Eq. (3.46) in all Ω can be avoided by just calculating the boundary values of φ_2 on Γ and then solving the Dirichlet problem Eq. (3.43) with the given boundary values. For $\boldsymbol{x} \to \Gamma$ Eq. (3.46) is given by

$$\varphi_2(\boldsymbol{x}) = \frac{1}{4\pi} \int_\Gamma \varphi_1(\boldsymbol{y}) \frac{\partial G(\boldsymbol{x}, \boldsymbol{y})}{\partial \boldsymbol{n}(\boldsymbol{y})} \, da + \left(\frac{S(\boldsymbol{x})}{4\pi} - 1 \right) \varphi_1(\boldsymbol{x}) \quad , \tag{3.47}$$

where $S(\boldsymbol{x})$ denotes the solid angle subtended by Γ at $\boldsymbol{x}$. Upon triangulation of the surface Γ of the domain Ω with triangular elements (which we naturally get from a triangulation of Ω with tetrahedral elements) and discretization of φ_1 and φ_2 we can rewrite Eq. (3.47) as

$$\boldsymbol{\varphi}_2 = B\boldsymbol{\varphi}_1 \tag{3.48}$$

with the boundary matrix B, which is a dense matrix with a size of $n_b \times n_b$ elements, where n_b is the number of nodes on the surface Γ.

The discretization of the scalar double layer operator in Eq. (3.47) has been derived by Lindholm [43]:

$$\int_\Gamma \varphi_1(\boldsymbol{y}) \frac{\partial G(\boldsymbol{x}, \boldsymbol{y})}{\partial \boldsymbol{n}(\boldsymbol{y})} \, da \approx \sum_{t \in \Gamma} \sum_{i=1}^{3} L_{t,i} \varphi_{1,t,i} \quad , \tag{3.49}$$

Figure 3.1: Local coordinate system and various vectors required for the discretization of the boundary integral Eq. (3.47) [43].

where t runs over all triangles on the surface Γ of the domain Ω and i runs over the three nodes of each triangle.

In order to calculate the matrix entries of B element by element (rather triangle by triangle) we use the local coordinates defined in Fig. 3.1.

$$L_{t,i} = \frac{s_{i+1}}{8\pi|t|} \left(\eta_{i+1} S_t - \zeta \sum_{j=1}^{3} \gamma_{ij} P_j \right) \tag{3.50}$$

$$
\begin{aligned}
\boldsymbol{\rho}_i &= \boldsymbol{r}_j - \boldsymbol{r} & \text{(3.51)} \\
s_i &= |\boldsymbol{\rho}_{j+1} - \boldsymbol{\rho}_j| & \text{(3.52)} \\
\eta_i &= \hat{\boldsymbol{\eta}}_j \cdot \boldsymbol{\rho}_j & \text{(3.53)} \\
\zeta &= \hat{\boldsymbol{\zeta}} \cdot \boldsymbol{\rho}_j & \text{(3.54)} \\
\gamma_{ij} &= \hat{\boldsymbol{\xi}}_{i+1} \cdot \hat{\boldsymbol{\xi}}_j & \text{(3.55)} \\
P_j &= \ln \frac{\rho_j + \rho_{j+1} + s_j}{\rho_j + \rho_{j+1} - s_j} & \text{(3.56)}
\end{aligned}
$$

$|t|$ denotes the area of triangle t and S_t the solid angle subtended by triangle

t at the "observation point" $\boldsymbol{r}$, which is given by

$$S_t = 2 \cdot \mathrm{sgn}(\zeta) \cdot \arccos\left(\frac{\rho_1\rho_2\rho_3 + \rho_1\boldsymbol{\rho}_2 \cdot \boldsymbol{\rho}_3 + \rho_2\boldsymbol{\rho}_3 \cdot \boldsymbol{\rho}_1 + \rho_3\boldsymbol{\rho}_1 \cdot \boldsymbol{\rho}_2}{\sqrt{2(\rho_2\rho_3 + \boldsymbol{\rho}_2 \cdot \boldsymbol{\rho}_3)(\rho_3\rho_1 + \boldsymbol{\rho}_3 \cdot \boldsymbol{\rho}_1)(\rho_1\rho_2 + \boldsymbol{\rho}_1 \cdot \boldsymbol{\rho}_2)}}\right).$$
(3.57)

In order to calculate the demagnetizing field, we have to perform the following steps:

Initialization

1. Discretize Eq. (3.41).

2. Calculate the boundary matrix in Eq. (3.48).

Solution

1. Solve Eq. (3.41) for a given magnetization distribution $\boldsymbol{J}$ using the standard FE method.

2. Calculate φ_2 on the boundary Γ using Eq. (3.48) to get the values for the Dirichlet boundary conditions.

3. Calculate φ_2 in the whole domain Ω using Eq. (3.43) with Dirichlet boundary values.

4. Calculate $\boldsymbol{H}_{\mathrm{demag}} = -\nabla(\varphi_1 + \varphi_2)$.

3.5 Effective Field

Finally we can collect all contributions to the effective field and calculate it by simple matrix-vector multiplications.

$$\boldsymbol{H}_{i,\mathrm{eff}} \approx -\frac{1}{V_i J_{\mathrm{s},i}}\frac{\partial E_{\mathrm{tot}}}{\partial \boldsymbol{u}_i} = (\boldsymbol{H}_{\mathrm{ext}} + \boldsymbol{H}_{\mathrm{demag}})_i - \frac{1}{V_i J_{\mathrm{s},i}}\left((G_{\mathrm{exch}} + G_{\mathrm{ani}}) \cdot \boldsymbol{u}\right)_i$$
(3.58)

Since the matrices for the exchange and anisotropy energies depend only on the (time independent) material parameters and the geometry, they need to be calculated only once at the beginning. In order to save time and memory, they can also be assembled into a single combined matrix, if the energies and fields are not required separately.

Chapter 4

Solution of the Micromagnetic Equations

4.1   Energy Minimization

In Sec. 3 we have introduced the Gibbs free energy of a micromagnetic system, discretized various contributions to the total energy, and derived the matrix-vector formulation. Some complication was introduced by the demagnetizing field, but the hybrid finite-element/boundary element method provides an elegant way to solve the problem accurately with a finite element mesh, which is restricted to the magnetic bodies.

This enables us to implement a simple energy minimization scheme to find the equilibrium magnetization distribution. If the magnetic polarization $\boldsymbol{J}$ is defined in Cartesian coordinates,

$$\boldsymbol{J}(\boldsymbol{x}) \approx \sum_i J_{\mathrm{s},i} \boldsymbol{u}_i \eta_i = \sum_i J_{\mathrm{s},i} \begin{pmatrix} u_{i,x} \\ u_{i,y} \\ u_{i,z} \end{pmatrix} \eta_i \qquad (4.1)$$

one has to use a constrained solver, which ensures, that the norm of $\boldsymbol{J}$ is preserved: $|\boldsymbol{J}| = J_{\mathrm{s}}$. However, it has been shown [44, 45] that the use of spherical coordinates has several advantages:

- The number of unknowns is reduced by 1/3, which speeds up the solver.

- The norm is automatically preserved, which allows the use of an unconstrained solver.

- Convergence problems with a Lagrange multiplier approach for the constraint $|\boldsymbol{J}| = J_\mathrm{s}$ are avoided.

However, the direct calculation of the energy gradient in spherical coordinates causes various problems due to the periodicity of the polar and azimuth angles. Therefore, the magnetic polarization for the minimizer is given in spherical coordinates ($\theta \in [0; \pi[$, $\varphi \in [0; 2\pi[$).

$$
\begin{pmatrix} u_{i,x} \\ u_{i,y} \\ u_{i,z} \end{pmatrix} = \begin{pmatrix} \sin\theta_i \cos\varphi_i \\ \sin\theta_i \sin\varphi_i \\ \cos\theta_i \end{pmatrix} \quad , \quad \begin{pmatrix} \theta_i \\ \varphi_i \end{pmatrix} = \begin{pmatrix} \arccos(u_{i,z}) \\ \arctan(u_{i,y}/u_{i,x}) \end{pmatrix} \quad (4.2)
$$

Then it is converted to Cartesian coordinates. The energy gradient is calculated in Cartesian coordinates, converted back to spherical coordinates

$$
\frac{\partial E}{\partial \theta_i} = \frac{\partial E}{\partial u_{i,x}} \frac{\partial u_{i,x}}{\partial \theta_i} + \frac{\partial E}{\partial u_{i,y}} \frac{\partial u_{i,y}}{\partial \theta_i} + \frac{\partial E}{\partial u_{i,z}} \frac{\partial u_{i,z}}{\partial \theta_i} = \tag{4.3}
$$

$$
= \frac{\partial E}{\partial u_{i,x}} \cos\theta_i \cos\varphi_i + \frac{\partial E}{\partial u_{i,y}} \cos\theta_i \sin\varphi_i - \frac{\partial E}{\partial u_{i,z}} \sin\theta_i \tag{4.4}
$$

$$
\frac{\partial E}{\partial \varphi_i} = \frac{\partial E}{\partial u_{i,x}} \frac{\partial u_{i,x}}{\partial \varphi_i} + \frac{\partial E}{\partial u_{i,y}} \frac{\partial u_{i,y}}{\partial \varphi_i} + \frac{\partial E}{\partial u_{i,z}} \frac{\partial u_{i,z}}{\partial \varphi_i} = \tag{4.5}
$$

$$
= \frac{\partial E}{\partial u_{i,x}} (-\sin\theta_i \sin\varphi_i) + \frac{\partial E}{\partial u_{i,y}} \sin\theta_i \cos\varphi_i \tag{4.6}
$$

and returned to the minimizer.

For the minimizer itself the limited memory variable metric (LMVM) algorithm – a quasi-Newton-method – of the TAO package [46, 47] has been selected, because it requires only the function values and the gradient of the total energy. In replacement for the Hessian (which is not available due to the demagnetizing field) the second-order information is approximated by a limited history of previous points and gradients. A similar method has been used in [44] and showed better convergence rates than Newton- or Gauß-Seidel methods.

4.2 The Dynamic Equation

The Landau-Lifshitz-Gilbert equation (Eq. (3.8)) is a system of ordinary differential equations (ODEs), which can be written in a general form as

$$\frac{d\boldsymbol{y}}{dt} = \boldsymbol{f}(t, \boldsymbol{y}) \quad , \quad \boldsymbol{y} \in \mathbb{R}^N \tag{4.7}$$

with the initial condition

$$\boldsymbol{y}(t_0) = \boldsymbol{y}_0 \quad . \tag{4.8}$$

The PVODE package [48, 49] is a general purpose solver for initial-value problems for stiff and non-stiff ODEs of the form of Eq. (4.7). It is based on CVODE [50, 51] and uses MPI for parallelization and portability.

Two methods are available for the numerical solution of Eq. (4.7): The backward differentiation formula (BDF), which is recommended for stiff problems, and the Adams-Moulton formula for non-stiff problems, both of which feature a variable stepsize and variable order. Both formulas can be written as the linear multistep formula

$$\sum_{i=0}^{K_1} \alpha_{n,i} y_{n-i} + h_n \sum_{i=0}^{K_2} \beta_{n,i} \frac{dy_{n-i}}{dt} = 0 \quad , \tag{4.9}$$

where $h_n = t_n - t_{n-1}$ is the stepsize and q the order. The Adams-Moulton formula is obtained with $K_1 = 1$ and $K_2 = q - 1$ with $1 \leq q \leq 12$. The BDF formula is represented by Eq. (4.9) with $K_1 = q$ and $K_2 = 0$ with $1 \leq q \leq 5$. The numerical integration is started with $q = 1$ and then varied automatically and dynamically.

If we insert Eq. (4.7) in Eq. (4.9) we get an implicit nonlinear system of equations for $\boldsymbol{y}$

$$\boldsymbol{G}(\boldsymbol{y}_n) := \boldsymbol{y}_n - h_n \beta_{n,0} \boldsymbol{f}(t_n, \boldsymbol{y}_n) - \boldsymbol{a}_n = 0 \quad , \tag{4.10}$$

which has to be solved at each time step. $\beta_{n,0}$ and $\boldsymbol{a}_n$ depend on the method, the integration order, and the previous time steps. An efficient method for nonstiff problems is functional iteration, because it does not require the solution of a linear system of equations. However, for stiff problems it is better

solved by Newton iteration, which does involve the solution of a linear system of equations. PVODE uses a Krylov subspace method – the iterative scaled preconditioned generalized minimal residual method (SPGMR) [52], whose performance can be considerably improved with suitable preconditioners.

4.2.1 Preconditioning

Preconditioning of the system of linear equations involved in the Newton iteration of the Krylov subspace method can considerably speed up its solution [53]. In addition, this method leads to fewer function evaluations of the Landau-Lifshitz-Gilbert equation and allows larger time steps, which gives an excellent performance of the numerical time integration.

In order to find the root of Eq. (4.10), the Newton method requires the calculation of the intermediate corrections $\Delta \boldsymbol{y} = \boldsymbol{y}_m - \boldsymbol{y}_{m-1}$, which follow from

$$\frac{\partial \boldsymbol{G}}{\partial \boldsymbol{y}} \Delta \boldsymbol{y} = -\boldsymbol{G}(\boldsymbol{y}_{m-1}) \quad . \tag{4.11}$$

The matrix $\partial \boldsymbol{G}/\partial \boldsymbol{y}$ in this linear system of equations is approximated by

$$\partial \boldsymbol{G}/\partial \boldsymbol{y} \approx I - h_n \beta_{n,0} \frac{\partial \boldsymbol{f}}{\partial \boldsymbol{y}} \quad . \tag{4.12}$$

The calculation of the Jacobian of $\boldsymbol{f}$

$$\frac{\partial \boldsymbol{f}}{\partial \boldsymbol{y}} = \frac{\partial}{\partial \boldsymbol{J}} \left(-\gamma' \boldsymbol{J} \times \boldsymbol{H} - \frac{\alpha \gamma'}{J_{\mathrm{s}}} \boldsymbol{J} \times (\boldsymbol{J} \times \boldsymbol{H}) \right) \tag{4.13}$$

requires the calculation of the Jacobian of the total energy with respect to the magnetization.

We have derived the expressions for the gradient of the total energy in Sec. 3.3. Since the total energy is a simple sum of exchange, magnetocrystalline anisotropy, Zeeman, and magnetostatic energy, we have calculated their gradients individually. For the first two contributions we found, that the gradient of the energy is a linear function of magnetization and ended up with a matrix-vector formulation. The external field is explicitly given anyway, but the magnetostatic field had to be calculated with a hybrid finite element/boundary element method.

Now we can analyze their contributions to the Jacobian of the total energy. The external field does not contribute at all, since it is independent of the magnetization and its first derivative with respect to the magnetization is zero. The first derivative of the demagnetizing field would contribute. However, it is not considered for the calculation of the Jacobian for two reasons. First, its calculation would be very expensive in terms of computational effort, and, due to its long-range nature, it would lead to a full matrix for the Jacobian. This results in huge memory requirements and a lot of communication between the processors in a parallel program. Moreover, we do not need the exact Jacobian, but a sensible approximation, which still speeds up the Newton iterations. Thus, it is sensible to consider only the contributions from the exchange and magnetocrystalline anisotropy energy.

The calculation of the Jacobian of these two energy terms is finally very easy. We have already calculated their gradient with respect to the magnetization in order to calculate their contributions to the local field. As mentioned before, we found the energy gradients to be linear with respect to the magnetization and came up with a matrix-vector formulation. Due to this linearity, their Jacobians are just simply given by these matrices Eq. (3.21) and Eq. (3.28) and we just have to add them up to get the approximate Jacobian for the total energy.

Finally, instead of calculating Eq. (4.11) with Eq. (4.12) directly, the preconditioning technique is applied [54]: The linear system

$$A\boldsymbol{x} = \boldsymbol{b} \tag{4.14}$$

is rewritten as

$$(AP^{-1})(P\boldsymbol{x}) = \boldsymbol{b} \tag{4.15}$$

and

$$A'\boldsymbol{x}' = \boldsymbol{b} \tag{4.16}$$

with $A' = AP^{-1}$ and $\boldsymbol{x}' = P\boldsymbol{x}$. If P is a good approximation to A, then A' is close to the identity matrix and Eq. (4.16) can be solved very efficiently.

4.3   The Nudged Elastic Band Method

In order to find possible paths of a micromagnetic system through its energy landscape to a local minimum of the total energy, we have implemented the static energy minimization method (cf. Sec. 4.1) and the time integration of the Landau-Lifshitz-Gilbert equation (cf. Sec. 4.2). We applied it to nucleation (cf. Sec. 8) and domain wall pinning problems (cf. Sec. 7) as well as investigations of dynamic magnetization reversal processes (cf. Sec. 9, Sec. 10). However, the investigation of thermal stability, which is an important topic especially in the area of magnetic storage devices, requires the calculation of transition rates between stable equilibrium states of the system. The transition rate between two stable equilibria is determined by the lowest energy barrier (saddle point), which separates them. Henkelman and Jónsson proposed the nudged elastic band method to calculate these minimum energy paths [55]. This method has been successfully applied to complex micromagnetic systems [56, 57] and it is especially suitable for parallelization.

The path is represented by a sequence of "images" (magnetization distributions), which connects the two given stable equilibrium states $\boldsymbol{M}_i$ and $\boldsymbol{M}_f$. These equilibria may be obtained using the static energy minimization method, for example. The initial path is given by the initial magnetization distribution $\boldsymbol{M}_i$ and the final magnetization distribution $\boldsymbol{M}_f$ and a number of images $\boldsymbol{M}_k$ in between, which can be obtained by simple linear interpolation. Then, an optimization algorithm is applied, which moves the "elastic band of images" through the energy landscape towards the optimal path, which is defined by

$$(\nabla E(\boldsymbol{M}_k) \cdot \boldsymbol{t})\boldsymbol{t} = \nabla E(\boldsymbol{M}_k) \quad , \tag{4.17}$$

where $\nabla E(\boldsymbol{M}_k)$ denotes the gradient of the total energy at image $\boldsymbol{M}_k$ and t is the unit tangent vector along the path. In order to avoid kinks in the path the tangent is calculated using forward, backward, or second order central differences. Eq. (4.17) requires the component of the gradient parallel to the tangent to be equal to the gradient. In other words, the optimal path is characterized by fact that the gradient of the total energy is parallel to the

tangent for any image $\boldsymbol{M}_k$.

Starting from the initial path an iterative optimization scheme is applied, which moves the images $\boldsymbol{M}_k$ in a direction $\boldsymbol{D}(\boldsymbol{M}_k)$, which is given by

$$\boldsymbol{D}(\boldsymbol{M}_k) = -\Big(\nabla E(\boldsymbol{M}_k) - (\nabla E(\boldsymbol{M}_k) \cdot \boldsymbol{t})\boldsymbol{t}\Big) \quad . \tag{4.18}$$

The interpretation of this expression is obvious: The images are moved along the negative gradient of the total energy perpendicular to the tangent. The negative gradient determines the direction towards lower energy while the distance between the images is preserved by taking only the component perpendicular to the tangent. Thus, an ordinary differential equation can be formulated

$$\frac{\partial \boldsymbol{M}_k}{\partial t} = \boldsymbol{D}(\boldsymbol{M}_k) \quad , \tag{4.19}$$

where t denotes some artificial time parameter, which is integrated using any ODE solver.

After the discussion of the static energy minimization method and the time integration the Landau-Lifshitz-Gilbert equation, the implementation of the nudged elastic band method has become very simple, because we can reuse parts of both of them. The static energy minimization provides us with the gradient of the total energy and for the integration of Eq. (4.19), we can use the same methods explained in Sec. 4.2 by just replacing the right hand side of Eq. (4.7) with Eq. (4.18).

The parallelization of this method can be done by distributing the images across the processors. Thus, every processors needs the full set of matrices (but only one copy independent of the number of images), which are required for the calculation of the local fields (and gradients). However, there is no need to partition the finite element mesh any more, because every processor has to do the full calculation for the images. This has the advantage, that no communication is required during the calculation of the gradient of the total energy. Only for the calculation of the tangents the magnetization of some images has to be copied to "neighboring" processors.

Chapter 5

Implementation

The implementation of the micromagnetics package is based on the freely available open source toolbox "PETSc" – the Portable, Extensible Toolkit for Scientific Computation [58]. It provides the data structures and low level linear algebra and many utility routines for small serial programs as well as large-scale applications for massively parallel supercomputers. Most important, it has a very clear design and simple interfaces for a steep learning curve and many additional features, which speed up the development process and help identifying and avoiding the pitfalls of parallel programs.

5.1   Required Libraries

The basic structure of the PETSc package is outlined in Fig. 5.1. It is built on well established standards for scientific computation: The BLAS libraries for basic linear algebra operations [59], LAPACK for higher level linear algebra functions [60], LINPACK for dense matrix factorization [61], and MPI for interprocess communication [62, 63], to name the most important ones. For all these libraries there are highly optimized implementations for all major hardware platforms available, which ensures easy portability and maximum performance.

On top of these "building blocks" PETSc implements commonly used data structures like vectors and matrices, the latter in various formats for dense, sparse, and block diagonal types for serial or parallel programs. These
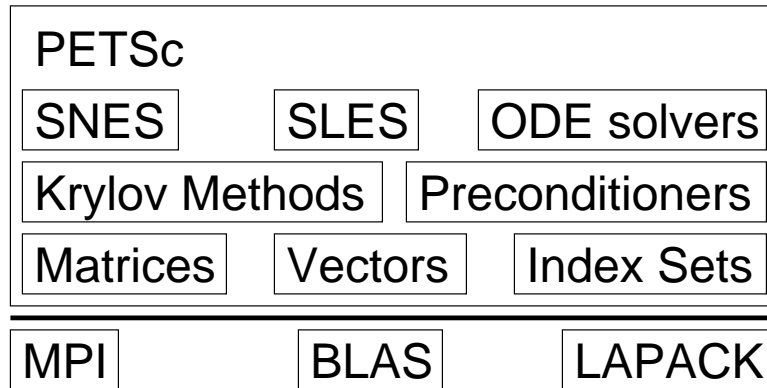
Figure 5.1: Structure of the PETSc library.

data structures are then used by the different numerical solvers for linear and nonlinear systems and ODEs to carry out the calculations with the underlying libraries. Even though PETSc is implemented in plain ANSI C it uses many object oriented techniques like data encapsulation and polymorphism, which makes it very flexible and efficient. Moreover, it provides a number of utility functions, which simplify the implementation of the application around the numerical problem: There are routines for the handling of program parameters and configuration files, data i/o and graphics output, profiling and logging, debugging and memory allocation tracking.

In addition, PETSc has interfaces to several other software packages. The 'Toolkit for Advanced Optimization" (TAO) [46] is one of them, and it is used for the static energy minimization in the micromagnetics application (in fact TAO itself is built on PETSc). There are also interfaces to ParMetis for parallel graph partitioning and PVODE [48] the parallel ODE integrator. For reasons to be explained later these built-in interfaces have not been used, but still the integration into PETSc is straight forward.

TAO is among a number of other libraries, which are used by the micromagnetics application (Fig. 5.2). The Metis library is used for mesh partitioning [64], PVODE for the time integration of the LLG equation [48], zlib for compressed data output [65], and libpng for the direct output of graphics files in PNG format [66].

A complete list of all required packages, short descriptions, references, and URLs can be found in App. B.

TAO	PVODE
Mesh handling	data/graphics
Metis	MPI	BLAS	LAPACK	zlib	libpng
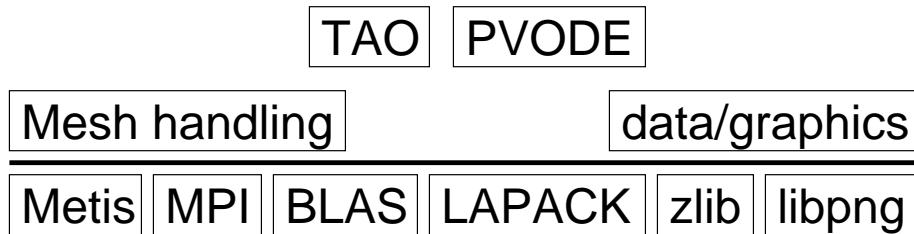
Figure 5.2: Structure of additional libraries.

5.2 Program Structure

The micromagnetics application can be divided into four sections (Fig. 5.3). First there is a short serial initialization part, which is executed on just one single processor. It reads the configuration files, various input files for the finite element mesh, the initial magnetization, material parameters, etc. Then the data are distributed to the different processors and all required initialization steps for parallel processing are initiated. Next the micromagnetic solvers are initialized, any remaining data structures are created, and stiffness and boundary matrices are calculated. Then the solver is called, which calculates energies and energy gradients, local fields and magnetization distributions. It continues calculating iteratively all desired quantities until some exit condition is met. Finally, the last state of the simulation is stored, all data structures are destroyed and the parallel processing environment is cleaned up.

To achieve optimal performance, it is sensible to make the initial serial initialization part as short as possible. However, this may require some additional data exchange between different processors at a later stage of the initialization phase. Even worse, it increases the amount of "bookkeeping" which is necessary to keep track of the distributed data. This trade off has shown up in the mesh partitioning phase, which can be done in parallel using ParMetis via the built-in interface of PETSc. Yet, it proved to be easier to handle, if it is done during the serial initialization phase on just a single processor. Since the whole initialization process itself usually takes only a fraction of the time of the rest of the simulation, it is not as important anyway.
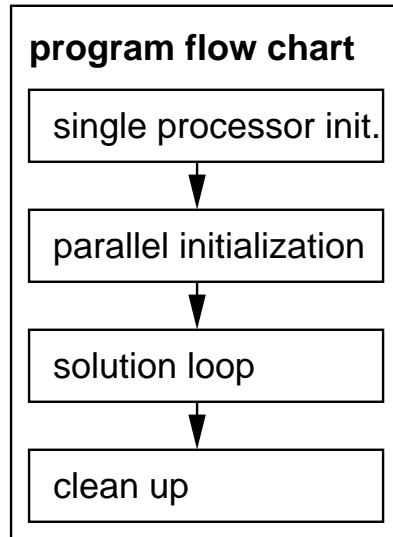
Figure 5.3: Coarse flow chart of the program.

5.2.1   Serial Initialization

The main tasks during the serial initialization phase are summarized in Fig. 5.4. When the application is started, the different instances of the application on various processors are initialized and synchronized. Then the first processor reads the configuration file for the simulation and evaluates the parameters and command line arguments. This is followed by reading the finite element mesh, reading the material parameters file and initializing the magnetization distribution. If requested, the finite element mesh is refined globally before it is partitioned using the Metis library.

Metis uses a very efficient serial multilevel k-way partitioning algorithm [67, 68], which gives high quality partitionings. First, the structure of the finite element mesh has to be mapped to a graph suitable for processing by Metis. The structure of the mesh is in its simplest form defined by a list of elements, for each of which the ids of its four vertices are given. The utility function `METIS_MeshToDual` generates from this information the dual graph in which each vertex corresponds to an element in the mesh and each edge connecting two vertices indicates, that the corresponding elements share a face. (This information is later also used to detect the boundary triangles of the finite element mesh and to calculate the boundary matrix as described

```
┌─────────────────────────────┐
│ single processor            │
│ initialization              │
│   ┌───────────────────────┐ │
│   │ PETSc/MPI init.       │ │
│   └───────────────────────┘ │
│              ↓              │
│   ┌───────────────────────┐ │
│   │ read FE mesh          │ │
│   └───────────────────────┘ │
│              ↓              │
│   ┌───────────────────────┐ │
│   │ read parameters       │ │
│   └───────────────────────┘ │
│              ↓              │
│   ┌───────────────────────┐ │
│   │ mesh partitioning     │ │
│   └───────────────────────┘ │
│              ↓              │
│   ┌───────────────────────┐ │
│   │ distribute data       │ │
│   └───────────────────────┘ │
└─────────────────────────────┘
```
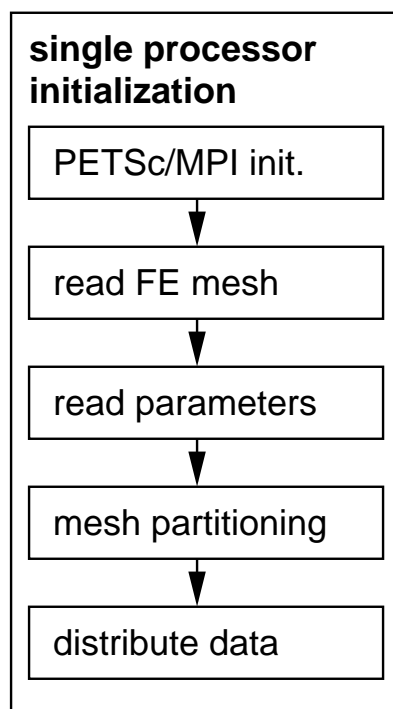
Figure 5.4: Flow chart of the single processor initialization section.

in Sec. 3.4.) Then the graph is partitioned in such a way, that the mesh is split into equal-size parts and the number of adjacent elements assigned to different processors is minimized. The first condition leads to a load balancing among the processors (assuming a set of equal processors), whereas the second should minimize the communication between different processors resulting from the assignment of adjacent elements to different processors. Based on the partitioning of the elements the nodes of the mesh are assigned to those processors, to which the majority of elements, which shares a given node, belongs (subject to balance constraints). Each processor then has (approximately) the same number of elements and nodes and a minimum of faces and nodes, which are shared with other processors. Fig. 5.5 shows the partitioning of the finite element mesh of a flat cylinder. The model is cut parallel to the axis of the cylinder, which results in the smallest areas of the cut planes and the smallest number of faces and nodes, which are shared by different partitions.

The dual graph of the finite element mesh is also used to prepare the

(a)

(b)

(c)

(d)
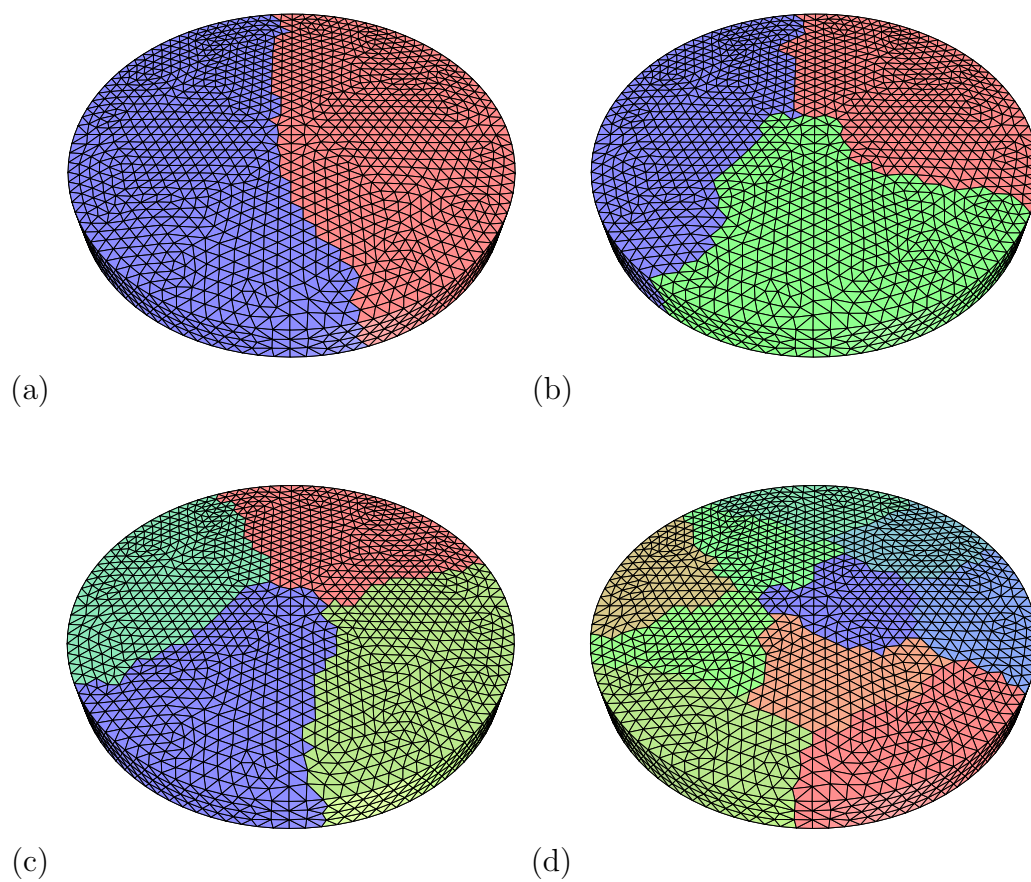
Figure 5.5: Mesh partitioning of a soft magnetic nanodot for two, three, four, and ten processors, respectively. Different colors correspond to parts which are assigned to different processors.

calculation of the boundary element matrix involved in the calculation of the demagnetizing field (cf. Sec. 3.4). There we need the boundary faces of the finite element mesh. Since we know the element connectivities from the dual graph, we immediately know all boundary elements, since they have at most three neighbors with which they share a common face. As we loop over all these elements, we just have to compare the faces with those of the neighbors to find out, which face lies on the surface of the finite element mesh. Especially this step would be quite troublesome, if the mesh was already distributed, because it would require a lot of communication and bookkeeping. Then, the boundary nodes are easily identified by the boundary faces.

According to the partitioning scheme suggested by Metis all data are then distributed to their destination processors. Many parameters like the initial time, number of nodes, elements, and faces, material parameters and vertex coordinates are broadcast to all processors. Other data arrays like the vertex to element assignment, element properties, and other element data are delivered just to the processors, which "own" the element. However, these data structures make only a minor part of the total required storage space.

All these steps are done only by the first processor, but the serial initialization part is very short and not computation intensive, which is the reason for the excellent scaling of the program initialization, which will be shown in Sec. 6.3.

5.2.2 Parallel Initialization

When all data have been delivered to their proper processors, the parallel data structures can be created and initialized (cf. Fig. 5.6). The parallel PETSc vectors for local magnetic fields, magnetic scalar potentials, etc. are created and the parallel solver for the Poisson problem is initialized.

Then the computation intensive part starts: First, the finite element mesh is analyzed thoroughly. The volumes of all elements and vertices (using the box scheme [40]), element quality factors, and the corresponding extrema and averages are calculated. Next, the stiffness matrix of the Poisson problem (Eq. (2.15)) and the matrices for the contributions to the local field
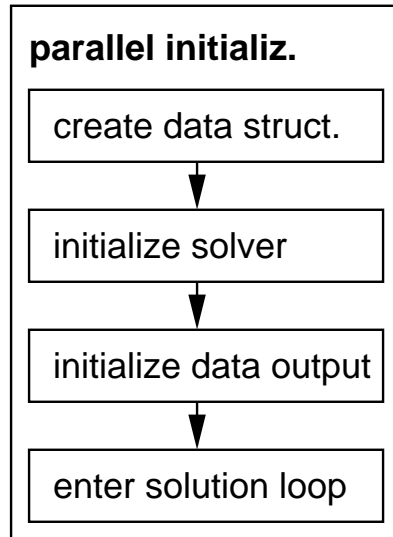
Figure 5.6: Flow chart of the parallel initialization section.

(Eqs. (3.21), (3.28)) are calculated on an element by element basis. However, the results are directly inserted in the global matrices, where the contributions from different elements (even from different processors) are added up by PETSc automatically. This behavior makes the handling of the nodes of the finite element mesh very convenient, because we do not have to manage any duplicate nodes ("ghost points").

Fig. 5.7 shows how PETSc distributes the data of matrices and vectors over the processors. For example, a simple 8×8 matrix is split into four partitions for four processors. The first two rows are stored on the first processor, the next two rows on the second processor, another two rows on the third, and the last two rows on the fourth processor. Vectors are distributed in a similar way: Each processors holds those elements which correspond to nodes of the finite element mesh that have been assigned to that processor.

The sparsity pattern of the stiffness matrix of the nanodot model on a single processor is shown on the left in Fig. 5.8. The band structure is achieved by a suitable numbering of the nodes, which has in this case been optimized by the mesh generator Patran using the Gibbs-Poole-Stockmeyer algorithm [69]. This can already be considered a type of "mesh partitioning"
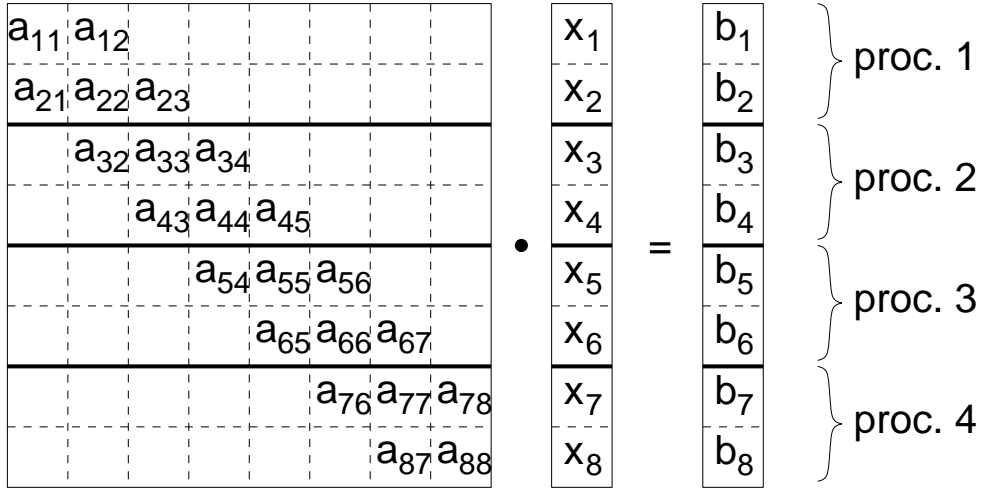
Figure 5.7: Matrix-vector multiplication with matrix and vector elements distributed over four processors.

since it renumbers the nodes in such a way, that nodes with common edges are close to each other in the numbering scheme. Thus, after partitioning the band structure is only slightly disturbed as shown on the right in Fig. 5.8, where the sparsity pattern of the whole stiffness matrix on two processors is shown. The dashed line separates the parts of the first and second processor.

Then, the boundary solid angles $S(\boldsymbol{x})$ are calculated which are subsequently used during the calculation of the boundary matrix (cf. Eq. (3.47)). In each element the solid angles subtended by the face opposite each node v_i (Fig. 5.9) are calculated as

$$\omega(v_i) = \alpha + \beta + \gamma - \pi \quad , \tag{5.1}$$

where α, β, and γ denote the dihedral angles between each pair of faces, which share the node v_i. These dihedral angles are calculated using the face normals (e.g. $\boldsymbol{n}_a$ and $\boldsymbol{n}_b$) as

$$\alpha = \pi - \arccos(\boldsymbol{n}_a \cdot \boldsymbol{n}_b) \tag{5.2}$$

The contributions from all elements sharing a common node are summed up and finally give the required boundary solid angle $S(\boldsymbol{x})$. If this calculation is
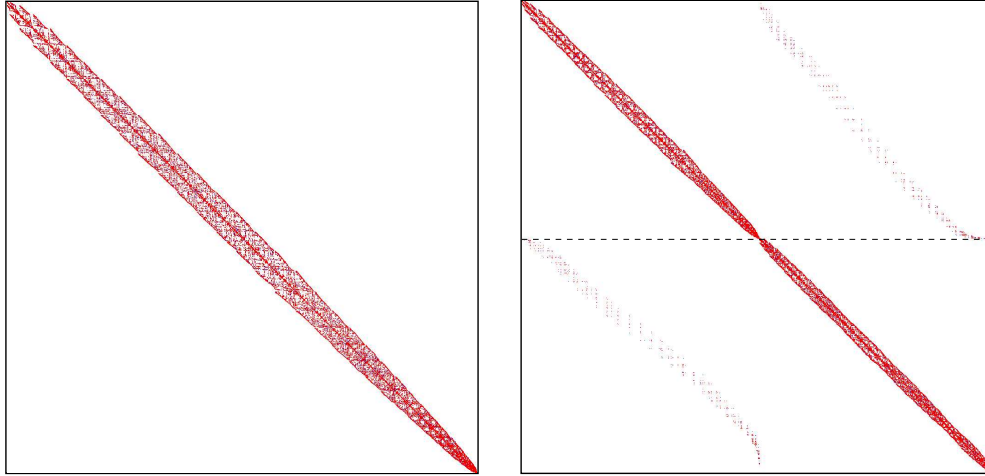
Figure 5.8: Sparsity pattern of the stiffness matrix of the nanodot model for a single processor (left) and distributed over two processors (right).

done for all nodes (including interior ones), the result can be checked against the boundary indicators obtained during the serial initialization, because the solid angle for all interior nodes has to be 4π, naturally.

For the data output along a sampling line through the model and for the graphics output the interpolation matrices are calculated (cf. Sec. 6.2.2). Then, the requested solver (PVODE for integration of the Landau-Lifshitz-Gilbert equation, TAO for energy minimization, or the solver for the nudged elastic band method) is initialized and all additionally required data structures are created.

The initialization phase is finally completed with the calculation of the local fields and energies of the initial magnetization distribution, first entries in the log files, and the removal of data structures, which are not needed any more.

5.2.3   Parallel Solution

The solution of the micromagnetic problem (cf. Fig. 5.10) is then carried out with the requested solver. All solvers require the calculation of local effective field Eq. (3.58) with simple matrix-vector multiplications. Since all matrices (except for the boundary matrix Eq. (3.48)) are sparse matrices,
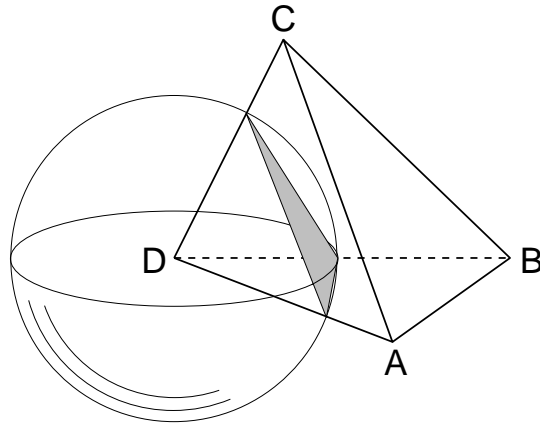
Figure 5.9: Solid angle of a trihedral angle made up by three faces of a tetrahedron.

these matrix-vector multiplications with distributed data are very efficient. If we assume a diagonal matrix with

$$a_{ij} = a_i \delta_{ij} \qquad (5.3)$$

the matrix-vector multiplication in Fig. 5.7 would not require any communication:

$$
\begin{aligned}
b_1 &= a_{11}x_1 \quad \ldots \text{all data on processor 1} \\
b_2 &= a_{22}x_2 \quad \ldots \text{all data on processor 1} \\
b_3 &= a_{33}x_3 \quad \ldots \text{all data on processor 2} \\
b_4 &= a_{44}x_4 \quad \ldots \text{all data on processor 2} \\
b_5 &= a_{55}x_5 \quad \ldots \text{all data on processor 3} \\
&\vdots
\end{aligned}
$$

However, if there are also some off-diagonal elements, then some communication is required:

$$
\begin{aligned}
b_1 &= a_{11}x_1 + a_{12}x_2 & \ldots \text{all data on processor 1} \\
b_2 &= a_{21}x_1 + a_{22}x_2 + a_{23}x_3 & \ldots x_3 \text{ from processor 2 required} \\
b_3 &= a_{32}x_2 + a_{33}x_3 + a_{34}x_4 & \ldots x_2 \text{ from processor 1 required}
\end{aligned}
$$

solution loop

perform iteration

calc. observables

data output

continue/abort
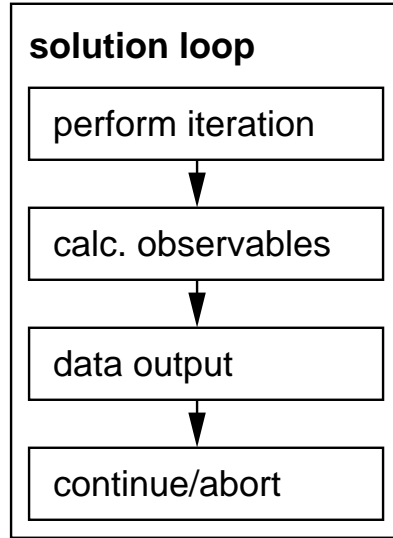
Figure 5.10: Flow chart of the solution loop.

$$b_4 = a_{43}x_3 + a_{44}x_4 + a_{45}x_5 \quad \ldots x_5 \text{ from processor 3 required}$$
$$b_5 = a_{54}x_4 + a_{55}x_5 + a_{56}x_6 \quad \ldots x_4 \text{ from processor 2 required}$$
$$\vdots$$

This gives a first idea, how distributed matrices and vectors and some linear algebra functions are handled. Yet, the user need not be concerned with these details since PETSc hides all the communication away and manages it internally.

For the integration of the LLG equation or the nudged elastic band method PVODE is called to make one time step. The energy minimization with TAO is performed until equilibrium has been reached. Then all required observables are calculated and written to a log file and additional data of the sampling line and graphics output are stored. Finally, several stopping criteria are checked and the simulation is continued with the next iterative step or it is aborted.
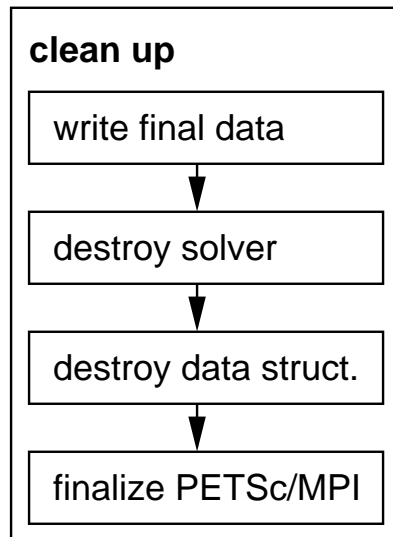
Figure 5.11: Flow chart of the final clean up section.

5.2.4   Clean Up

When the simulation has been completed, the final results are logged, the solvers are destroyed, all data structures freed and the program exits gracefully (cf. Fig. 5.11).

Chapter 6

Optimization

During the implementation of the micromagnetics application, special attention has been paid to the optimization with regard to speed and storage requirements. The former is strongly determined by good scaling properties of the program on multiple processors. The latter is not an issue for the memory (owing to the distributed data structures), but it can become a problem concerning the size of the data files, which are generated and stored on disk during a simulation.

6.1   Profiling

The timing of a serial (single processor, single threaded) program is usually measured as the "real CPU time" (the time which is spent executing commands of the program) by the kernel of the operating system. Thus, idle times during which the program is "sleeping" and waiting for other processes or i/o operations to complete are not taken into account.

On the contrary, the timing of a parallel program has to be done in terms of the elapsed time between its invocation and termination ("wall clock time"). Idle times of one of the different instances of the program indicate a load balancing problem, which may lead to a less than optimal scaling. As a result, careful profiling requires, that all instances have an equal environment on their processor (i.e. no other processes producing a high load should be running) and all timings have to made in terms of "elapsed wall clock time".

Accurate profiling of the application is supported by several PETSc features, which are activated with command line arguments for the PETSc application:

- `-log_summary` prints a summary of timing data and performance statistics at the end of the program. The impact on the overall performance of the program is very small.

- `-log_info` prints detailed information about data structures, solver performance and i/o operations. Printing these data on stdout or to a file slows down the program considerably, but it provides accurate information about specific parts of the program. If this option is selected, the execution of all subroutines of the micromagnetics application is timed individually.

6.2   Data I/O

Reading files from and writing them to disk is a quite slow process, but usually the total time spent with i/o operations is negligibly small as compared to the total execution time of the program. More important is the amount of data, which have to be stored. Due to the distributed data structures, the size of the finite element models can be increased (almost linearly) with the number of processors, if each of them has the same amount of private memory available. However, the generation of the FE models and the storage of the results to disk can become a problem.

6.2.1   Mesh Refinement

The requirements for a suitable finite element mesh have already been discussed in Sec. 2.4. In order to reduce the size of the initial finite element mesh, global or partial (adaptive) mesh refinement can be done at run time. Yet, in parallel programs adaptive refinement methods give rise to another difficulty and that is "load balancing" [70]. In order to get the maximum speed up, each processor working for a parallel program should be busy all the time, because delays and idle times reduce the overall performance.

Therefore, the problem is initially split up into parts, which will give each processor the same amount of work. To be more accurate, in a heterogeneous environment where machines and processors with different speeds and capabilities are used, the numerical problem has to be distributed in such a way, that all processors finish their tasks at the same time. Then they do not have to wait for each other, when they have to synchronize their results. Adaptive mesh refinement methods insert and remove finite elements (and therefore nodes) and modify the number of unknowns at run time. Thus, the computational effort will increase for processors working on a partition of the finite element mesh, where elements have been inserted, and decrease for those, where elements have been removed. Of course, this disturbs the initial load balancing and requires a new partitioning of the finite element mesh, redistribution of the current data to the processors and reinitialization before the calculation can be resumed. This scheme has been implemented in the finite element package "UG" [71, 72], whose data model is based on "Dynamic Distributed Data" [73], a software tool for distributed memory parallelization.

Nevertheless, global mesh refinement has been implemented, because it allows much smaller input data files and adds the flexibility of increasing the mesh resolution without remeshing the model with a mesh generator. The global refinement scheme is very simple, because it just splits up every finite element into eight "children" (cf. Fig. 6.1) [16]. The details of the implementation are discussed in Sec. 6.2.1. If this scheme is applied to the whole finite element mesh, its structure remains consistent. The quality of the mesh is preserved, because the four children in the corners of the parent element are congruent to the parent and the other four from the octahedron in the center have equal volumes, too. Even though they are not congruent with the parent, it has been shown, that at most three congruence classes occur. Thus, the stability of the generated triangulations is preserved. With every refinement step the number of finite elements increases by a factor of eight and the number of nodes approximately, too.

As a result, the input data files and especially the file containing the mesh geometry are much smaller. Even more important, the mesh generator does not have to generate a very fine and therefore large mesh, even though it has
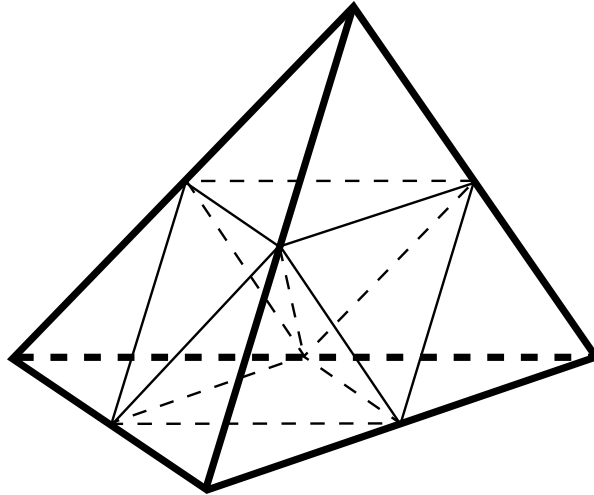
Figure 6.1: Global refinement of a "parent" tetrahedral finite element (thick lines) into eight "children" [16].

to be fine enough to resolve the details of the geometrical model and should give finite elements of good quality. Moreover, convergence of the results can be "easily" checked with a refined finite element mesh.

6.2.2   Data Output

For the direct output of graphics images, the PNG file format has been chosen, because it is widely supported (also by all newer WWW clients), generates very small, highly compressed files, it is not encumbered by any patents (like the GIF file format), and the reference library libpng [66] is freely available.

However, first the magnetization, which is defined on the nodes of the unstructured finite element mesh, has to be interpolated on a regular mesh in the desired slice plane. The slice plane is defined in the configuration file in the form

$$ax + by + cz = d \quad , \quad \boldsymbol{n} = \begin{pmatrix} a \\ b \\ c \end{pmatrix} \tag{6.1}$$

with the normal vector $\boldsymbol{n}$. Then all elements, which are cut by the slice plane have to be found. In order to simplify this task the whole model (simply the

Cartesian coordinates of the vertices) is translated and rotated in such a way, that the slice plane coincides with the x-y-plane. Then all elements which are cut by the x-y-plane – this is easily determined using the z-coordinates of the vertices – are tagged, and the maximum dimensions (the "bounding rectangle") of the finite element model in the slice plane are determined. For a given image size we can now calculate the Cartesian coordinates $\boldsymbol{P}$ of each pixel P, which then has to be assigned to one of the tagged elements, within which the pixel is located. This "point location problem", which is a standard problem in geographic information systems and computer-aided design and engineering [74], is the most time consuming part. However, the number of tagged elements (which are cut by the slice plane) is usually far smaller than the total number of elements, and so we can use a brute force yet clever approach, which takes advantage of some peculiarities of our specific problem.

In principle, for each pixel we have to search all tagged elements and determine if the pixel is inside or outside. But we can speed up the search by skipping those elements, for which the distance of the pixel from the first node is larger than the maximum edge length of any tetrahedron.

If a suitable element is found we calculate the barycentric coordinates $\boldsymbol{B}_P = (\alpha, \beta, \gamma, \delta)$ of the pixel. The barycentric coordinates are defined as the relative position of P inside the tetrahedron $ABCD$. In a "regular" tetrahedron (which has three edges coinciding with the coordinate axes) these correspond to the relative coordinates as indicated in Fig. 6.2.

$$\boldsymbol{P} = \alpha\boldsymbol{A} + \beta\boldsymbol{B} + \gamma\boldsymbol{C} + \delta\boldsymbol{D} \quad , \quad \delta = 1 - \alpha - \beta - \gamma \tag{6.2}$$

If we solve for (α, β, γ) we get a simple linear system of equations

$$\begin{pmatrix} \alpha \\ \beta \\ \gamma \end{pmatrix} = (\boldsymbol{A} - \boldsymbol{D}|\boldsymbol{B} - \boldsymbol{D}|\boldsymbol{C} - \boldsymbol{D})^{-1} \cdot (\boldsymbol{P} - \boldsymbol{D}) \tag{6.3}$$

The point P is inside the tetrahedron if and only if

$$\alpha, \beta, \gamma, \delta \geq 0 \quad , \tag{6.4}$$
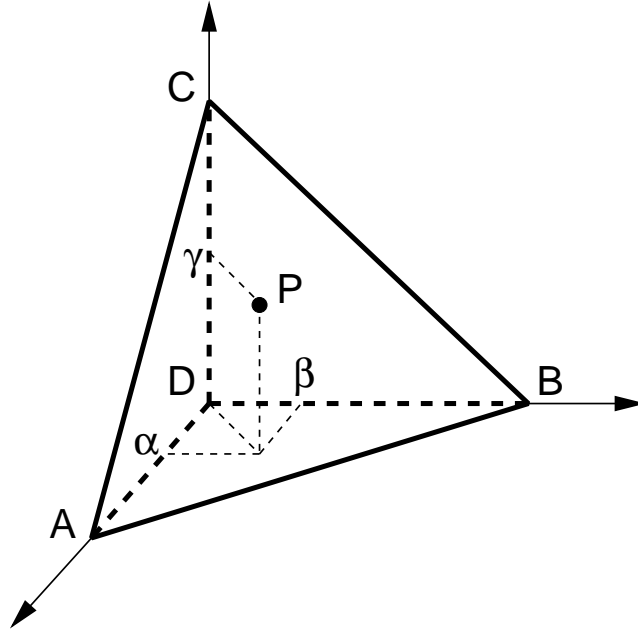
Figure 6.2: Barycentric coordinates in a regular tetrahedron.

which is equivalent to

$$\alpha, \beta, \gamma \geq 0 \quad \text{and} \quad \alpha + \beta + \gamma \leq 1 \quad . \tag{6.5}$$

The barycentric coordinates $(\alpha, \beta, \gamma, \delta)$ give the weight, by which the data values at the corresponding vertices of the tetrahedron contribute to the linear interpolation at P. Thus, for some data x_i defined on the vertices of the tetrahedron, we find the linear interpolation at P with

$$x_P = \alpha x_A + \beta x_B + \gamma x_C + \delta x_D \quad . \tag{6.6}$$

As a result we can assemble an interpolation matrix, which calculates the magnetization for all pixels of the image. Let $\boldsymbol{M}_{\text{FE}}$ denote the PETSc vector of one Cartesian component of the magnetization of all nodes of the finite element mesh and $\boldsymbol{M}_{\text{ip}}$ the PETSc vector of interpolated values, then we have

$$\boldsymbol{M}_{\text{ip}} = A_{\text{ip}} \boldsymbol{M}_{\text{FE}} \tag{6.7}$$

with the $(m \times n)$ interpolation matrix ($m = a \times b$ rows for images with
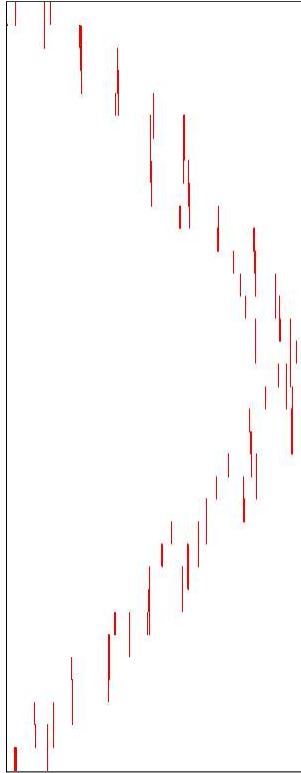
Figure 6.3: Sparsity pattern of the interpolation matrix for graphics output.

$a \times b$ pixels and n columns for a finite element mesh with n nodes). The matrix elements $A_{ij,\mathrm{ip}}$ are given by the barycentric coordinate of pixel P_i corresponding to node with the global index j of the finite element, in which the pixel is located. This matrix is very sparse (cf. Fig. 6.3 for the sparsity pattern of the nanodot model), as it has only four entries per row (the four barycentric coordinates of a given pixel).

Since the interpolation matrix depends only on the triangulation, we can calculate it during the initialization phase of the program. Whenever a snapshot of one magnetization component should be stored to disk, a simple matrix-vector multiplication gives the interpolated values at the pixel positions. Then the data are color coded using the scheme shown in Fig. 6.4. Finally, the PNG library [66] is called to convert these data into a PNG graphics file.

In addition to snapshots of the magnetization it is often desirable to
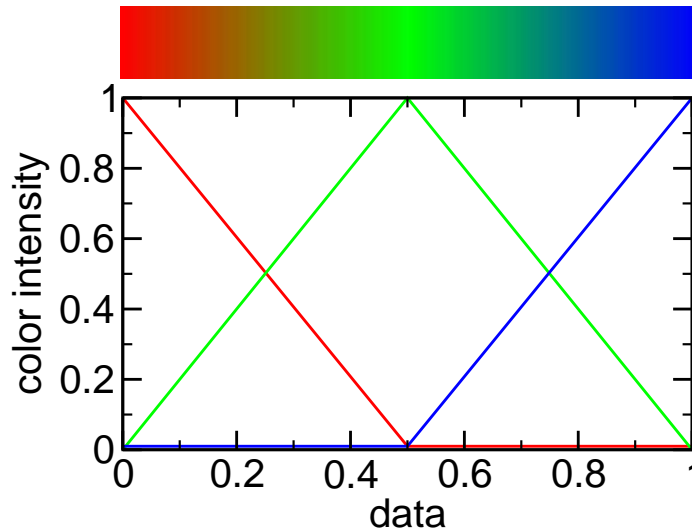
Figure 6.4: RGB color intensities for data encoding and resulting color map.

measure some data along a probing line through the model. This feature has been implemented based on the algorithm described above. For the probing line we translate and rotate the model to make the probing line coincide with the x-axis. Then we tag all elements, which are cut by the x-axis and determine the barycentric coordinates of every point on the sampling line. We finally end up with another interpolation matrix, which calculates the data values along the probing line. These can then be stored in a data file on disk.

Finally, the complete set of data, which includes the magnetization, the magnetic scalar potential, and the local fields are stored in files in UCD format [75]. This file format can be read by many advanced visualization packages like AVS [76] and MicroAVS [77]. However, the (human-readable) ASCII UCD format generates huge files, because the whole finite element mesh is stored in each file. Thus, two measures have been taken to tackle this problem.

First, the finite element mesh is stored in a single separate file in UCD format during the initialization phase. The data files, which are generated during the simulation are then stored without the mesh definition, which saves about 50% of disk space. Secondly, the data files are compressed using the zlib-library [65] in gzip-compatible format, which shrinks the data to

about 30% of their initial size. Thus, we end up with data files, which require only 15% of the uncompressed storage space. To restore the data in proper UCD format, a simple shell script uncompresses the data and merges them with the mesh data. Alternatively, there is also a binary UCD format, which gives smaller files than the standard ASCII format, but it is not as widely supported and may lead to compatiblity problems, when the files are transferred to machines with different hardware architecture and operating system.

6.3 Performance

The performance (the speedup in particular) of the micromagnetics application has been measured on a Compaq SC45 cluster consisting of 11 nodes Alpha Server ES45 with 4 Alpha processors (EV68 @ 1 GHz, 8 MB Cache/CPU) and 16 GB of shared memory each. The nodes are interconnected with a Quadrics switch, which provides a maximum MPI bandwidth of 600 MB/s. Since this machine has been shared with several other users, up to 24 processors have been available for speedup measurements.

The speedup has been measured as

$$S_P = \frac{t_1}{t_P} \quad ,$$

where t_1 is the execution time of the program for a given problem on a single processor and t_P is the execution time for the same problem on P processors [78].

The energy minimization method, which uses the LMVM method of the TAO package (cf. Sec. 4.1), has been applied to calculate the nucleation field of FePt nanoparticles (cf. Sec. 8.3). The timing results are summarized in Fig. 6.5. On 8 and 16 processors we find a "superlinear" behavior of the solution part of the application. This is a well known phenomenon in parallel computing and can be attributed to caching effects. As the same total amount of data is distributed over more processors, the relative amount decreases and may reach a size, where it fits into the fast cache memory of modern computer architectures. As a result, the data need not be fetched

from the main memory (which is a lot slower than the cache memory) and the calculations are completed a lot faster. However, as ever more processors are used, communication requires more and more time which eventually leads to a saturation of the speedup factor.

The parallel time integration using PVODE is not as efficiently parallelized as the TAO package, which is shown in Fig. 6.6.

For comparison, Tab. 6.7 shows the speedup obtained on a Beowulf type cluster of 900 MHz AMD PCs running Linux [79] (for a different problem). These machines are linked with a standard switched 100 MBit Ethernet network.
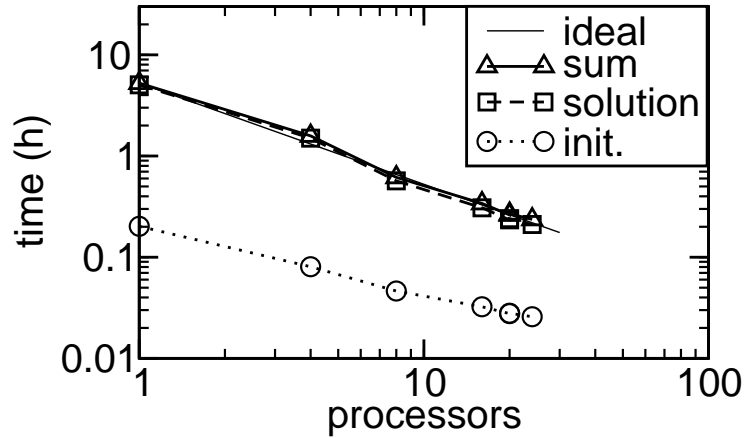
processors	CPU time (h)	speedup
initialization		
1	0.202	1.00
4	0.080	2.52
8	0.046	4.38
16	0.032	6.26
20	0.027	7.33
24	0.025	7.86
solution		
1	5.047	1.00
4	1.500	3.36
8	0.568	8.87
16	0.307	16.41
20	0.233	21.57
24	0.210	23.97
total		
1	5.249	1.00
4	1.581	3.32
8	0.615	8.53
16	0.339	15.44
20	0.261	20.06
24	0.236	22.20

Figure 6.5: Speedup of initialization, solution, and total execution time of the parallel energy minimization algorithm (TAO) on an AlphaServer.
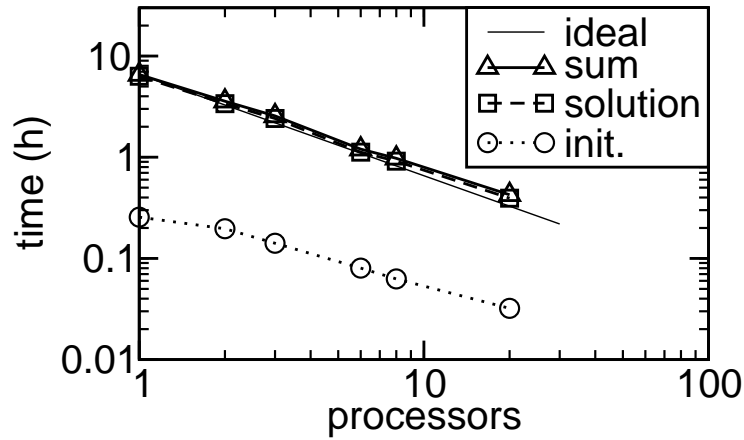
processors	CPU time (h)	speedup
initialization		
1	0.255	1.00
2	0.196	1.30
3	0.141	1.81
6	0.080	3.19
8	0.062	4.07
16	0.037	6.73
20	0.032	7.96
solution		
1	6.309	1.00
2	3.379	1.86
3	2.416	2.61
6	1.120	5.63
8	0.913	6.91
16	0.451	13.98
20	0.393	16.03
total		
1	6.565	1.00
2	3.576	1.83
3	2.557	2.56
6	1.200	5.46
8	0.975	6.72
16	0.489	13.42
20	0.425	15.42

Figure 6.6: Speedup of initialization, solution, and total execution time of the parallel time integration (PVODE) on an AlphaServer.
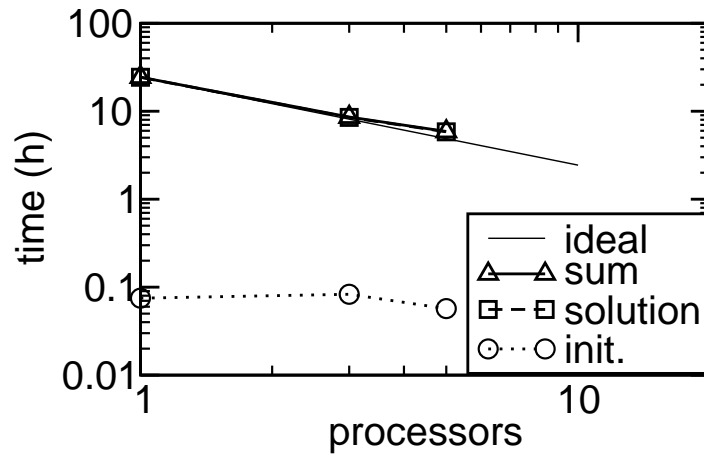
processors	CPU time (h)	speedup
initialization		
1	0.075	1.00
3	0.083	0.91
5	0.057	1.32
solution		
1	24.334	1.00
3	8.5059	2.86
5	5.8314	4.17
total		
1	24.41	1.00
3	8.589	2.84
5	5.889	4.15

Figure 6.7: Speedup of initialization, solution, and total execution time of the parallel time integration (PVODE) on a Beowulf type AMD cluster.

Chapter 7

Domain Wall Pinning in SmCo Permanent Magnets

The coercivity mechanism of precipitation hardened SmCo permanent magnets is dominated by the pinning of magnetic domain walls on the precipitation structure. In this chapter the microstructure of these magnets is determined using transmission electron micrographs and simplified models are developed. The basics of the pinning mechanism on planar interfaces, intercellular phases and a simple cell structure are investigated using micromagnetic simulations and compared with an analytical model. Then, a model of the rhomboidal cell structure is used to study attractive and repulsive pinning for different material parameters and material compositions.

7.1   Introduction

Samarium-Cobalt type permanent magnets were discovered in the 1960's by Strnat and coworkers [1]. The high magnetic moment of Sm and Co as well as the high magnetocrystalline anisotropy are the reason for the excellent magnetic properties of this material. As compared to NdFeB type magnets SmCo magnets have superior properties at elevated temperatures due to their high Curie temperatures ($720\,°C$ for $SmCo_5$ and $820\,°C$ for Sm_2Co_{17} [80]) and low temperature coefficients of coercivity, which makes it the best material currently available for high temperature magnets.

Thus, the HITEMAG project of the European Union [2], whose objective is the development and optimization of magnetic materials for high temperature applications, concentrates on this material.

7.2 Experimental Characterization

Precipitation hardened $Sm(Co,Fe,Cu,Zr)_{7.5-8}$ magnets are classified as "pinning controlled" [81, 82] and their behavior arises from the cellular precipitation structure, which is observed in transmission electron micrographs. Figs. 7.1, 7.2 show the microstructure of typical $Sm(Co,Fe,Cu,Zr)_{7.5-8}$ type magnets. The magnetic properties are determined by the fine cell morphology with rhomboidal cells of $Sm_2(Co,Fe)_{17}$ with a typical diameter of 100–200 nm, which are separated by a boundary phase of $Sm(Co,Cu,Zr)_{5-7}$ [83]. The cellular precipitation structure is formed during a lengthy production process with sophisticated heat treatment, which includes sintering, homogenizing, quenching, isothermal aging, and annealing [12]. Its development is determined by the direction of zero deformation strains due to the lattice misfit between the different phases [84]. The quality of this intercellular phase strongly depends on the additives, especially Zr and Cu. Cu is concentrated in the intercellular "1:5" phase, whereas Zr is mainly found in the lamellar structure of the Z-phase and provides a diffusion path for Cu segregation.

Foucault images of Lorentz electron microscopes show that the cellular precipitation structure acts as a pinning site for magnetic domain walls (Fig. 7.3) [85, 86, 87, 12]. The difference in composition between the cells and the cell boundary phase gives rise to a difference in the magnetocrystalline anisotropy. As a result it is energetically favorable for a magnetic domain wall either to stay in the cell boundary phase ("attractive domain wall pinning" if the domain wall energy is lower) or just inside the cells ("repulsive domain wall pinning" if the domain wall energy in the cell boundary phase is higher than that in the cells) [88].
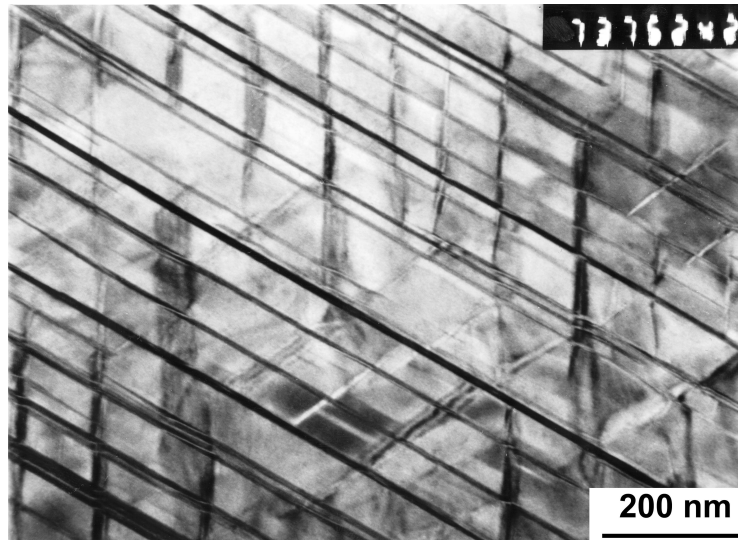
Figure 7.1: TEM micrograph of the microstructure of a $Sm(Co,Fe,Cu,Zr)_z$ precipitation hardened magnet. The lamella phase perpendicular to the [0001] direction of the cell matrix phase gives strong contrast in this image [89].
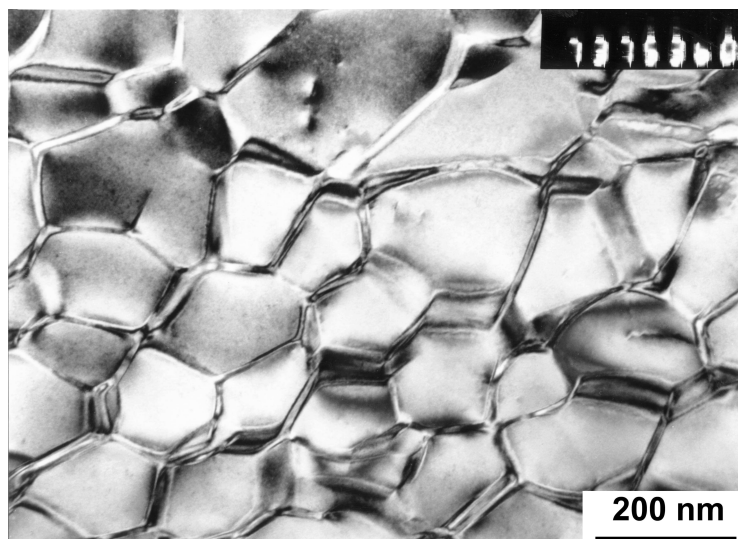
Figure 7.2: Bright field TEM micrograph of the cellular precipitation structure of a $Sm(Co,Fe,Cu,Zr)_z$ magnet. The $Sm_2(Co,Fe)_{17}$ cells are surrounded by $Sm(Co,Cu)_5$ cell boundaries [89].

Figure 7.3: Lorentz electron micrograph of a $Sm(Co,Fe,Cu,Zr)_z$ magnet. The magnetic domain wall between two domains with opposite magnetization (bright and dark cells) is pinned on the precipitation structure [87].

7.3 Simplified models

7.3.1 Pinning on a Planar Interface

If a perfect interface with a discontinuity in the material parameters is assumed, a one-dimensional micromagnetic model can be calculated analytically. Schrefl [90] has calculated the nucleation field for two neighboring grains with 90° misoriented easy axes. Kronmüller and Goll [91] have presented a model for grains with parallel easy axes but a step-like change in the material parameters at the interface. Finally, Della Torre et al. [92] have assumed a variation of the exchange energy as a function of position and they have obtained results for a square well and Gaussian decrease.

Our simplest geometrical model of the pinning process includes two different materials (different saturation polarization J_s, uniaxial magnetocrystalline anisotropy K_1 and exchange constant A) with a perfectly planar interface assuming a step like change [91] of the material parameters (cf. Fig. 7.4). Typical values for $Sm(Co,Fe,Cu,Zr)_z$ magnets can be found in Tab. 7.1. However, the simulations are independent of the choice of A and K_1, only the exchange length $l_{ex} = \sqrt{A/K_1}$ is relevant. If an ideal Bloch wall is assumed,
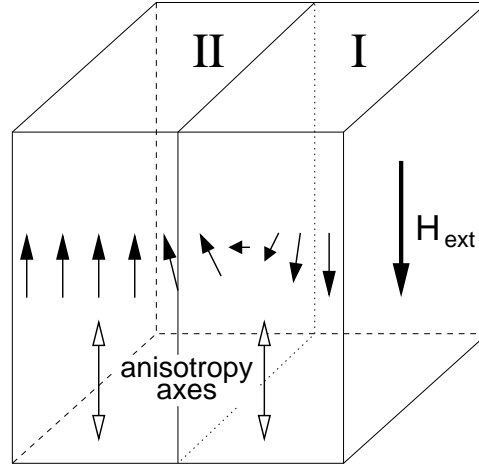
Figure 7.4: Model geometry for domain wall pinning on a perfectly planar interface with parallel anisotropy axes. The chain of arrows indicates the magnetization distribution of a pinned domain wall.

the pinning field, which is required to force the domain wall into the hard material (with higher domain wall energy), can be calculated with the 1D analytical model of Kronmüller and Goll [91]. The micromagnetic simulation is initialized with a Bloch wall in the softer material (I) and the external field pushes it towards the interface into the harder material (II) (cf. Fig. 7.4).

The comparison with the micromagnetic simulations shows, that the edge length of the finite elements has to be smaller than the exchange length (e.g. 1.8 nm in Sm_2Co_{17} [91]) of the harder material in order to avoid "artificial pinning" on the finite element mesh (cf. Sec. 7.3.4). Fig. 7.5 shows the dependence of the pinning field H_{pin} (in units of the anisotropy field $H_{ani}^{II} = 2K_1^{II}/J_s^{II}$) on the ratio of exchange ($\varepsilon_A = A^I/A^{II}$) and anisotropy constants ($\varepsilon_K = K_1^I/K_1^{II}$). The thick curve represents $\varepsilon_A \cdot \varepsilon_K = 1$, where the two materials have equal domain wall energy and therefore exhibit no domain wall pinning ($H_{pin} = 0$). Only that part with $H_{pin} > 0$ is physically relevant. The pinning field is always smaller than the anisotropy field. For given ε_A the pinning field is proportional to ε_K. However, if ε_A is reduced (which decouples the two materials), the coercive field shows a steep increase towards the anisotropy field. Thus, in order to reach high pinning fields, a low ε_A ratio has to be achieved.
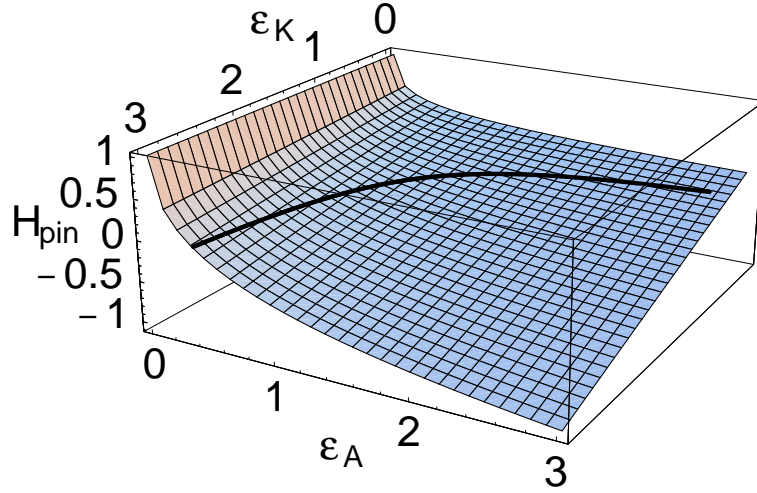
Figure 7.5: Dependence of the pinning field H_{pin} (in units of the anisotropy field of material II) on the ratio of exchange (ε_A) and anisotropy constants (ε_K) for given A^{II} and K_1^{II} according to a 1D analytical model [91]. The thick curve represents $\varepsilon_A \cdot \varepsilon_K = 1$, where the two materials have equal domain wall energy and $H_{\mathrm{pin}} = 0$.

When the external field is switched on, the domain wall moves towards the interface and gets pinned. As the external field increases the Bloch wall is more and more forced into the "harder material" until it depins and propagates further through the "harder material". The analytical result has been calculated with the one dimensional model of Kronmüller and Goll [91], which gives the pinning field as

$$H_{\mathrm{pin}} = \frac{2K_1^{\mathrm{II}}}{J_{\mathrm{s}}^{\mathrm{II}}} \frac{1 - \varepsilon_A \varepsilon_K}{(1 + \sqrt{\varepsilon_A \varepsilon_J})^2} \quad , \tag{7.1}$$

where

$$\varepsilon_J = \frac{J_{\mathrm{s}}^{\mathrm{I}}}{J_{\mathrm{s}}^{\mathrm{II}}} \quad , \quad \varepsilon_A = \frac{A^{\mathrm{I}}}{A^{\mathrm{II}}} \quad , \quad \varepsilon_K = \frac{K_1^{\mathrm{I}}}{K_1^{\mathrm{II}}} \tag{7.2}$$

and (I) denotes the material parameters of the softer material and (II) those of the harder material.

	"2:17" type	"1:5" type
	cells	boundary phase
J_s (T)	1.3	0.8
A (pJ/m)	14.0	14.0
K_1 (MJ/m^3)	5.0	9.0
$l_{ex} = \sqrt{A/K_1}$ (nm)	1.7	1.3
$\delta = l_{ex} \cdot \pi$ (nm)	5.3	3.9
$H_{ani} = 2K_1/J_s$ (kA/m)	7692	22500

Table 7.1: Material parameters of typical $Sm(Co,Fe,Cu,Zr)_z$ permanent magnets [80, 93, 94, 91].

7.3.2   Pinning on an Intercellular Phase

Then the influence of the thickness t of an intercellular phase (a coherent precipitation) on coercivity has been investigated using a finite element micromagnetic model with static energy minimization. As compared to the simple planar interface, we now have three regions (cf. Fig. 7.6). The outer regions (indicated with "I") represent the cells, whereas the center region (indicated with "II") represents the intercellular phase. In $Sm(Co,Fe,Cu,Zr)_z$ precipitation hardened magnets, the SmCo 2:17 cells are separated by a thin SmCo 1:5 intercellular phase. Depending on the Cu content of this cell boundary phase, its domain wall energy might be lower (high Cu content) or higher (low Cu content) than that of the cells giving rise to "attractive" or "repulsive pinning", respectively.

   In the former case, the domain wall prefers to stay in the intercellular phase, where it has a lower energy. However, its thickness has to be large enough so that the wall "fits in" [95]. Fig. 7.7 shows the dependence of the pinning field on the thickness of the intercellular phase in comparison with the ideal case of an intercellular phase of infinite thickness (where it reduces to "pinning on a planar interface"). Analogously, the intercellular phase has to be thick enough to provide an energy barrier in the case of repulsive pinning. The results are also shown in Fig. 7.7, where the axes have been scaled to the exchange length of the intercellular phase and the
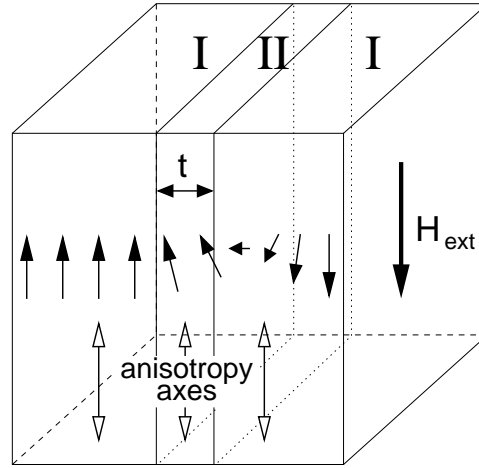
Figure 7.6: Model geometry for domain wall pinning on an intercellular phase with parallel anisotropy axes. The chain of arrows indicates the magnetization distribution of a pinned domain wall.

field to the pinning field for infinite thickness of the precipitation (which is 2200 kA/m in $Sm(Co,Fe,Cu,Zr)_z$ [91]). As a result, the thickness of the intercellular phase has to be at least three times the exchange length. This corresponds to the domain wall width (which is usually defined as $\pi \cdot l_{ex}$). For thinner precipitations the domain wall can either "tunnel" through the intercellular phase (repulsive pinning) or it does not fit into it (attractive pinning). Fig. 7.7 clearly emphasizes the similarity in behavior between attractive and repulsive pinning, which has not been covered in [95]. A misalignment of the anisotropy axes with respect to the interfaces up to $40°$ has not shown any major influence on the pinning fields, provided the external field is applied parallel to the anisotropy axes. Such canted anisotropy axes give rise to magnetic charges at the interface, which generate a magnetostatic field. However, it is too small as compared to the anisotropy field to have any significant impact on the pinning field.

7.3.3   Pinning on the Cell Structure

Then the influence of the cell boundary phase perpendicular to the domain wall has been studied. The geometry is shown in Fig. 7.8. It resembles the situation of a domain wall, which moves from the right to the left and gets
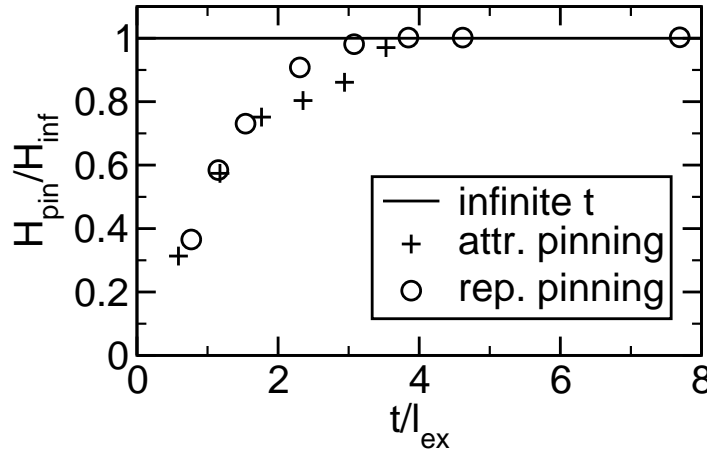
Figure 7.7: Pinning field for attractive and repulsive pinning as a function of the thickness t of the intercellular phase. The thickness is given in units of the exchange length of the intercellular phase. The pinning field is given in units of the pinning field for infinite t.

trapped in the (softer) intercellular phase ("I"), where it is repelled by the cells ("II"). The interesting question is, if the pinning field is changed by the cellular structure as compared to the perfect planar interfaces discussed above. The results are given in Fig. 7.9, where the pinning field (normalized to the pinning field for $t = 0$, which corresponds to the planar interface again) is given as a function of the relative thickness t/T of the intercellular phase. T is the sum of the edge length of a cell and the thickness of the intercellular phase t. In Fig. 7.8 the "hard surface area" of the cells is indicated by the shaded faces. Obviously, the pinning field depends linearly on the relative thickness of the intercellular phase. Even if the whole model is scaled to twice or three times its size (i.e. the cell size is increased by a factor of two or three) we find the same behavior, because the relative thickness remains constant (cf. data marked "area x2" and "area x3" in Fig. 7.9).

If we switch to the case of repulsive pinning again, we can assume that now the cells ("II") are softer than the intercellular phase ("I") in Fig. 7.8. In this case the domain wall moves from left to right and gets pinned in front of the intercellular phase. The pinning fields are also given in Fig. 7.9. They show the same linear behavior as in the case of attractive pinning. However, in a fully developed cell structure the possible range of values for
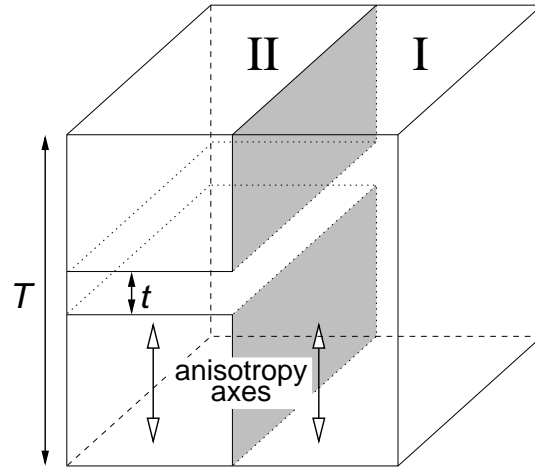
Figure 7.8: Model geometry for domain wall pinning on a coherent precipitation structure (with parallel anisotropy axes). The shaded areas indicate the faces of the cells, where the magnetic domain wall gets pinned.

the thickness t are restricted by a minimum (cf. Fig. 7.7) below which the domain wall does not fit in and a maximum (cf. Fig. 7.21) above which the whole intercellular phase is reversed.

For $Sm(Co,Fe,Cu,Zr)_z$ precipitation hardened magnets, this means, that the pinning field increases with the cell size. However, it decreases linearly with the thickness of the intercellular phase, if it is larger than the domain wall width. Below this limit the pinning field is strongly reduced. These results are independent, whether attractive or repulsive pinning is dominating. Thus, the best magnetic properties should be found in magnets with large cells, thin (but still sufficiently thick) intercellular phases, and large differences in the domain wall energy (ideally a large difference in the exchange constants).

7.3.4 Artificial Pinning

The influence of the space discretization using the finite element mesh has been investigated in more detail, because the magnetic domain walls in permanent magnets like SmCo are very thin. Thus, a high resolution mesh with very small elements is required where domain walls occur.

A very homogeneous finite element mesh with 59491 elements and 11085
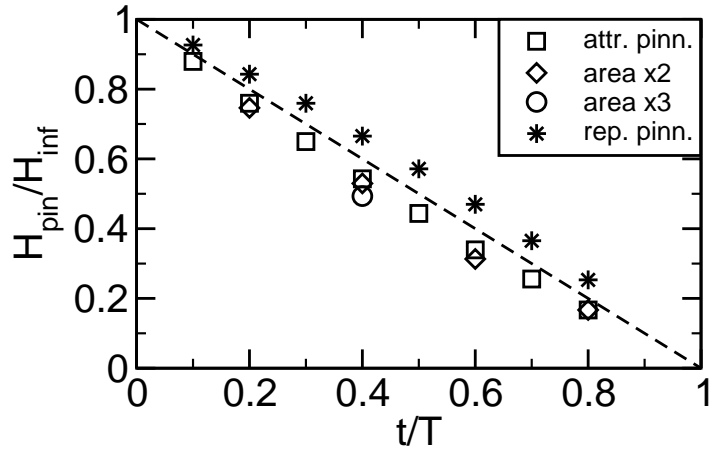
Figure 7.9: Pinning field for attractive and repulsive pinning of a magnetic domain wall on the cell structure as a function of the relative thickness t/T. The data marked "area x2" and "area x3" have been obtained with a model scaled to twice and three times the initial size. The dashed line is just a guide to the eye.

vertices has been used. The minimum edge length of any edge connecting two vertices in the finite element mesh is 0.29, the maximum edge length is 1.02 and the average is 0.56. The simulations are initialized with a magnetic domain wall in the center of the softer material (cf. Fig. 7.4). Then the magnetization is relaxed in zero field, so it can obtain its true minimum energy state. The domain wall energy as a function of the average edge length in units of the exchange length is shown in Fig. 7.10. The result for the domain wall energy remains almost constant. However, as the average edge length increases (the mesh is scaled up) the exchange energy increases while the magnetocrystalline anisotropy energy decreases and cancels the error in the former.

When the external field is switched on, the domain wall moves towards the interface and gets pinned. As the external field increases the Bloch wall is more and more pushed against the interface until it depins and propagates further through the harder material. The simulation results for different scaling are given in Fig. 7.11. The analytical result has been calculated with the one dimensional model of Kronmüller and Goll [91] (cf. Eq. (7.1)).

Fig. 7.12 summarizes the pinning fields, which have been obtained from
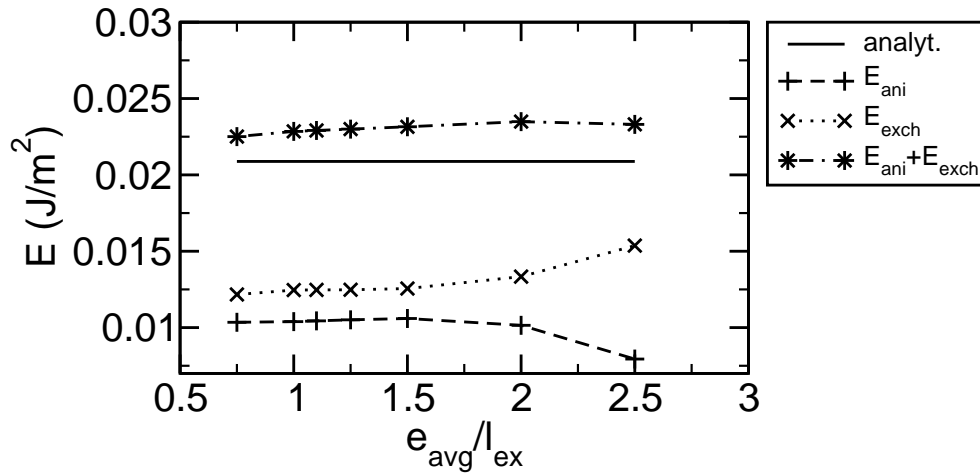
Figure 7.10: Domain wall energy as a function of the average edge length of the finite element model. The average edge length is given in units of the exchange length. The solid line indicates the analytical Bloch wall energy $4\sqrt{AK_1}$.
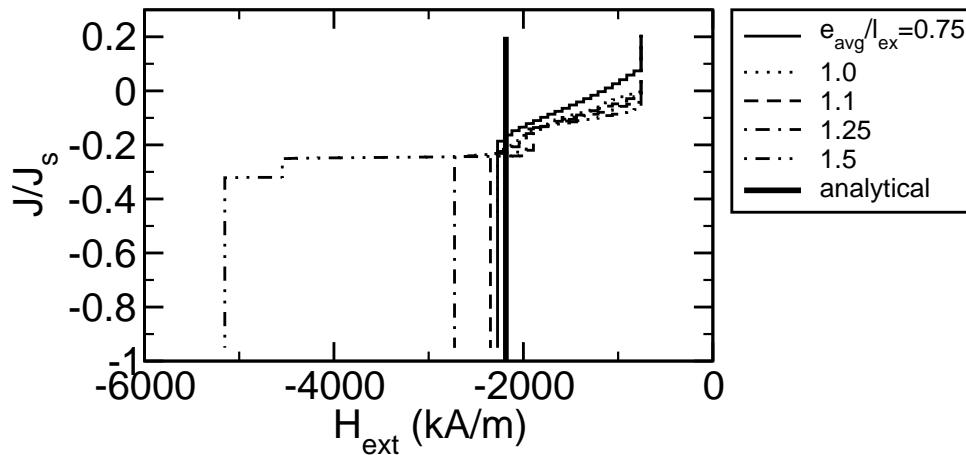
Figure 7.11: Demagnetization curves for different average edge length of the finite element model. The analytical pinning field has been calculated with the model presented in Sec. 7.3.1.
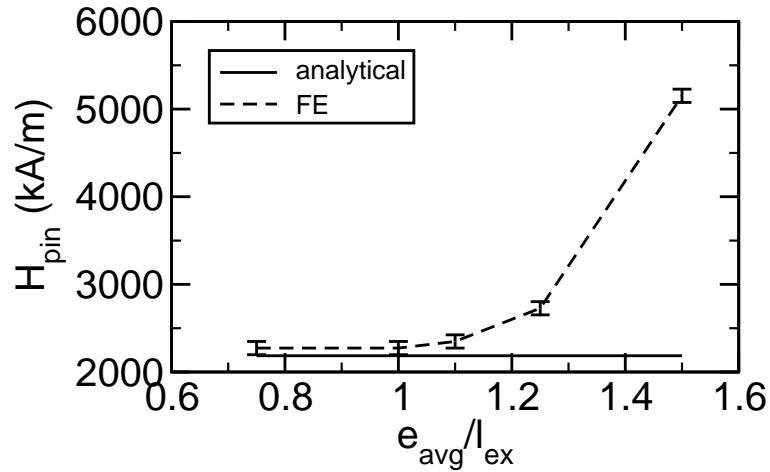
Figure 7.12: Pinning fields for different average edge length of the finite element model. As the mesh size increases the domain wall gets artificially pinned on the finite element mesh.

the demagnetization curves in Fig. 7.11. The error bars indicate the step size by which the external field has been increased, when the magnetization distribution reached equilibrium. Thus, the finite element simulation gives the correct pinning fields within its numerical limits.

In conclusion, the (average) edge length of a very homogeneous finite element mesh has to smaller or at most equal to the exchange length of the material. For inhomogeneous finite element meshes, the maximum edge length has to be considered because domain walls can get stuck in very coarse parts of the mesh.

7.4 Rhomboidal Cell Structure

A finite element model of the microstructure of $Sm(Co,Fe,Cu,Zr)_z$ has been developed. It consists of $2 \times 2 \times 2$ rhomboidal cells with a spacer layer for the cell boundary phase in between (see Fig. 7.13). The edge length e and the "corner angle" β of the rhombohedrons as well the thickness t of the precipitation are variable. The "space diagonal" D is parallel to the easy axis. The domain wall of the initial magnetization distribution of our simulations lies in the plane, which is indicated by the thick lines.
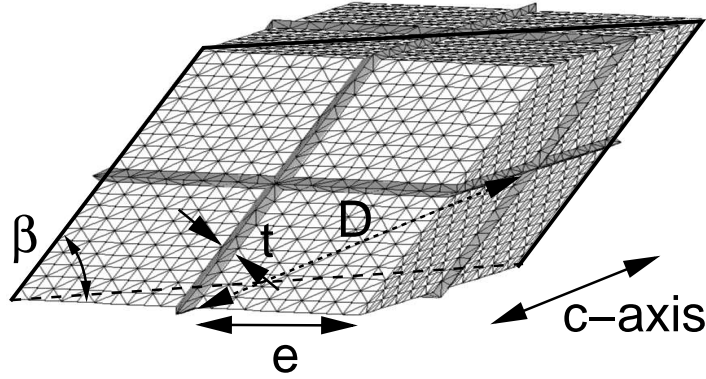
Figure 7.13: Finite element model of the rhomboidal cell structure of precipitation hardened $Sm(Co,Fe,Cu,Zr)_z$ magnets.

We have assumed the following material parameters for 300 K [80]: For the cells ("2:17" type) $J_s = 1.32$ T, $A = 14$ pJ/m, $K_1 = 5$ MJ/m^3. For the cell boundary phase ("1:5" type) we have used $J_s = 0.8$ T, $A = 14$ pJ/m, $K_1 = 1.9$ MJ/m^3. The resulting exchange length is 1.7 nm in the cells and 2.7 nm in the cell boundary phase. Thus, the domain wall width is 5.3 nm in the cells and 8.5 nm in the cell boundary phase.

These material parameters with lower anisotropy in the intercellular phase as compared to the cells give rise to "attractive pinning", which means, that the domain wall prefers to move into the intercellular phase and stays there pinned.

7.4.1   Attractive and Repulsive Pinning

We have studied the influence of the material parameters by varying the anisotropy constant K_1 of the precipitation between 0.4 MJ/m^3 (to mimic almost isolated cells or a close to paramagnetic - Cu rich - intercellular phase, A and J_s have also been reduced) and the value for the cells. The demagnetization curves in Fig. 7.14 have been obtained for cells with $e = 50$ nm and $\beta = 60°$, which gives $D \approx 125$ nm, and $t = 5$ nm. For very low values of the anisotropy constant we find a very strong pinning effect (horizontal plateau in the demagnetization curve in Fig. 7.14). As K_1 approaches the value for the cells (2:17 phase) the pinning effect disappears.
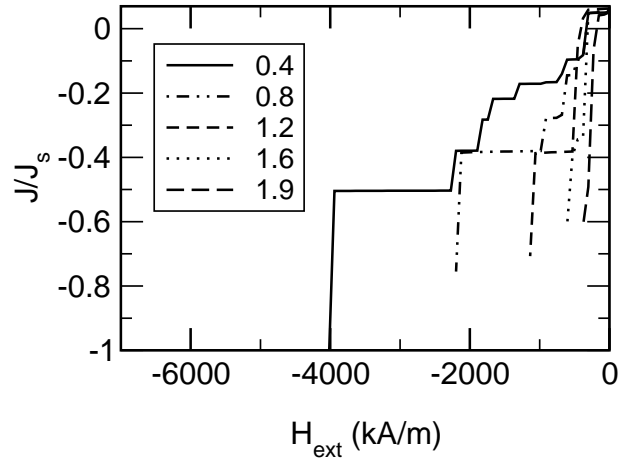
Figure 7.14: Demagnetization curves for reduced magnetocrystalline anisotropy K_1 of the cell boundary phase (values in the legend in MJ/m^3) – attractive pinning.

If the magnetocrystalline anisotropy of the intercellular phase is larger than that of the cells, the second possible pinning mechanism is found: "repulsive pinning".

The demagnetization curves for repulsive pinning and different values of the anisotropy constant of the intercellular phase are shown in Fig. 7.15. For only slightly enhanced values of the anisotropy constant K_1 we find no pinning, but for $\Delta K_1 \geq 4.0$ MJ/m^3 the pinning field reaches 1.5 kA/m. In this regime the pinning field is directly proportional to ΔK_1. The results for attractive and repulsive pinning are summarized in Fig. 7.16. In addition it shows a comparison with the analytical model mentioned in Sec. 7.3.1. Obviously, the pinning fields are smaller than those expected from the analytical model. This effect has to be ascribed to the influence of thickness of the intercellular phase and the cell structure as described in Sec. 7.3.

7.4.2 Influence of the Thickness of the Intercellular Phase

However, not only the material composition and material parameters, but also the geometry of the cellular structure has an important influence on the magnetic properties. The influence of the cell size has been studied
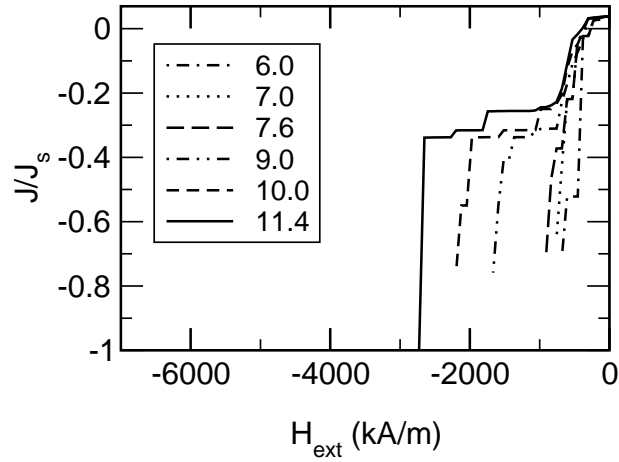
Figure 7.15: Demagnetization curves for enhanced magnetocrystalline anisotropy K_1 of the cell boundary phase (values in the legend in MJ/m^3) – repulsive pinning.
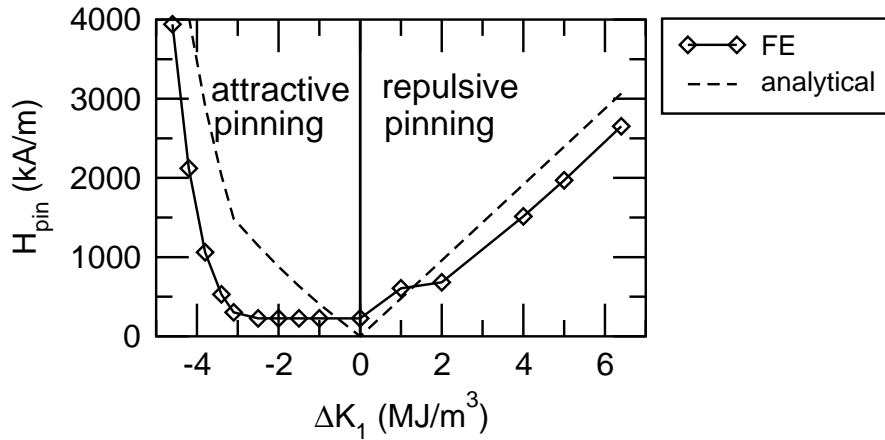
Figure 7.16: Pinning field vs. difference in anisotropy constant between the cells and the cell boundary phase in a 3D model of the rhomboidal SmCo microstructure and comparison with the analytical 1D model of Kronmüller, Goll [91].
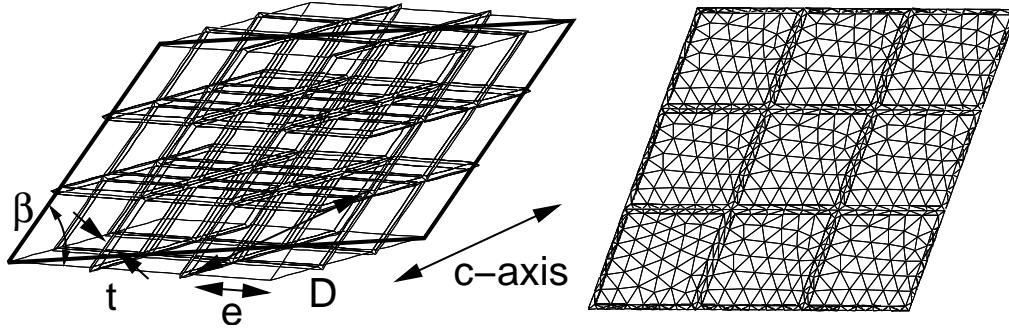
Figure 7.17: Finite element model with $3 \times 3 \times 3$ cells.

previously [96] and it showed a strong increase with increasing size of the cells (when the composition of the magnet was kept constant by increasing the cell boundary, too). We have investigated solely the influence of the thickness of the cell boundary phase on the domain wall pinning and the pinning field, but kept the cell size constant. This time we have used a larger model of $3 \times 3 \times 3$ cells and larger cells with $e = 100$ nm and $\beta = 60°$, which gives $D \approx 250$ nm (cf. Fig. 7.17). The thickness has been varied from $t = 2.5$ nm to $t = 40$ nm and the material parameters for the "2:17" cells and the "1:5" intercellular phase at 300 K given above have been used.

As we are varying the thickness, the ratio of the volume of the cells $V_{2:17}$ to the volume of the cell boundary phase $V_{1:5}$ changes. Thus, the composition and the z-value changes. These data are summarized in Tab. 7.2, where a volume of $V_{\mathrm{e}}^{2:17} = 0.24853 \, \mathrm{nm}^3$ and $V_{\mathrm{e}}^{1:5} = 0.0859 \, \mathrm{nm}^3$ for the elementary cells of the "2:17-type" cells and the "1:5-type" cell boundary phase, respectively, have been assumed [97]. The z-value is determined by

$$z = \frac{17 \cdot V_{2:17}/V_{\mathrm{e}}^{2:17} + 5 \cdot V_{1:5}/V_{\mathrm{e}}^{1:5}}{2 \cdot V_{2:17}/V_{\mathrm{e}}^{2:17} + 1 \cdot V_{1:5}/V_{\mathrm{e}}^{1:5}} \quad ,$$

where all additives have been neglected.

The demagnetization curves given in Fig. 7.19 show, that for a very thin cell boundary phase (2.5 nm, 5 nm) the effect of domain wall pinning vanishes, because the domain wall width is larger than the thickness of the cell boundary phase. For a thickness of 10 and 20 nm we find strong domain wall pinning. When an external field of about 2500 kA/m is applied, the

t (nm)	$V_{2:17}$ (nm^3)	$V_{1:5}$ (nm^3)	ratio	z
2.5	28 738	2 358	12.187	8.13
5	28 738	4 843	5.934	7.81
10	28 738	10 202	2.817	7.31
20	28 738	22 570	1.273	6.64
40	28 738	54 643	0.526	5.93

Table 7.2: z-values for different thickness t of the cell boundary phase around cells with $D = 250$ nm.

domain wall can overcome the energy barrier and cross the cell boundary phase (Fig. 7.20). For a cell boundary phase with a thickness of more than 4 times the domain wall width, the analysis of the magnetization distribution (Fig. 7.21) reveals a new behavior: The whole cell boundary phase reverses starting from the original position of the domain wall, because the curvature of the domain wall [98] allows it to propagate through the whole cell boundary phase (Fig. 7.18). This effect is a result of the competition between Zeeman energy and domain wall energy. The system can lower its Zeeman energy by domain wall bending, because the domain with its magnetization parallel to the external field increases its volume. However, this happens at the expense of domain wall energy, because the bending increases the area of the domain wall. For very thin intercellular phases the domain wall is very flat because the reduction in Zeeman energy would be very low. For thick intercellular phases the domain wall bending gets more and more pronounced until it can reverse the whole intercellular phase. This leads to the second plateau in the demagnetization curve for $t = 40$ nm in Fig. 7.19. Only at higher fields the magnetization reversal of the cells starts with the nucleation of a reversed domain in a corner of the rhomboidal cells.

Due to pinning on the computational grid an external field of 1500 kA/m is required to move the domain wall from its initial position. This effect has to be attributed to the size of the large model with $3 \times 3 \times 3$ cells, the larger size of the cells and the lower resolution of the finite element mesh. However, it has been verified that similar pinning fields are obtained for the smaller model with a proper high resolution mesh.

(a) $t = 20$ nm   (b) $t = 30$ nm   (c) $t = 40$ nm
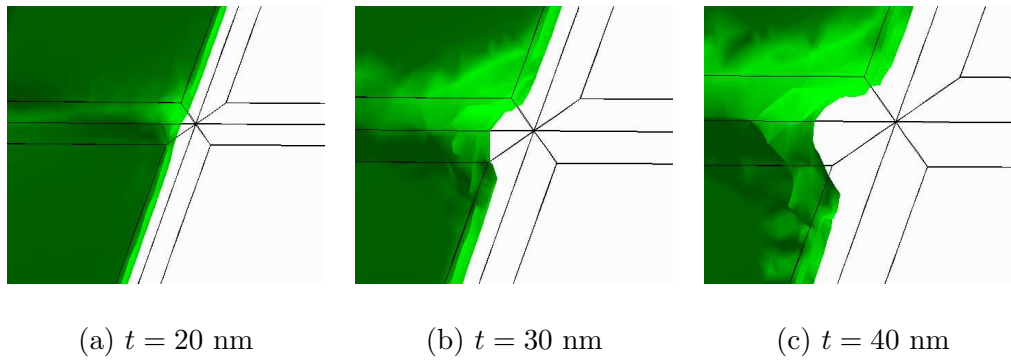
Figure 7.18: Domain wall bending of a magnetic domain wall in the (softer) intercellular phase (attractive pinning).
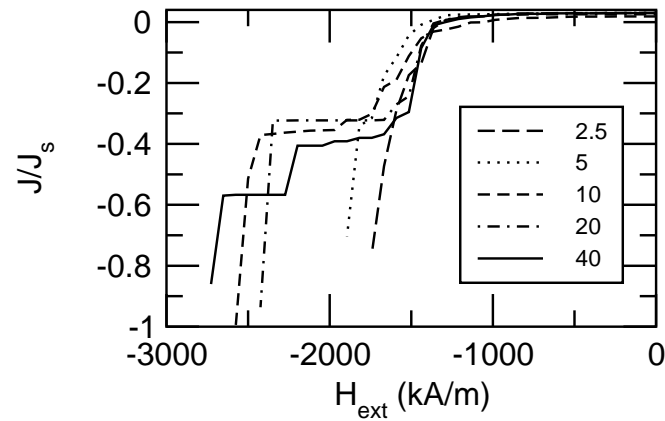
Figure 7.19: Demagnetization curves for varying thickness t (values in the legend in nm) of the intercellular phase around large cells with $D = 250$ nm.

(a) Demagnetization curve

(b) $H_{\mathrm{ext}} = -1360$ kA/m
$J/J_{\mathrm{s}} = -0.03$

(c) $H_{\mathrm{ext}} = -2040$ kA/m
$J/J_{\mathrm{s}} = -0.35$

(d) $H_{\mathrm{ext}} = -2500$ kA/m
$J/J_{\mathrm{s}} = -0.53$
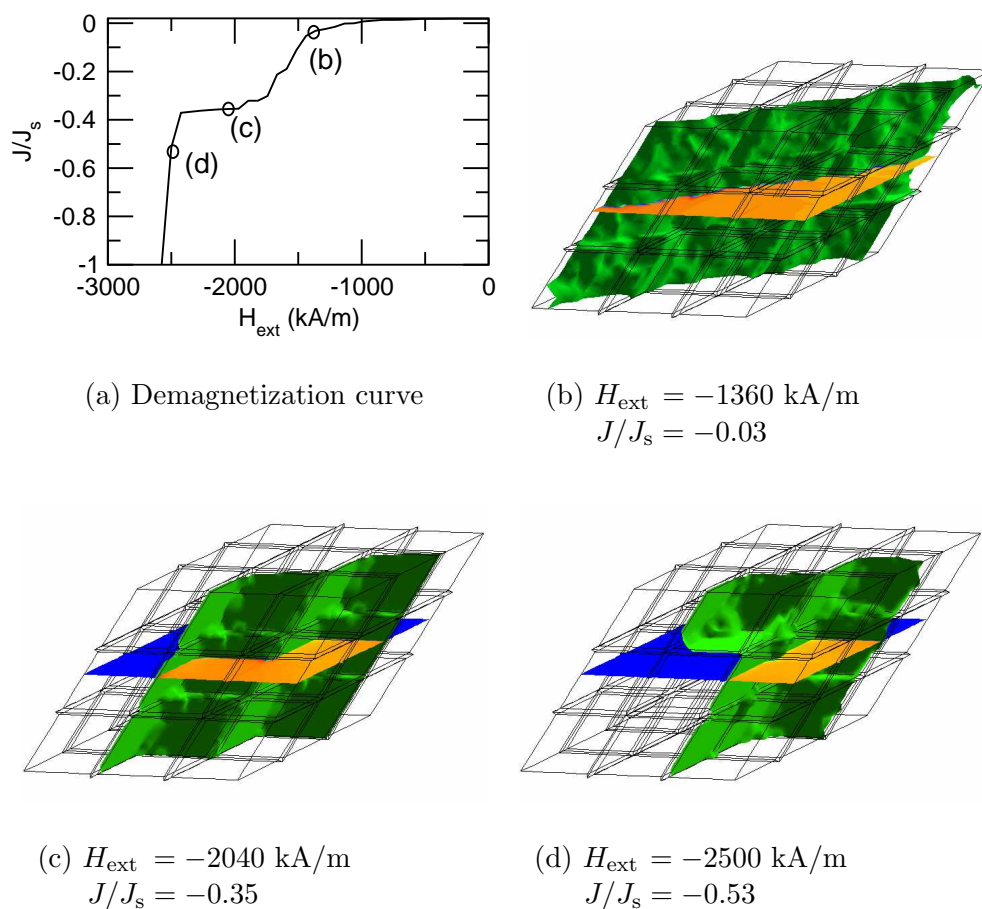
Figure 7.20: Magnetization distribution for $D = 250$ nm and $t = 10$ nm. The green surface indicates the domain wall, which separates the two domains (red and blue areas) with antiparallel magnetization.
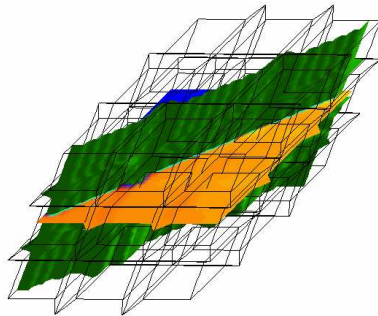
(a) $H_{\text{ext}} = -1360$ kA/m
    $J/J_{\text{s}} = -0.01$
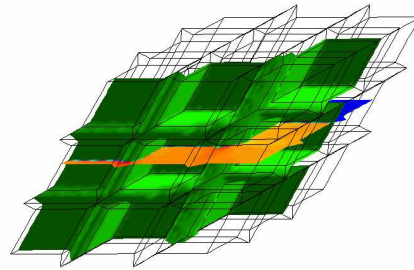
(b) $H_{\text{ext}} = -2120$ kA/m
    $J/J_{\text{s}} = -0.41$
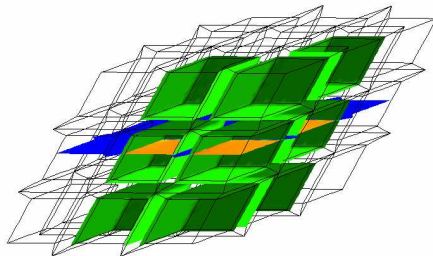
(c) $H_{\text{ext}} = -2420$ kA/m
    $J/J_{\text{s}} = -0.56$
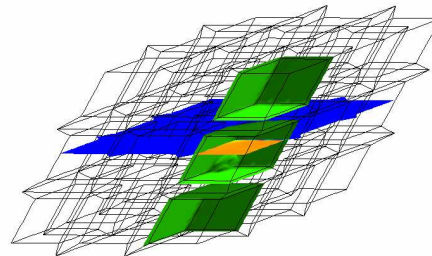
(d) $H_{\text{ext}} = -2720$ kA/m
    $J/J_{\text{s}} = -0.86$

Figure 7.21: Magnetization distribution for $D = 250$ nm and $t = 20$ nm. The green surface indicates the domain wall, which separates the two domains (red and blue areas) with antiparallel magnetization.

7.5 Conclusions

In order to improve the magnetic properties of pinning controlled $Sm(Co,Fe,Cu,Zr)_z$ magnets the thickness and the composition of the cell boundary phase have to be optimized. As the difference in the domain wall energy between the cells and the cell boundary phase increases, the pinning field and, as a result, the coercive field of the magnet increase in the regime of attractive as well as in that of repulsive pinning. Our detailed study of the pinning behavior of domain walls has revealed, that the dependence of the pinning field on the thickness of the intercellular phase is equivalent for attractive and repulsive domain wall pinning. However, our simulations show, that the cellular structure of $Sm(Co,Fe,Cu,Zr)_z$ magnets plays a crucial role for domain wall pinning. The cell boundary phase must not be too thin, for the domain wall to "fit in" and it must not be thicker than 4 times the domain wall width. Within this range the thickness of the cell boundary phase reduces the pinning field linearly with increasing relative thickness of the intercellular phase.

Chapter 8

Nucleation Processes in FePt Nanoparticles

Finite element micromagnetic simulations have been carried out to study the influence of the demagnetizing field, the distribution of easy axes and the particle size on the coercivity of FePt nanoparticles.

8.1   Introduction

High density magnetic storage media require tight control of the grain size, grain size distribution, chemical composition, and microstructure to ensure the thermal stability of the bits and keep the media noise low. However, as the areal density increases, the grain size and the magnetic switching volume decreases. In order to maintain the stability materials with higher uniaxial anisotropy than the common CoCrPt alloys are required. FePt thin films and self assembled nanoparticles (cf. Fig. 8.1) are promising candidates for high density magnetic storage media. Their magnetocrystalline anisotropy is 50–100 times larger than in CoPtCr media alloys which may allow areal densities in the Tbit/in^2 regime [99].
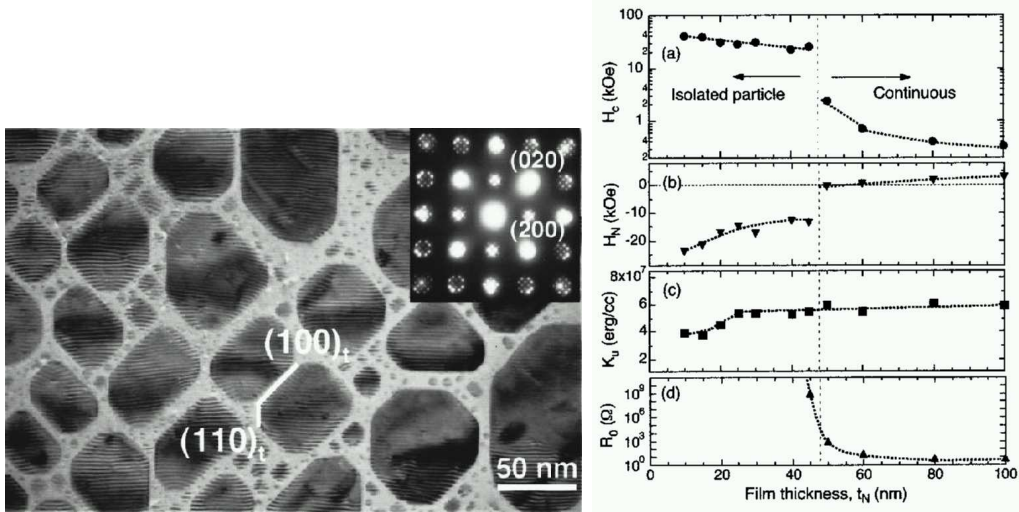
Figure 8.1: Left: Transmission electron micrograph of an FePt thin film (thickness: 10 nm) on MgO(001) substrate.
Right: Magnetic properties and electric resistance for FePt thin films as a function of film thickness. H_c denotes the coercivity, H_n the nucleation field, K_u the uniaxial magnetocrystalline anisotropy constant, and R_0 the resistance. (both images from [100])

8.2 Finite Element Model

A HREM image and our geometrical model are shown in Fig. 8.2. We have split our hexahedral particle into six parts of equal volume. In each part the magnetocrystalline anisotropy axis is uniform, but we have varied the axes in the different parts.

Typical values for the material parameters of FePt ($L1_0$) thin films and nanoparticles have been measured and published in various papers. They are summarized in the papers by Klemmer [102] and Weller [99]. We have chosen the values given in Tab. 8.1 for our FE simulations. Additional influences from surface anisotropy, thermal effects, or disorder in the crystalline structure (dislocations, twins) have been neglected.
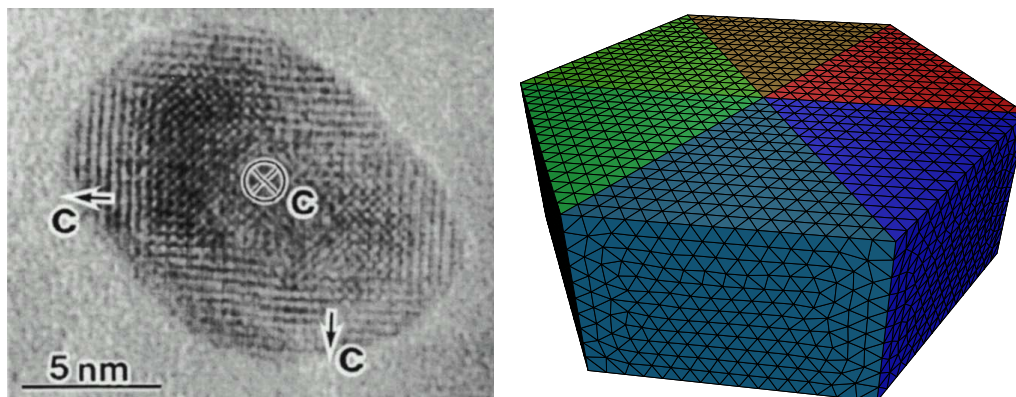
Figure 8.2: Left: HREM image of a typical ordered FePt nanoparticle with three regions of different easy axes (picture from [101]).
Right: Geometrical model of an FePt nanoparticle used in the micromagnetic simulations. The finite element mesh consists of 10340 nodes and 55076 elements, which gives a discretization length of 1.2 nm, if the edge length is 30 nm. The model is split into six parts of equal volume, in which the anisotropy axis are varied (2:2:2 configuration shown).

FePt ($L1_0$)	
J_s	1.43 T
A_{exch}	1.0×10^{-11} J/m
K_{ani}	7.7 MJ/m^3
H_{ani}	10769 kA/m ($\hat{=}$13.5 T)
l_{exch}	1.2 nm

Table 8.1: Material parameters of FePt ($L1_0$), which have been used for the micromagnetic simulations [102, 99].
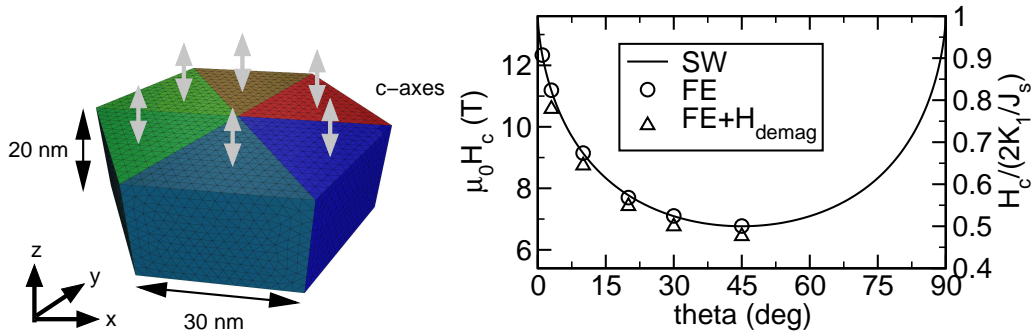
Figure 8.3: Nucleation field of an FePt nanoparticle with uniaxial magnetocrystalline anisotropy as a function of the angle of the applied field with respect to the easy axis. The finite element simulation gives the correct result of a Stoner-Wohlfarth particle. If the demagnetizing field is taken into account, the nucleation field is reduced by less than 5 % due to the dominating high magnetocrystalline anisotropy.

8.3   Stoner-Wohlfarth Behavior

First we have done simulations of a particle with a single magnetocrystalline anisotropy axis and a diameter of 60 nm. As expected we find the behavior of a typical Stoner-Wohlfarth particle. The results are shown in Fig. 8.3. Then we have included the demagnetizing field in the simulation and found only a very small influence on the nucleation field, which is reduced by less than 5 %. This is due to the dominating role of the anisotropy, which gives rise to an anisotropy field of more than 13 T. In comparison the demagnetizing field in a particle with perfectly homogeneous magnetization varies from 0.4 to 0.9 T within the particle. This is illustrated in Figs. 8.4, 8.5, and 8.6, where we have plotted the z-component of the demagnetizing field through different parts of the particle.

8.4   Multiple Easy Axes

Then we have studied the influence of a distribution of easy axes within the particle. As described above, we have varied the easy axis in the six parts of our model and calculated the coercivity. The results are summarized in Tab. 8.2. The left column indicates, how many of the six parts of our
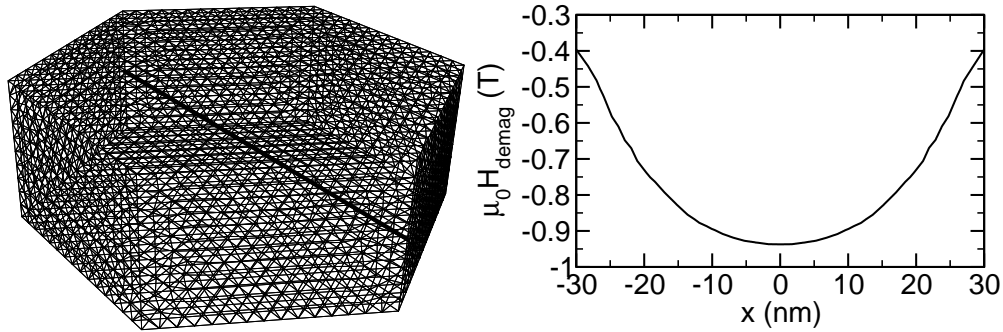
Figure 8.4: The z-component of the demagnetizing field has been measured along the x-axis through the center of the nanoparticle as shown in the left image. The result is shown in the graph on the right.
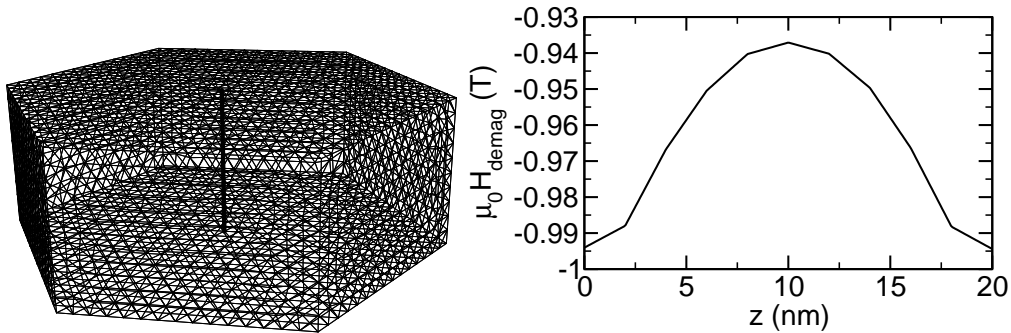
Figure 8.5: The z-component of the demagnetizing field has been measured along the z-axis through the center of the nanoparticle as shown in the left image. The result is shown in the graph on the right.
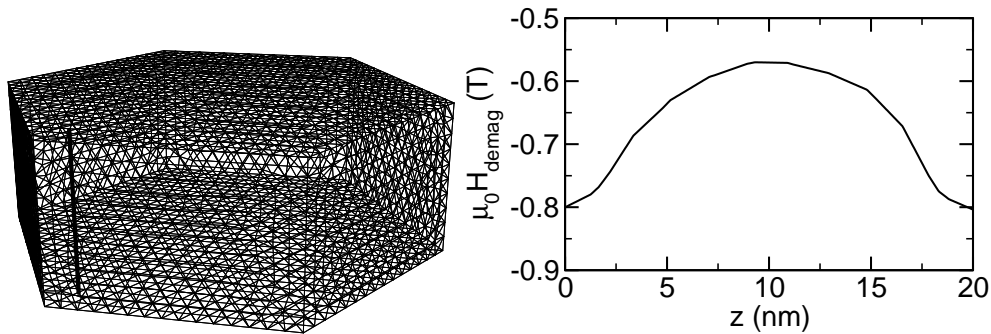
Figure 8.6: The z-component of the demagnetizing field has been measured along a line parallel to the z-axis close to an edge of the nanoparticle as shown in the left image. The result is shown in the graph on the right.

$\uparrow:\rightarrow:\nearrow$	H_c (kA/m)
5:1:0	3330
4:2:0	3140
4:1:1	3310
3:3:0	3630
3:2:1	3420
2:2:2	3430

Table 8.2: Coercivity as a function of the easy axis distribution: The first, second, and third number of a triplet in the first column indicates in how many of the six parts of the finite element model the easy axes are parallel to the z-, x-, and y-axis, respectively. Obviously, the coercivity is strongly reduced as compared to the nucleation field of a particle with a single anisotropy axis. However, the mixture of anisotropy axes does not have a significant influence for a particle with 30 nm edge length.

model have their easy axis parallel to the z-, y-, and x-axes, respectively. The results show, that the coercivity is decreased by a factor of three as compared to the nucleation field. However, the different distributions of easy axes show no significant influence on the coercivity. This behavior indicates, that the 90° domain wall at the interface between two misaligned parts of the particle determines the coercivity. Thus, already a single misaligned part is sufficient to reduce the coercivity by a factor of three.

Finally, we have reduced the size of the particles and studied their coercivity. The shape and aspect ratio remained the same, the model has just been rescaled to the desired size. The exchange length of FePt is about 1 nm (cf. Tab. 8.1) and the resulting domain wall width about 3 nm. As a result, the properties of very small particles are modified due to the increasing importance of the exchange interactions. The results of our simulations are summarized in Tab. 8.2. The coercivity of (2:2:2) particles with the "3 easy axes"-distribution (top left figure in Fig. 8.7) remains almost constant if we reduce the edge length of the particles from 30 nm (discussed above) to 15 nm and 7.5 nm. However, for an edge length of 3.75 nm (diameter of the particle: 7 nm) the coercivity is reduced to 2100 kA/m.

The "6 easy axes"-distribution is characterized by the fact, that each pair of neighboring parts in our model has perpendicular easy axes. For this distribution we find a further reduced coercivity of 2000 kA/m, which drops
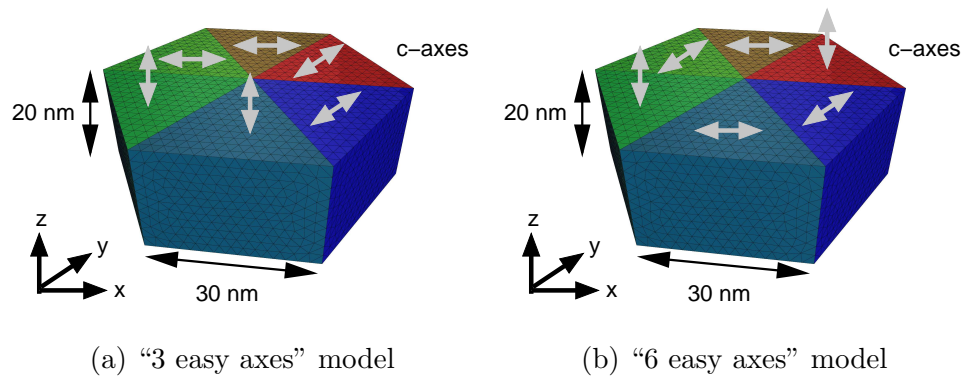
(a) "3 easy axes" model   (b) "6 easy axes" model
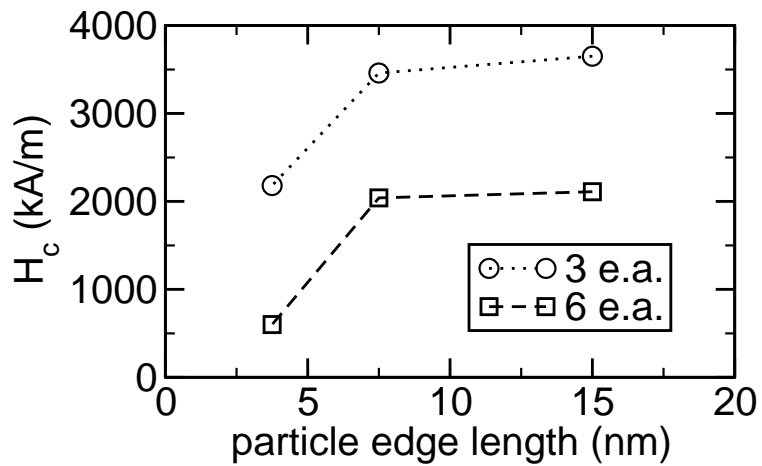
Figure 8.7: Coercivity as a function of the easy axis distribution and edge length of the nanoparticle. The easy axis distribution is shown in the top left figure for the "3 easy axes" (where two neighboring parts of the model have the same easy axis) and on the top right for the "6 easy axes" (where all neighboring pairs have perpendicular easy axes) distribution, respectively.

to 600 kA/m if the particle size is reduced to 3.75 nm.

8.5 Conclusions

Shima et al. [100] have measured coercivities of up to 40 kOe (3200 kA/m) for FePt thin films with strongly faceted islands (cf. Fig. 8.1), which agree well with our simulations. In very small FePt nanoparticles of approximately 20 nm diameter Bian et al. [101] have found regions with different easy axes (as shown in Fig. 8.2) and measured coercivities of 4.4 kA/m. Our simulations have shown a similar reduction in coercivity depending on the particle size and distribution of easy axes. However, close cooperation with experimental groups will be necessary to model the microstructure of the thin films and nanoparticles properly and use appropriate material parameters.

Chapter 9

Permalloy Nanodots

The static and dynamic properties of magnetic nanodots with curling in-plane magnetization distribution (vortex) are studied using 3D dynamic micromagnetic simulations. The magnetization distribution, contributions to the total energy, hysteresis behavior, and surface charges are calculated and compared with an analytical vortex model. A phase diagram of the magnetic ground states of magnetic nanodots as a function of the radius and height is calculated and compared with analytical and experimental investigations. The dynamic properties, which are important for high frequency applications, are reported for in-plane and out-of-plane fields.

9.1 Introduction

The recent advances in microfabrication techniques [103] have stimulated interest in the properties of submicron sized patterned magnetic elements [104, 105]. Promising applications include magnetic random access memory, high-density magnetic recording media, and magnetic sensors [106]. However, in order to exploit the special behavior of magnetic nanoelements it is necessary to study and understand their fundamental properties. We have studied the static properties of cylindrical magnetic nanodots of different sizes and aspect ratios with analytical models and numerical finite element (FE) simulations, especially magnetic vortex states.

Direct experimental evidence for the existence of these magnetic vortex
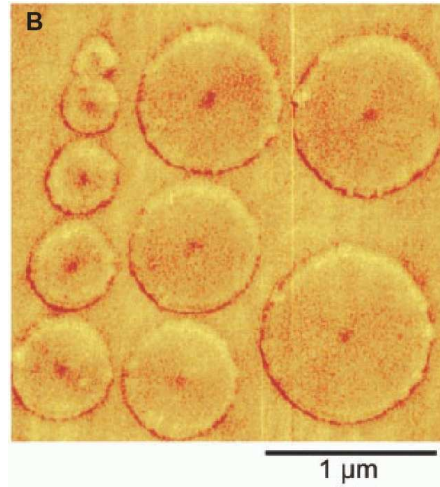
Figure 9.1: MFM image of nanodots with 50 nm thickness and different diameters (0.3 to 1 μm) [107]. The dark spots in the center of the dots indicate the magnetic vortex core, where the MFM detects the stray field caused by the perpendicular magnetization.

states has been found by the method of magnetic force microscopy. Shinjo and coworkers [107] have used magnetic force microscopy (MFM) to characterize magnetic nanodots of permalloy ($Ni_{80}Fe_{20}$) with a thickness of 50 nm and a radius between 300 nm and 1 μm, for example. An MFM image is given in Fig. 9.1. It shows the magnetic contrast of nanodots with different radii. The dark spots in the center of the nanodots indicate the position of the vortex core, where the strongest stray field is sensed by the MFM tip. However, the lateral resolution is not high enough to estimate the diameter of the vortex core. In addition, the the MFM tip is sensitive only to the out-of-plane component of the stray field gradient, and the interaction between the magnetization of the nanodot and the MFM tip plays an important role for the contrast. These problems can be overcome using spin-polarized scanning tunneling microscopy and the direct observation of the magnetization distribution in nanoscale iron islands with magnetic vortex cores have been reported [108]. Lorentz transmission electron microscopy allows in situ magnetizing experiments with thin samples and it has been used to characterize the magnetization distribution in individual circular and elliptical particles [109].

The hysteresis loops of magnetic nanodots have been measured by vibrating sample magnetometer [105] and magneto-optical methods [110, 111]. Single domain and vortex states have been successfully identified. Furthermore, these magnetic vortex states are an interesting object for high frequency magnetization dynamics [112] experiments, which are important for high-density magnetic recording media, where high-frequency field pulses of the magnetic write head store the information by reversing the magnetization.

In most of the simulations the material parameters given in Tab. 9.1, which are typical of permalloy ($Ni_{80}Fe_{20}$), have been used.

Saturation magnetization	M_s	8×10^5 A/m $= 8 \times 10^2$ G
Saturation polarization	$J_s = \mu_0 M_s$	≈ 1 T
Exchange constant	A	13×10^{-12} J/m $=$
		1.3×10^6 erg/cm
Exchange stiffness constant	$C = 2A$	26×10^{-12} J/m
Anisotropy has been neglected.		

Table 9.1: Typical material parameters of permalloy ($Ni_{80}Fe_{20}$).

9.2 Analytical and Numerical Models

9.2.1 The Analytical Rigid Vortex Model

The rigid vortex model assumes a "rigid vortex", which does not change its shape in an external field. Together with a certain magnetization distribution it gives an approximation for the magnetization distribution of a curling state (vortex state) in a fine cylindrical particle. An analytical model for the magnetization distribution $\boldsymbol{M}(\boldsymbol{x})$ in zero field has been developed using a variational principle by Usov and coworkers [113, 114]. It is split into two parts (cf. Fig. 9.2)

The first part describes the magnetization in the core of the vortex ($r \leq a$, a is the vortex core radius), which is defined by $M_z \neq 0$:

$$M_x = -\frac{2ar}{a^2+r^2} \sin \varphi \tag{9.1}$$

$$M_y = \frac{2ar}{a^2+r^2} \cos \varphi \tag{9.2}$$
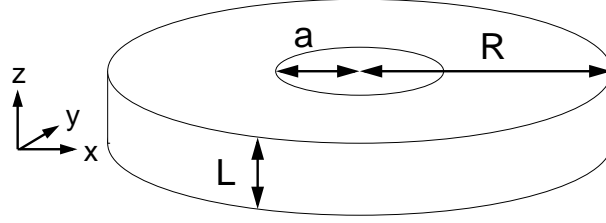
Figure 9.2: Geometry of a flat cylindrical nanodot.

$$
\begin{aligned}
M_z &= \sqrt{1 - \left(M_x^2 + M_y^2\right)} \\
&= \sqrt{1 - \frac{2ar}{a^2 + r^2}}
\end{aligned}
\tag{9.3}
$$

where r, φ are the polar coordinates. The other part describes the magnetization outside the core $(r > a)$:

$$
\begin{aligned}
M_x &= -\sin\varphi & (9.4) \\
M_y &= -\cos\varphi & (9.5) \\
M_z &= 0 & (9.6)
\end{aligned}
$$

a denotes the radius of the core and it is given by

$$
a = \left(\frac{l_{\text{ex}}^2 R}{12\kappa g}\right)^{1/3} \quad ,
$$

where l_{ex} (the exchange length) is given by

$$
l_{\text{ex}} = \sqrt{\frac{A}{\frac{1}{2}\mu_0 M_{\text{s}}^2}} \quad ,
$$

R is the radius of the nanodot, κ is a numerical constant (cf. [113]) and g is the ratio R/L, where L is the height of the nanodot. For permalloy we find $l_{\text{ex}} = 5.7$ nm and with $R = 100$ nm and $L = 20$ nm we get $a \approx 11$ nm. The core radius is obtained from the minimization of the total energy (exchange and magnetostatic energy).

There are some typical properties of the rigid vortex model with Usov's magnetization distribution:

	coarse mesh	fine mesh	adapted mesh
$R = 1$, $L = 0.2$			
mesh size	0.2	0.06	0.02 to 0.4
nodes	1437	6455	1397
elements	5816	30979	6256
surface triangles	1758	5232	1390
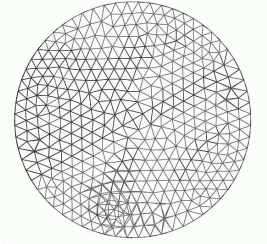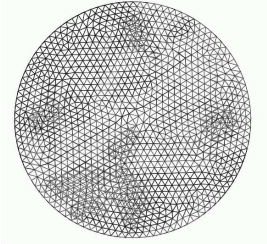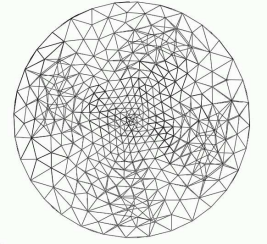
Table 9.2: Finite element meshes of different mesh density for a circular nanodot.

- In equilibrium in zero field there are surface charges only on the top and bottom surface within the vortex core.

- For shifted vortices surface charges are induced on the circumference of the nanodot.

- There are no volume charges in the model.

9.2.2   Numerical Finite Element Simulations

A model of a cylindrical nanodot and the finite element meshes were created using the CAD software MSC/Patran. It is a very flat nanodot with a radius of $R = 1$ and a height of $L = 0.2$. In order to investigate the influence of the finite element mesh on the results, three meshes with different mesh density have been created (cf. Tab. 9.2).

The first mesh is a uniform tetrahedral mesh with an average mesh size of 0.2. Since the nanodot is 0.2 thick, there is only one layer of elements. The second dot has an average mesh size of 0.06, which resulted in 4 layers. The third mesh is an "adapted" mesh, with a very high density of nodes in the center, where the core of the vortex is found in zero external field. This
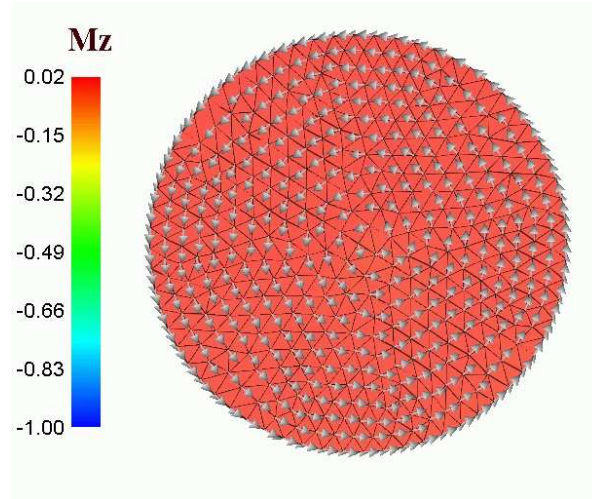
Figure 9.3: Magnetization distribution of the vortex state on the coarse mesh. The vortex core cannot be resolved.

is sensible, because the vortex represents a singularity, which requires a very high numerical accuracy and therefore a lot of nodes. The outer regions are meshed with larger finite elements, since the magnetization distribution is rather uniform.

9.3   Static Properties

First we have investigated the static properties of the permalloy nanodots and compared the results of the analytical rigid vortex model and the numerical finite element simulations.

The finite element simulations have been initialized with the magnetization distribution of the rigid vortex model and an approximate core radius. Then the Landau-Lifshitz equation of motion for the magnetization has been integrated with a damping constant $\alpha = 1$ in zero field, and the magnetization relaxed to its equilibrium distribution, which minimizes the total Gibbs free energy.

For the coarse mesh the magnetization distribution given in Fig. 9.3 has been found. Obviously, the resolution of the mesh is too low to properly resolve the vortex. Thus, M_z is zero in the whole dot. The second mesh
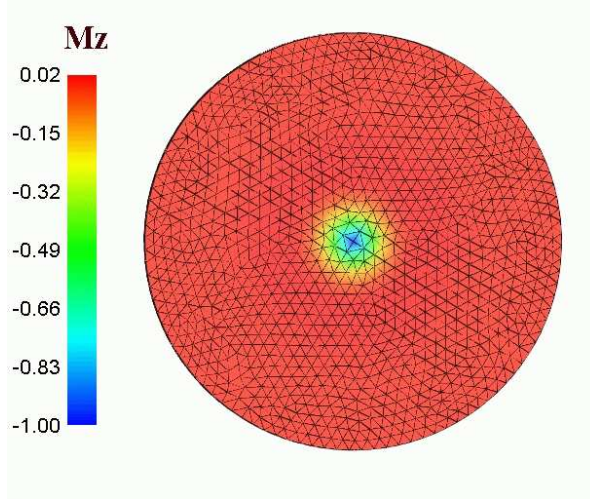
Figure 9.4: Magnetization distribution of the vortex state on the fine mesh. The vortex core is properly resolved.

with a mesh size of 0.06 is fine enough to resolve the core (Fig. 9.4). The adapted mesh, which has a high resolution with many small elements in its center and a gradually decreasing resolution towards the circumference, resolves the core just as well as the fine mesh (cf. Fig. 9.5), but its number of nodes and elements is comparable to that of the coarse mesh. Therefore it is very well suited for simulations, where the vortex core can be expected to be in the center of the nanodot. If the vortex core moves out of the center (e.g. due to an external field), it might reach a region with a low resolution mesh. Then, the vortex core cannot be resolved properly any more and the results become very unreliable. As a result, it is necessary to use either a uniform high resolution mesh or to apply adaptive mesh refinement, which increases the mesh density at run time as required and optimizes (minimizes) the number of nodes and elements in the finite element mesh.

The profile of M_z along the x-axis through the center of the dot for the different meshes is given in Fig. 9.6. The coarse grid clearly fails to resolve the vortex. However, the fine and the adapted grid are in excellent agreement. This emphasizes the importance of suitable meshing, because the fine grid consists of more than four times more elements than the adapted one, which leads to much longer computation times. However, if we define the vortex core radius as that radius, where M_z is zero, we find a value of
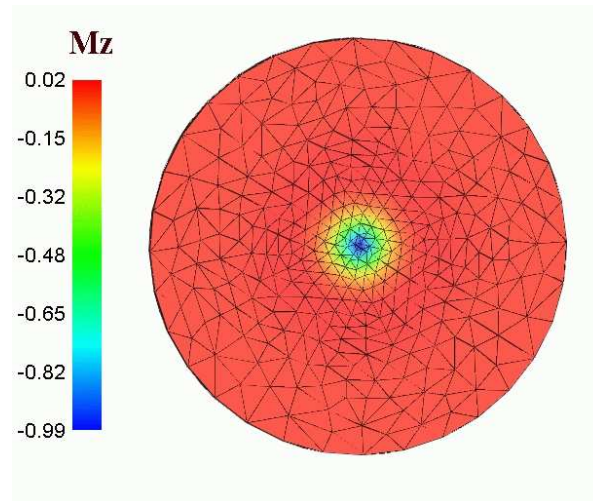
Figure 9.5: Magnetization distribution of the vortex state on the adapted mesh. The vortex core is nicely resolved, but the total number of elements and vertices is similar to that of the coarse mesh.
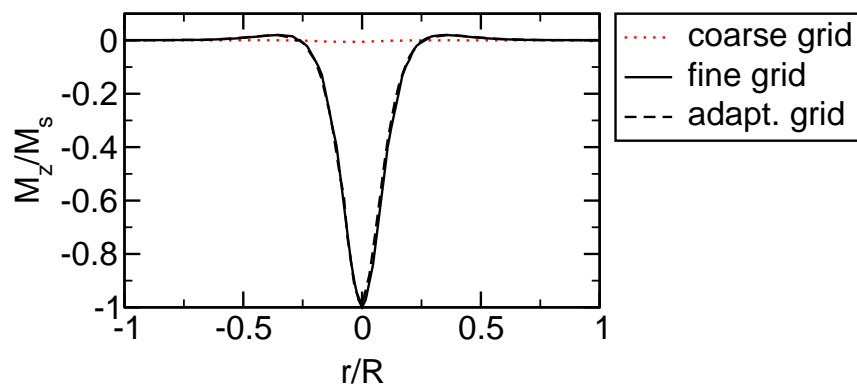
Figure 9.6: Profile of M_z along the x-axis through the center of the nanodot for different meshes.
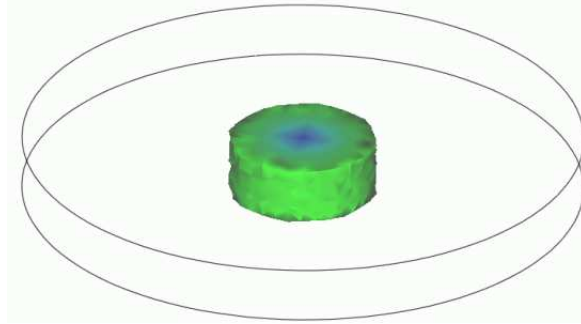
Figure 9.7: Isovolume ($M_z < 0$) plot of the vortex core.

approximately 25 nm, which is considerably larger than the value predicted by the rigid vortex model (11 nm, see above). M_z is also quite uniform across the thickness of the dot. This fact and the "shape" of the vortex core are visualized in Fig. 9.7. The core is plotted as the isovolume, where M_z is 0 or lower (the vortex is pointing in $-z$ direction). This corresponds to the definition of the rigid vortex model. The dot itself is sketched by the edges of its top and bottom surface.

9.3.1   Magnetization Distribution

In order to speed up the calculation of equilibrium magnetization distributions of magnetic vortices the rigid vortex model has been implemented in the FE code and it has been used to initialize the magnetization distribution with the vortex at the beginning of the simulation. The plots of M_z in Fig. 9.8 show a comparison of the rigid vortex model with the finite element approximation (due to the finite resolution of the mesh, there is a small difference in the core diameter) and the equilibrium magnetization distribution, which has been found by integrating the Landau-Lifshitz equation of motion with the damping constant $\alpha = 1$ until equilibrium has been reached.

The results show, that the vortex core is approximately 54 % larger (18.5 nm) than assumed by the rigid vortex model (12 nm) due to a "broadening" of the M_z distribution (if the core radius is defined by $M_z = 0$). Furthermore it is interesting to note that the finite element simulation shows that there is a region with $M_z > 0$ outside the core. Thus, we find positive
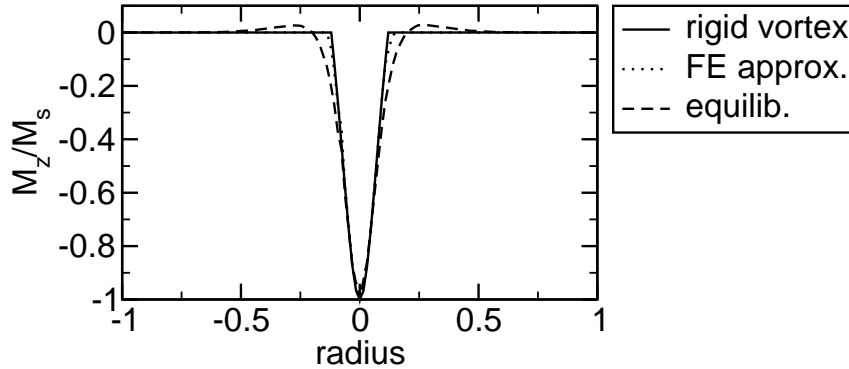
Figure 9.8: Profiles of M_z along the x-axis through the center of the nanodot for the analytical model, its finite element approximation, and the relaxed magnetization in equilibrium.

surface charges in the core of the vortex, which are surrounded by negative surface charges. Only outside of approximately half the radius (50 nm) almost all surface charges disappear. It has been verified, that there is very little variation of the magnetization distribution across the thickness of the nanodot.

9.3.2 Energy

Then the exchange and magnetostatic energies of the vortices have been compared. The analytical values for the energies have been obtained with the formulas given by Usov et al. [113, 114]. The finite element results are in good agreement with the analytical results and it is shown in Tab. 9.3, that the energy of the equilibrium magnetization distribution, which has been found with the FE model, is indeed smaller than that of the rigid vortex model.

In the first row of Tab. 9.3 the analytical results for the rigid vortex model are given, which have been obtained using Ref. [114]. The second row gives the result, which is obtained by the FE program, if the magnetization distribution is initialized with the rigid vortex model. The third row shows how the results improve, if a finite element mesh with smaller mesh size is used (cf. Fig. 9.5), and the fourth row gives the deviation from the analytical solution. In the fifth row the magnetostatic energy, which is almost solely

	units: J/m^3	Magnetostatic energy	Exchange energy	Total energy
1	Rigid vortex model (analytical Usov)	432.1	5356	5788
2	Rigid vortex model (FE)	388.8	5307	5696
3	Rigid vortex model (FE) adapted mesh	417.0	5341	5758
4	FE error	-3.5 %	-0.28 %	-0.52 %
5	Rigid vortex model (FE) zoom	418.1		
6	FE simulation (equilib.)	387.1	5150	5537
7	difference FE - analytical	-10.42 %	-3.85 %	-4.35 %

Table 9.3: Comparison of the energies obtained by the rigid vortex model and numerical FE simulations.

caused by the vortex core, is given for a FE model, where the core has been meshed with a very fine mesh and the rest of the nanodot has been omitted. Finally, the sixth row gives the results after relaxing the magnetization into equilibrium, and the seventh row indicates the deviation from the analytical result. Thus, the rigid vortex model is a good approximation, but the FE calculation shows, that there is a slightly different magnetization distribution, which has a lower total energy.

9.3.3 Hysteresis

Fig. 9.9 shows the hysteresis curve for a circular nanomagnet with in-plane external field. For very high external fields (applied in the plane of the nanodot), the magnetization is almost uniform and parallel to the external field (Fig. 9.10(a)). As the field decreases (solid line in Fig. 9.9) the magnetization distribution becomes more and more non uniform, which is caused by the magnetostatic stray field. Upon further decrease of the external field, the symmetry of the magnetization distribution breaks and a "C" state (Fig. 9.10(b)) develops. At the nucleation field (about 5 kA/m for our example) a vortex nucleates on the circumference and quickly moves towards its equilibrium position (close to the center of the nanodot). As a result we find a sudden drop in the average magnetization. When the exter-
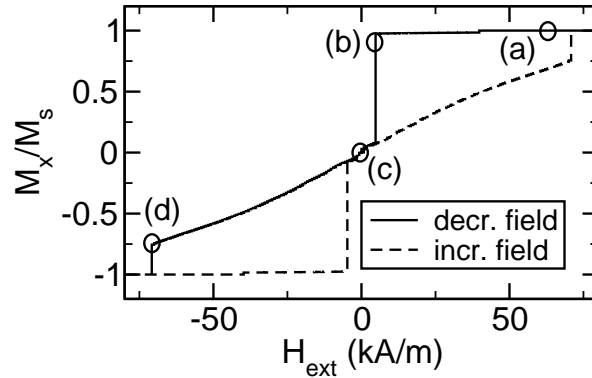
Figure 9.9: Hysteresis curve of a nanodot with $L/R = 20$ nm$/100$ nm $= 0.2$ for an in-plane external field. The circles mark the position on the hysteresis curve at which the snapshots in Fig. 9.10 have been taken.

nal field is reduced to zero the vortex moves into the center of the nanodot (Fig. 9.10(c)). If the external field is increased in the opposite direction, the vortex is forced out of the center of the dot. For about -70 kA/m the vortex is pushed out of the nanodot (annihilation: Fig. 9.10(d)) and we find the second jump in the hysteresis curve to (almost) saturation.

This characteristic behavior has also been found experimentally using Hall-micromagnetometry by Hengstmann et al. [115], who measured the stray field of individual permalloy disks using a sub-μm Hall magnetometer. The hysteresis loops of arrays of Supermalloy nanomagnets have been measured by Cowburn et al. [110] using the Kerr effect. Their characteristic loop shape has then been used to identify the single-domain in-plane and the vortex phase.

The rigid vortex model can describe very well the susceptibility, magnetization distribution, and vortex annihilation field for low fields as well as the vortex nucleation field for a wide range of dot sizes [116, 117, 118, 119]. The experimentally observed nucleation fields appear to be bigger than those predicted by the rigid vortex model [120]. This is probably due to the fact, that the simplest "C-shape" nucleation is not always an appropriate approach to describe the magnetization reversal in circular dots.

In Fig. 9.11 the total energy is plotted as a function of the external field for the branch of decreasing field of the hysteresis curve. The solid line

(a) (Almost) homogeneous magnetization.

(b) "C" state before the vortex nucleates.

(c) Centered vortex in zero field.

(d) Magnetization distribution before annihilation of the vortex.
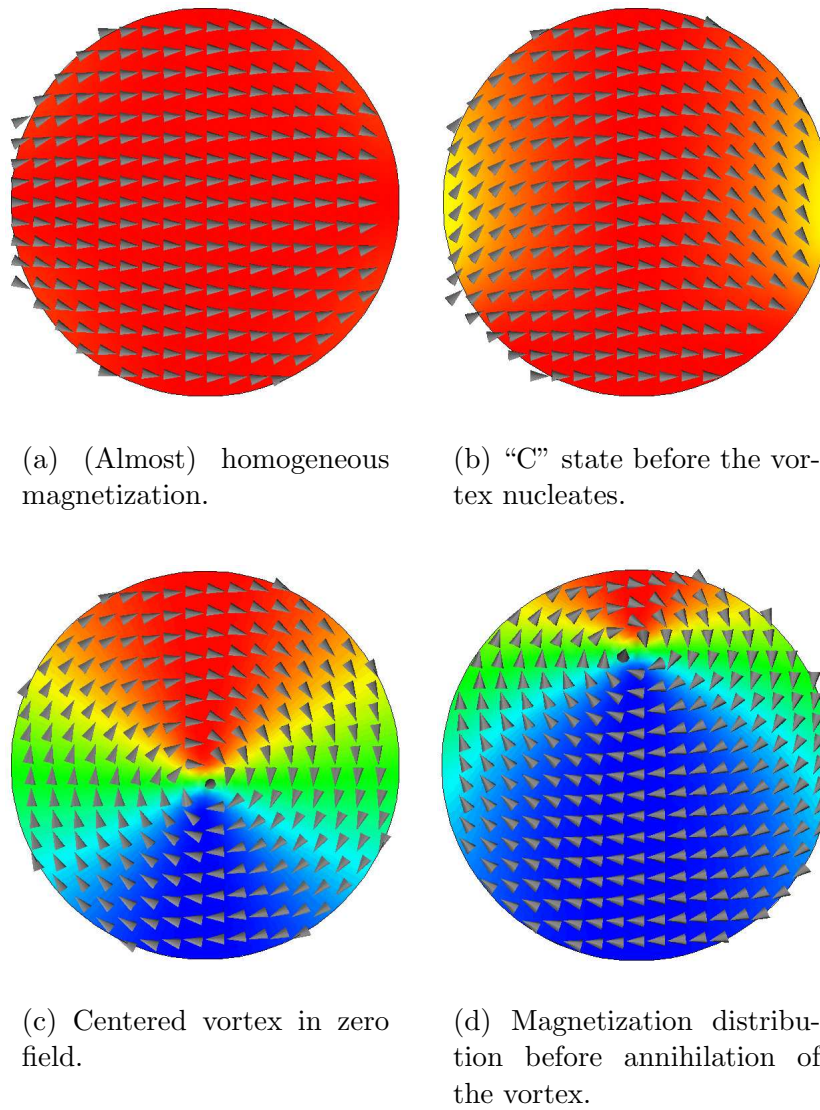
Figure 9.10: Typical magnetization distributions along the hysteresis loop. The snapshots have been taken at the corresponding position on the hysteresis curve indicated in Fig. 9.9.
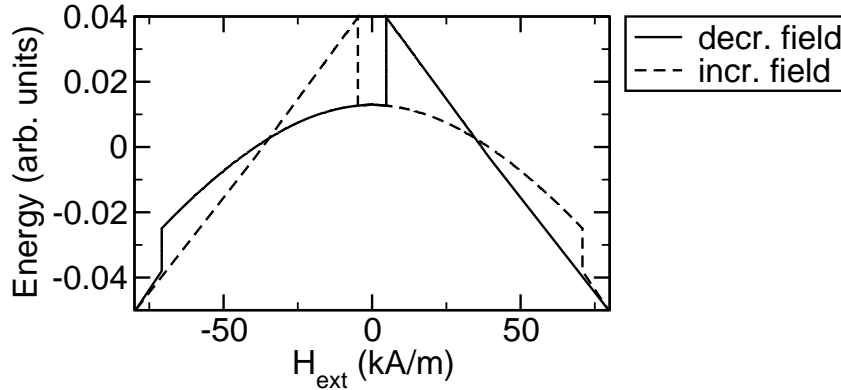
Figure 9.11: Total energy as a function of the external field for both branches (solid line for decreasing field - dashed line for increasing field) of the hysteresis loop.

indicates the hysteresis branch for decreasing external field and the dashed line that for increasing field. For very high fields we have an almost uniformly magnetized nanodot. For decreasing field the total energy increases (almost) linearly. The dashed line for positive field values indicates the total energy for the vortex state. At the intersection of the solid and the dashed line (at a value of about 35 kA/m for the external field) the vortex state and the uniform magnetization have equal energy. However, they are separated by an energy barrier, which arises from the magnetostatic energy, which in turn is caused by the stray field on the circumference of the nanodot as the vortex is pushed out of the center. Thus, the vortex state is a metastable state for external fields higher than 35 kA/m and the uniform state is metastable for external fields below 35 kA/m.

The field dependence of exchange and magnetostatic energy are given in Fig. 9.12. The exchange energy remains approximately constant for negative external fields until the annihilation field is reached. Since all exchange energy is stored in the vortex core, this indicates that the vortex core remains undisturbed for even very large vortex shifts.

For a twice as large nanodot with $R = 200$ nm and $L = 40$ nm we find a nucleation field of 28 kA/m and an annihilation field of 84 kA/m. The corresponding hysteresis loop is given in Fig. 9.13.

In general, the initial susceptibility, the vortex nucleation, and the
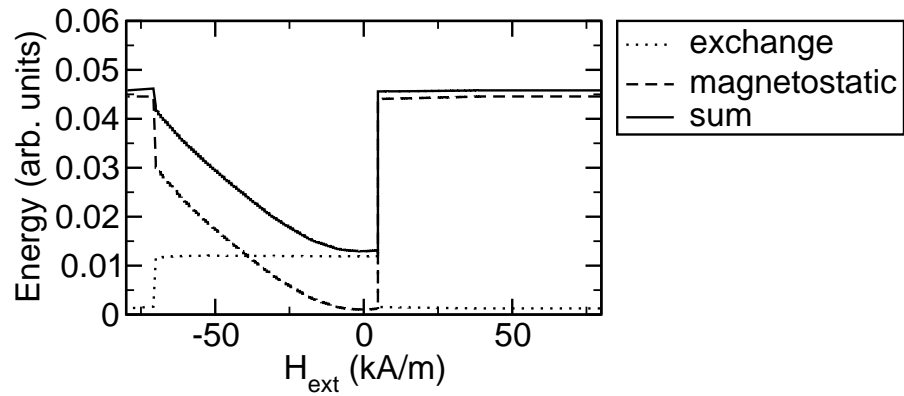
Figure 9.12: Exchange and magnetostatic energy and their sum as a function of the external field (for decreasing external field).
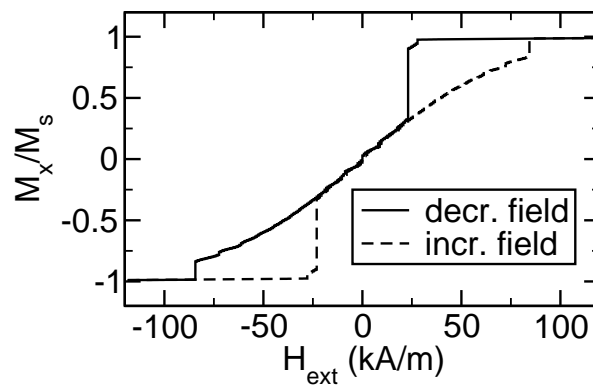
Figure 9.13: Hysteresis curve of a nanodot with a radius of 200 nm and a thickness of 40 nm.
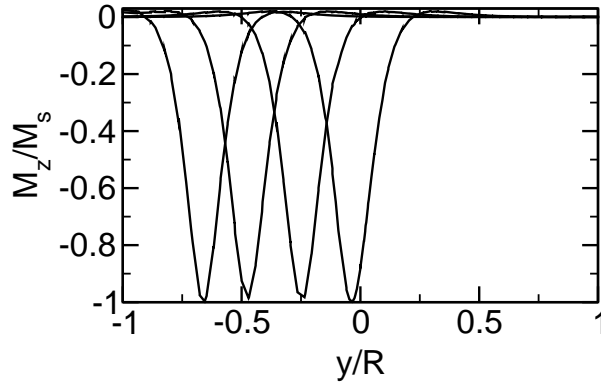
Figure 9.14: Profiles of M_z along the y-axis through the center of the nanodot for a vortex moving in $-y$ direction due to an external field increasing in x direction.

annihilation fields depend on the dot's saturation magnetization M_s and should scale universally as a function of the dimensionless dot-aspect ratio L/R [116, 117].

9.3.4   Average Magnetization

Fig. 9.14 shows profiles of M_z along the y-axis for different external fields. As a result, the vortex is shifted and the profile "moves" towards the circumference of the dot ($|y/R| = 1$). From this plot the position of the vortex core for a given external field has been extracted. The corresponding average magnetization $\langle M_x \rangle$ is plotted in Fig. 9.15 (open circles). For symmetry reasons M_y is zero (the vortex is shifted along the y-axis, since we applied a field in x-direction).

By integrating the magnetization distribution of the rigid vortex model over the surface of the nanodot the average magnetization $\langle M_x \rangle$ has been calculated. The result is given in Fig. 9.15. We find very good agreement between the rigid vortex model and the finite element simulation. The small difference can be understood by considering small deviations of the magnetization distribution due to surface charges on the circumference (cf. Sec. 9.3.5).
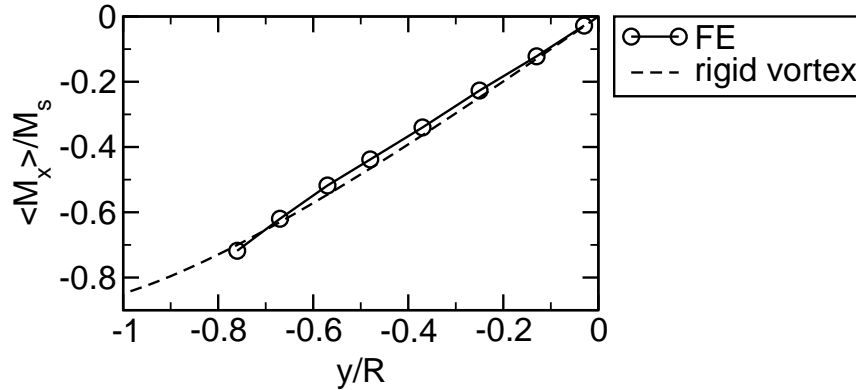
Figure 9.15: Comparison of $\langle M_x \rangle$ as a function of the vortex displacement between the FE simulation and the rigid vortex model. $y = 0$ corresponds to a centered vortex, $y = -0.78$ is the maximum shift before vortex annihilation occurs in the FE simulation.

9.3.5   Surface Charge Density

Another important aspect in comparison with the rigid vortex model is the magnetostatic energy and the surface charges, which generate the magnetostatic field. On the top and bottom circular surface the surface charges are proportional to M_z, because the normal vector $\boldsymbol{n}$ of the top and bottom is simply e_z and $-e_z$, respectively. However, on the circumference the normal vector is, of course, e_r.

Fig. 9.16 shows a contour plot of the surface charge density on the nanodot in zero field. As expected, the equilibrium position of the vortex core is in the center of the nanodot and the circular magnetization distribution avoids any surface charges on the circumference (Fig. 9.17).

If an in-plane external field is applied, the vortex core is shifted perpendicular to the direction of the field (Fig. 9.18). As a result, surface charges appear on the circumference (Fig. 9.19).

Fig. 9.20 shows the surface charge distributions for different applied fields. The "jitter" in this plot arises from the slightly different values across the height of the nanodot. The nanodot has been discretized by an unstructured mesh with four "layers" of finite elements. Thus, there are typically five nodes of the finite element mesh across the height of the dot and the values of the surface charge density of all five nodes has been plotted in Fig. 9.20.
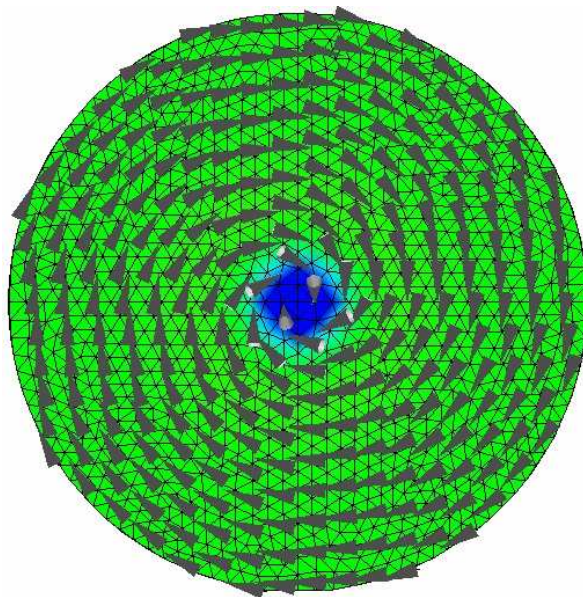
Figure 9.16: Contour plot of the surface charge density on the nanodot in zero field. Green indicates no surface charges, blue indicates negative surface charges.
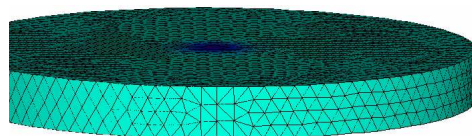
Figure 9.17: Contour plot of the surface charge density on the circumference of the nanodot in zero field.
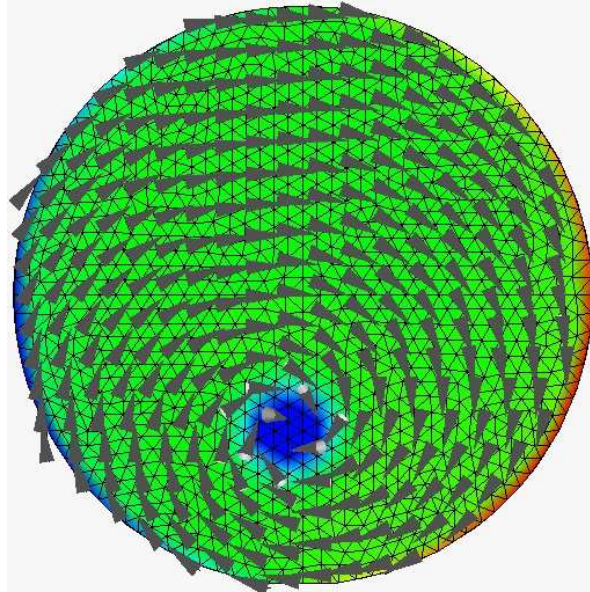
Figure 9.18: Contour plot of the surface charge density on the nanodot in an external field. Blue indicates negative charges, green zero charges, and red positive surface charges.
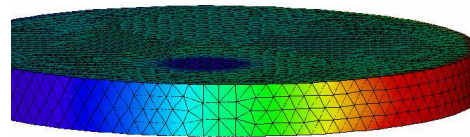
Figure 9.19: Contour plot of the surface charge density on the circumference of the nanodot in an external field.
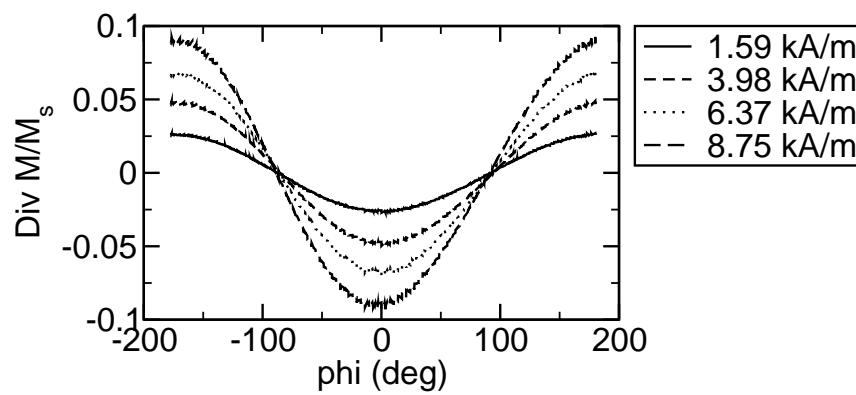
Figure 9.20: Surface charge density on the circumference of the nanodot for different applied fields.

The surface charge densities for different vortex core displacements, as calculated with the FE model, is given in Fig. 9.21.

The surface charge distributions have been calculated, as they are predicted by the rigid vortex model. A comparison of the results with the finite element model can be found in Fig. 9.22.

For small external fields and therefore small vortex displacements there is very good agreement between the analytical rigid vortex model and the finite element simulation. As the external field increases more surface charges appear on the circumference of the nanodot. However, the rigid vortex model overestimates these surface charges. The values for the average magnetization is in good agreement, but the surface charge distribution is not. The reason is, that the magnetization distribution close to the circumference is disturbed by the strong demagnetizing fields. As we further increase the external field and the vortex displacement this deviation becomes more and more pronounced. In addition, we also find some deviation in the center of the nanodot, which arises from a more "elliptical" shape of the magnetization distribution as the vortex is pushed towards the boundary. Contour plots of the difference between the magnetization distribution calculated by the FE simulation and the rigid vortex model $d = |\boldsymbol{M}_{\text{FE}} - \boldsymbol{M}_{\text{rv}}|$ are shown in Fig. 9.23 for $H_{\text{ext}} = 66.0$ kA/m $= 830$ Oe, $\langle M_x \rangle / M_{\text{s}} = -0.72$, and $b/R = -0.76$. The red areas at the circumference and in the center of the nanodot indicate differences between the rigid vortex model and the FE simulation.

In remanence, the demagnetizing field arising from the vortex structure is mainly concentrated in the vortex core (Fig. 9.24). It has a dominating z-component and a smaller radial component.

9.3.6 Phase Diagram

A summary of the results of the equilibrium magnetization distribution of nanodots with different aspect ratios is given in the phase diagram in Fig. 9.25. The transition from the in-plane magnetization to the vortex state is sharp, because this requires that the symmetry of the single domain state with (almost) homogeneous in-plane magnetization breaks in order to form the vortex state with cylindrical symmetry. The line separating the in-plane
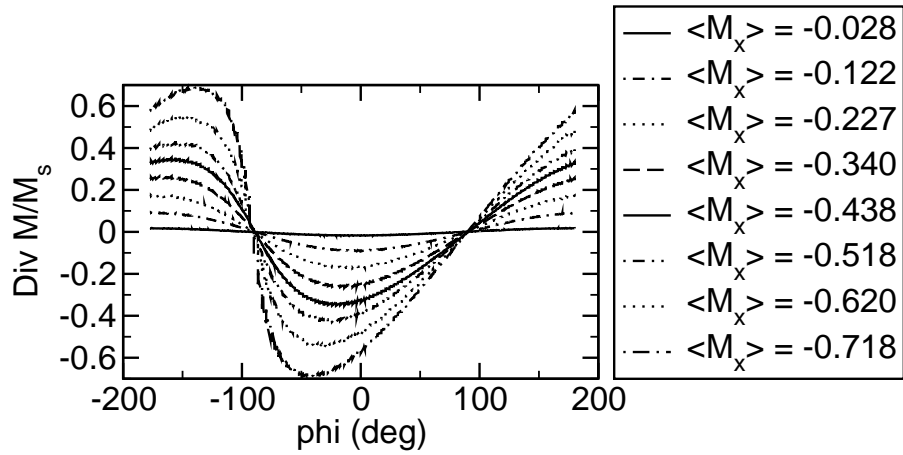
Figure 9.21: Surface charge distribution as a function of the polar angle on the circumference of the nanodot for different vortex shifts (indicated by different $\langle M_x \rangle$).
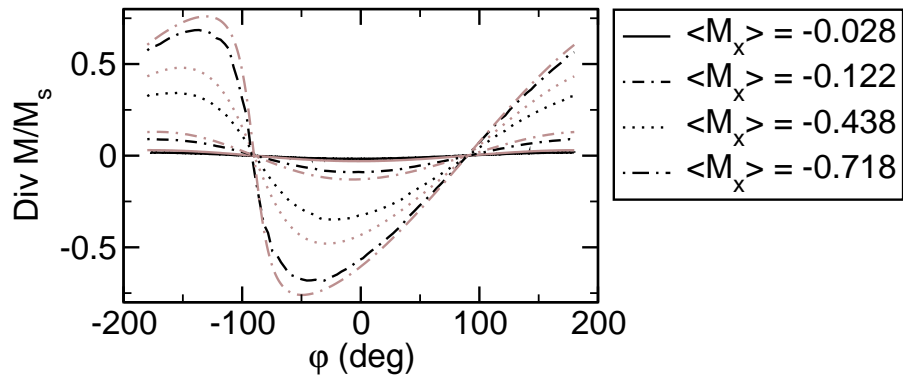
Figure 9.22: Surface charge distribution on the circumference of the nanodot as a function of the polar angle. An in-plane external field shifts the vortex (cf. Fig. 9.23) and leads to surface charges on the circumference. The rigid vortex model (gray lines) overestimates the charge density as compared to the FE simulation (black lines).
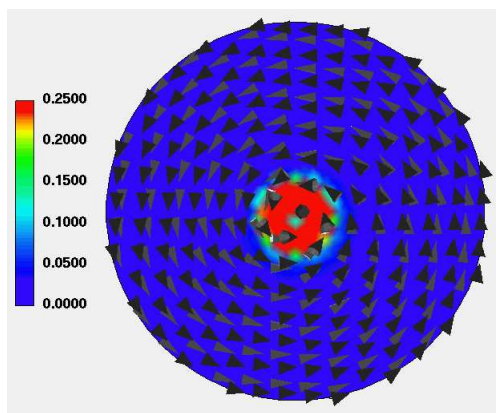
(a)
$H_{\text{ext}} = 0.8 \text{ kA/m} \,\hat{=}\, 10 \text{ Oe}$
$\langle M_x \rangle / M_\text{s} = -0.02$
$b/R = -0.03$
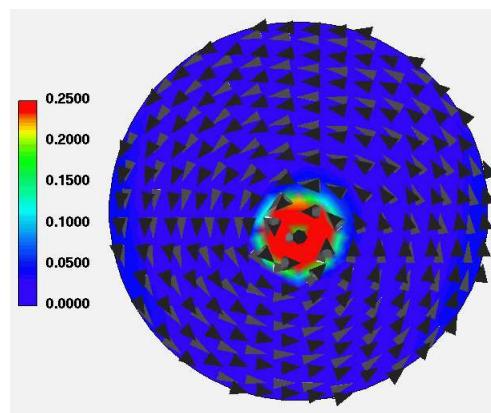
(b)
$H_{\text{ext}} = 8.8 \text{ kA/m} \,\hat{=}\, 110 \text{ Oe}$
$\langle M_x \rangle / M_\text{s} = -0.12$
$b/R = -0.13$
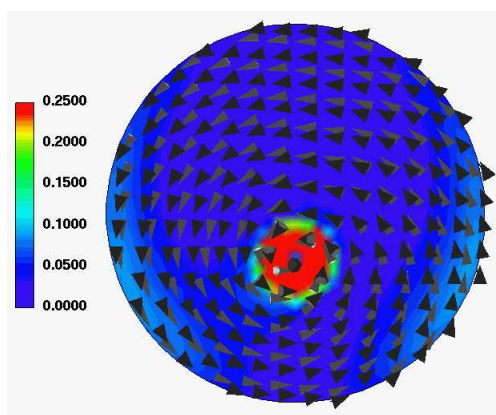
(c)
$H_{\text{ext}} = 16.7 \text{ kA/m} \,\hat{=}\, 210 \text{ Oe}$
$\langle M_x \rangle / M_\text{s} = -0.23$
$b/R = -0.25$
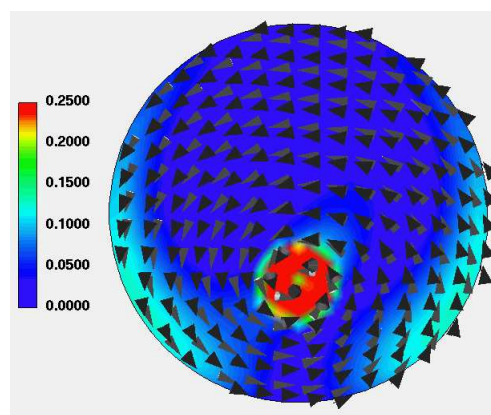
(d)
$H_{\text{ext}} = 25.5 \text{ kA/m} \,\hat{=}\, 320 \text{ Oe}$
$\langle M_x \rangle / M_\text{s} = -0.34$
$b/R = -0.37$

(Fig. cont. on next page)
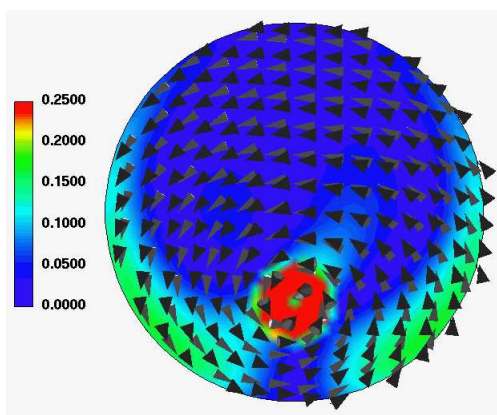
(e)
$H_{\text{ext}} = 34.2$ kA/m $\hat{=} 430$ Oe
$\langle M_x \rangle / M_{\text{s}} = -0.44$
$b/R = -0.48$
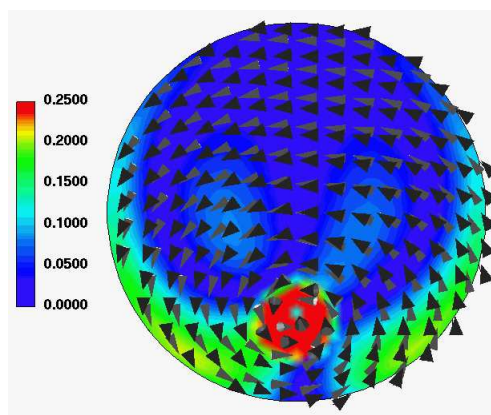
(f)
$H_{\text{ext}} = 42.2$ kA/m $\hat{=} 530$ Oe
$\langle M_x \rangle / M_{\text{s}} = -0.52$
$b/R = -0.57$
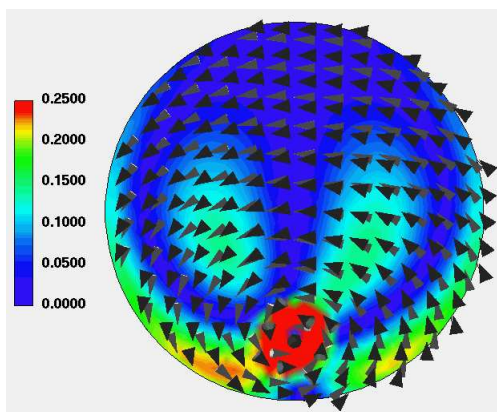
(g)
$H_{\text{ext}} = 54.1$ kA/m $\hat{=} 680$ Oe
$\langle M_x \rangle / M_{\text{s}} = -0.62$
$b/R = -0.67$
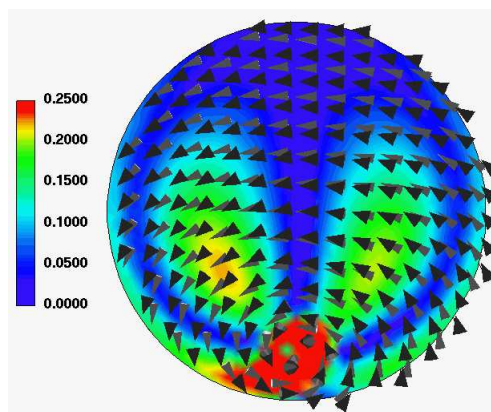
(h)
$H_{\text{ext}} = 66.0$ kA/m $\hat{=} 830$ Oe
$\langle M_x \rangle / M_{\text{s}} = -0.72$
$b/R = -0.76$

Figure 9.23: Contour plot of $d = |\boldsymbol{M}_{\text{FE}} - \boldsymbol{M}_{\text{rv}}|$. Blue areas indicate good agreement of the magnetization distribution between the rigid vortex model (black cones) and the FE model (gray cones), red areas indicate larger differences.
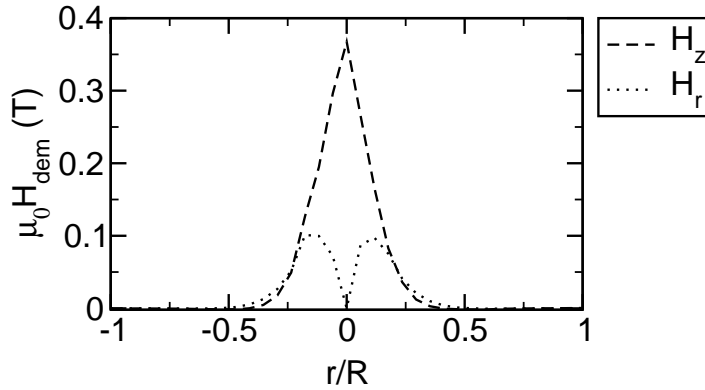
Figure 9.24: H_z^{dem} and H_r^{dem} across the nanodot.

and out-of-plane remanent states has a slope of 1.8, which is in agreement with the simulations by Ross et al. [105] and analytical calculations [121]. Magneto-optical measurements of hysteresis curves [110] also show a distinct change between these two regimes. The single domain particles retain high remanence and switch at very low fields, whereas a sudden loss in magnetization reducing the external field (cf. Fig. 9.9) is typical of a flux closure configuration (vortex state, cf. Fig. 9.26).

However, the transition from the vortex to the perpendicular magnetization (parallel to the cylinder axis) is not well defined. The numerical experiments show a smooth transition from one state to the other. For decreasing the dot aspect ratio, the magnetization starts to twist and exhibits very inhomogeneous magnetization distributions (Fig. 9.27). So we have defined a magnetization distribution with $M_z > 0.75$ as being a perpendicular ground state. The two-dimensional analytical model cannot describe this transition properly, because it would require, that the dependence of the magnetization on the z-coordinate is taken into account.

Nevertheless, the numerical results and the experimental data are in excellent agreement with analytical calculations of this phase diagram. The solid lines in Fig. 9.25 have been taken from the phase diagram presented in [122].

Experimental data have been obtained from arrays of soft magnetic cylindrical particles by Ross et al. [105] The data of their Ni samples are also shown in Fig. 9.25. The agreement with the numerically calculated phase diagram
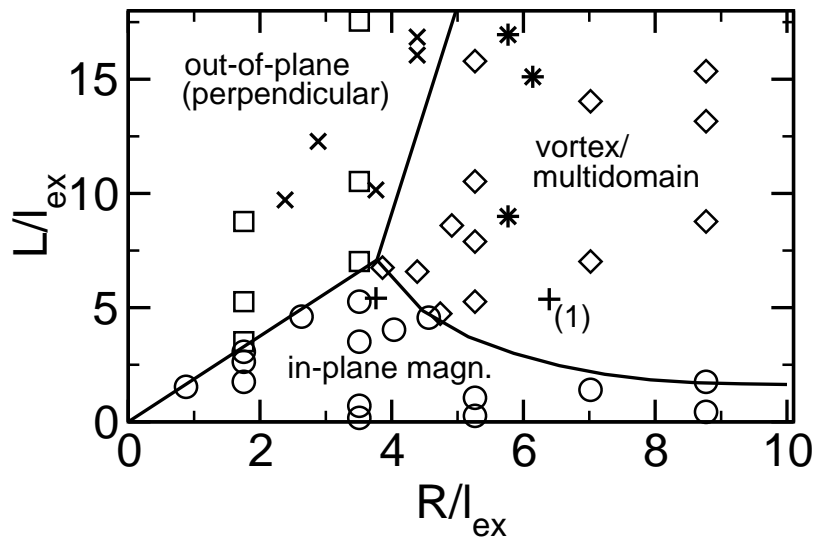
Figure 9.25: Phase diagram of magnetic ground states (axis scaling in units of the exchange length). The data points indicated by the open symbols have been calculated with the FE model. The circles (O) represent dots with lowest energy in the in-plane magnetization state, squares (□) those with perpendicular magnetization, and diamonds (◇) dots in vortex/multidomain state. The experimental data have been taken from Ross et al. [105] The crosses (×) indicate "Ni Type A" samples with out-of-plane (perpendicular) magnetization at remanence, the plus symbols (+) indicate "Ni Type B" samples with in-plane, and the asterisks (∗) "Ni Type C" samples with vortex or multidomain states, respectively. The experimental data nicely fit in the phase diagram with one exception, which is indicated by "(1)". There, a remanent state with in-plane magnetization has been found, where a vortex state might be expected. The solid lines give the analytical equilibrium single-domain radius calculated by Metlov et al. [122]

(a) $L/R = 1$, $R = 10$ nm

(b) $L/R = 1$, $R = 25$ nm

(c) $L/R = 1$, $R = 28$ nm
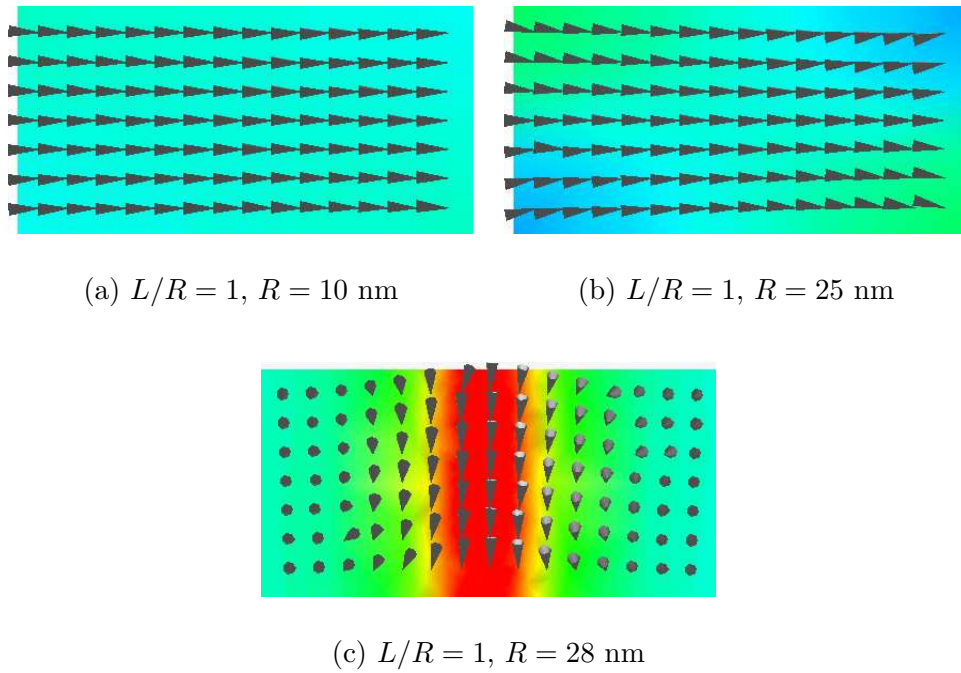
Figure 9.26: Equilibrium magnetization distributions in zero field inside the nanodots (cut along the cylinder axis) for dots with aspect ratios $L/R = 1$.
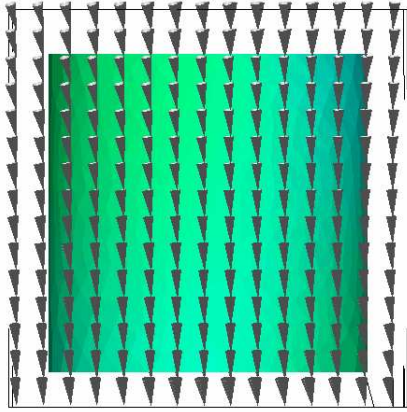
(a) $L/R = 2$, $R = 10$ nm
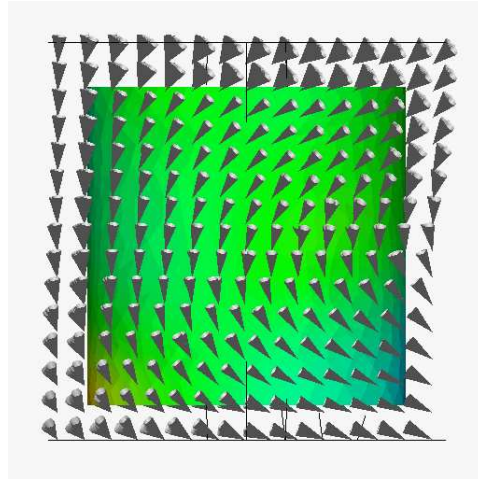
(b) $L/R = 2$, $R = 25$ nm
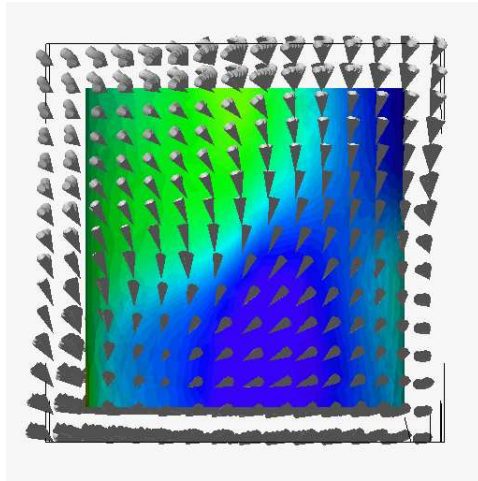
(c) $L/R = 2$, $R = 40$ nm

Figure 9.27: Magnetization distributions for dots with aspect ratios $L/R = 2$.

is very good. Only one data point does not fit in. A remanent state with in-plane magnetization is found, where a vortex state might be expected. However, also the smooth transition from the perpendicular magnetization to the vortex (multidomain) state has been found. Note, that ignoring the existence of the vortex core in nanodots [123] leads to an over-estimation of the total energy and, as a result, to wrong coordinates of the lines separating different magnetic states in soft magnetic cylindrical nanodots.

9.4 Dynamic Properties

The investigation and improved understanding of the dynamic processes in magnetic nanoparticles become more and more important as magnetic nanoparticles are promising candidates for high-speed, high-density magnetic storage (e.g. hard disks and MRAMs – magnetic random access memory devices) and sensor devices [124, 125].

Recent advances in nanometer scale fabrication technology allow detailed experimental investigations on a nanometer length scale [104, 105]. In high-speed storage devices magnetization reversal occurs by applying short field pulses [126]. The characteristic switching time depends on the reversal mode and is usually in the nanosecond regime. The magnetization reversal excites many spin-excitation modes (spin waves), whose understanding is important to determine the field dependent spin instability regions, where spontaneous or thermally-assisted magnetization reversal might occur [127].

The magnetization dynamics under short field pulses have been investigated in saturated NiFe disks [128] and in closure domains in Co disks [129]. However, the magnetization dynamics of the magnetic vortex state in thin Permalloy disks is markedly different from those in the uniformly magnetized state and also from the spin-waves observed in thin magnetic films.

9.4.1 Vortex Precession

The dynamic behavior of the magnetic nanodots has been studied by instantaneously applying an external field of 80 Oe (8 mT, 6.4 kA/m) in plane perpendicular to the dot axis. Even though the experiment was started from
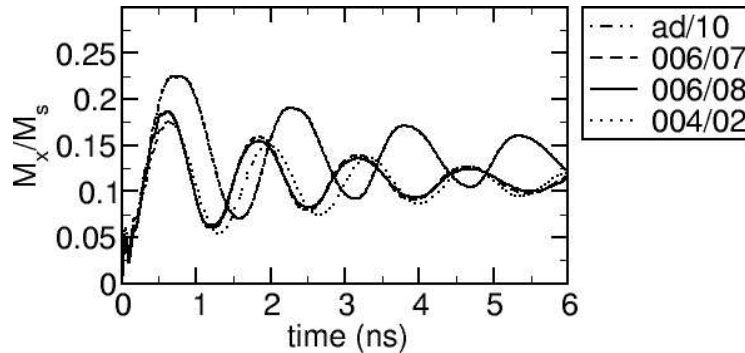
Figure 9.28: Oscillation of $\langle M_x \rangle$ as the vortex core precesses towards equilibrium.

the equilibrium magnetization distribution in zero field, M_x and M_y show a quite irregular behavior during the first 0.5 ns. During this time the vortex core "adapts" to the applied external field and deforms while it does already start its precession towards equilibrium. A low damping constant of $\alpha = 0.05$ has been used.

Figs. 9.28 and 9.29 show $\langle M_x \rangle$ and $\langle M_y \rangle$ as a function of time. Simulation "ad/10" uses an inhomogeneous mesh with very small finite elements (edge length 2 nm) in the center, where the vortex core is found in equilibrium, and a smooth transition to a coarser mesh outside the core (up to an edge length of 10 nm at the circumference – cf. Tab. 9.2). Simulation "006/07" uses a homogeneous mesh with an average mesh size of 6 nm, simulation "006/08" uses the same mesh with a shorter time step and simulation "004/02" uses a mesh with 4 nm edge length. Obviously, simulation "ad/10" exhibits strong deviations from the other results, because the vortex has to move into the coarser mesh as it is pushed out of the center of the nanodot due to the external field. However, the coarser mesh leads to a bad approximation of the vortex core and an inaccurate result.

In contrast, the simulations using the uniform meshes give results, which are in good agreement. The precession frequency of 0.65 GHz is also confirmed by the results of Guslienko and coworkers [130]. In addition it has been found, that the magnetostatic energy oscillates in phase with M_x (Fig. 9.30). This has to be ascribed to variations in the surface charge density on the circumference.
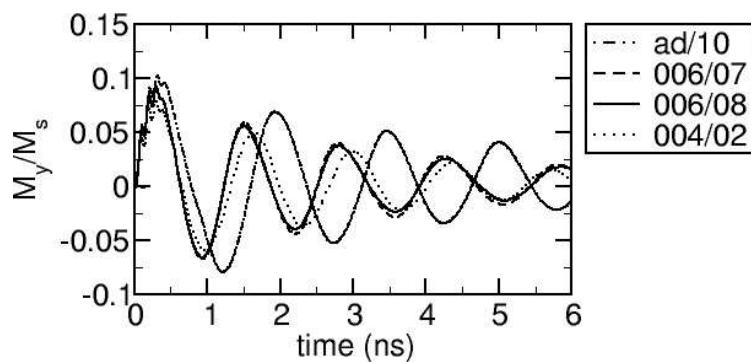
Figure 9.29: Oscillation of $\langle M_y \rangle$ as the vortex core precesses towards equilibrium.
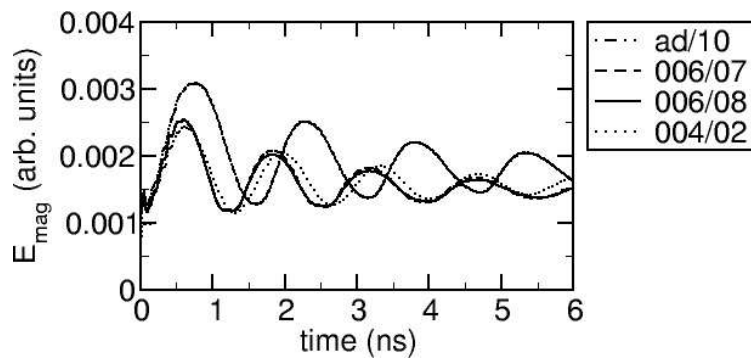
Figure 9.30: Oscillation of the magnetostatic energy.

The time evolution of $\langle M_x \rangle$ (the average of M_x over the whole nanodot) for a dot with an aspect ratio of $L/R = 10$ nm$/100$ nm $= 0.1$ is given in Fig. 9.31(a). Then the damped oscillation, which is caused by the spiral motion of the vortex core towards its equilibrium position, is observed. The corresponding Fourier spectrum is given in Fig. 9.31(b) and shows a sharp peak at a frequency of 0.7 GHz.

Fig. 9.32 shows the results of the translation mode eigenfrequencies of various nanodots with a radius $R = 100$ nm and a thickness between 10 nm and 40 nm. The results are in good agreement with the results of a finite difference model and the analytical "two-vortices" model presented in Ref. [130].

The decreasing total energy (dissipation due to damping with $\alpha = 0.05$ in the Landau-Lifshitz equation of motion) and the swapping between magnetostatic and Zeeman energy (which shifted by $180°$) are shown in Fig. 9.33. The exchange energy remains constant, because the vortex core, which accounts for most of the exchange energy, precesses without changing its shape. This confirms the analytical description of the translational mode suggested in Ref. [131].

Direct experimental observation of this mode in an isolated vortex using time-resolved Kerr microscopy has recently been reported by Park et al. [132]. There is good qualitative agreement with the analytical and numerical models, but still a few questions concerning the quantitative discrepancies and damping times remain open.

9.4.2   Discrete Fourier Transforms

In order to measure the oscillation frequency of the magnetization more accurately, the discrete Fourier transform of the discretely sampled data has been calculated. The different components of the magnetization distribution have been sampled at regular time intervals at different spots on and in the nanodot.

Thus, we have obtained N consecutive sampled values at a time interval Δ during the measurement time $\tau = N \cdot \Delta$. The accuracy of the discrete Fourier transform is determined by two fundamental numbers:
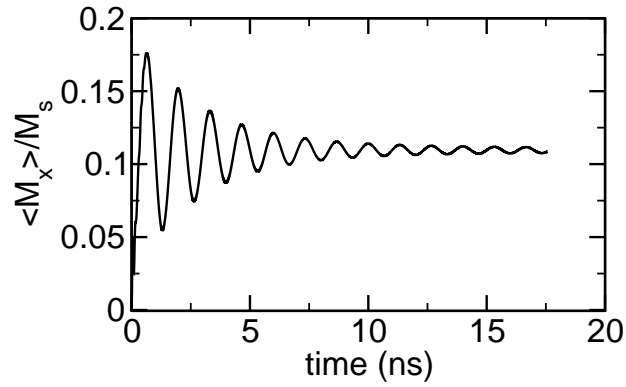
(a) Oscillation of $\langle M_x \rangle$ as a function of time.
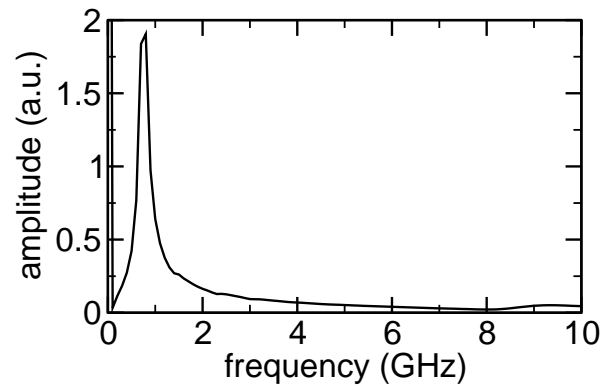
(b) Fourier spectrum

Figure 9.31: Simulation results for vortex precession in a nanodot with $L/R = 20$ nm$/100$ nm $= 0.2$ under applied in-plane field $\mu_0 H_x = 0.01$ T.
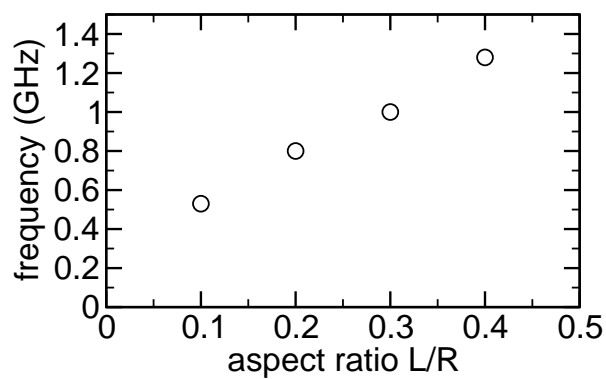
Figure 9.32: Translation mode eigenfrequencies versus aspect ratio L/R for nanodots with $R = 100$ nm.
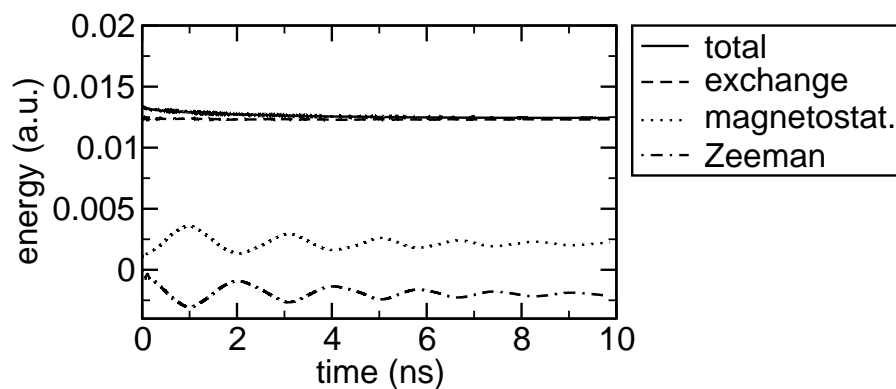
Figure 9.33: Energy over time for a dot with $L/R = 0.1$ and $\mu_0 H_x = 0.01$ T.

The Nyquist frequency [133]

$$f_N = \frac{1}{2 \cdot \Delta} \quad , \quad T_N = \frac{1}{f_N} = 2 \cdot \Delta$$

describes the maximum frequency, that can be measured, if the sampling interval Δ is given. The critical sampling of a sine wave requires two sampling points per cycle, the first at the positive peak and the second at its negative trough.

The minimum frequency, which also determines the "resolution" of the discrete Fourier transform (the minimum difference in frequency, which can be distinguished)

$$f_r = \frac{1}{T_r} = \frac{1}{N \cdot \Delta} = \frac{1}{\tau}$$

is given by the fact, that the maximum period, which fits into the measurement interval τ, is at most $T_r = \tau$.

Therefore, the discrete Fourier transform of a real valued function with N measurement samples each taken after a constant time interval Δ delivers $N + 1$ values for the amplitudes for a frequency spectrum from 0 (constant offset) to the Nyquist frequency f_N at frequency intervals f_r.

9.4.3 Radial Modes

Initially, an external field of 4 kA/m is applied parallel to the symmetry axis of the cylindrical nanodot (perpendicular to the circular plane on the top and bottom) and the Landau-Lifshitz-Gilbert equation is integrated with strong damping ($\alpha = 1$) until equilibrium is reached. Then the external field is switched off and the free oscillation in zero field is studied. The moment, when the external field is switched off, is also the starting time ($t = 0$) of our measurements.

Fig. 9.34 shows M_z as a function of the radius of the nanodot for different times. It shows the uniform oscillation of M_z across the whole radius. The amplitude of the oscillation is larger at the circumference of the nanodot and decreases towards the center. The vortex core remains almost undisturbed. The uniformity of the oscillation is even better visible in Fig. 9.35, where M_z
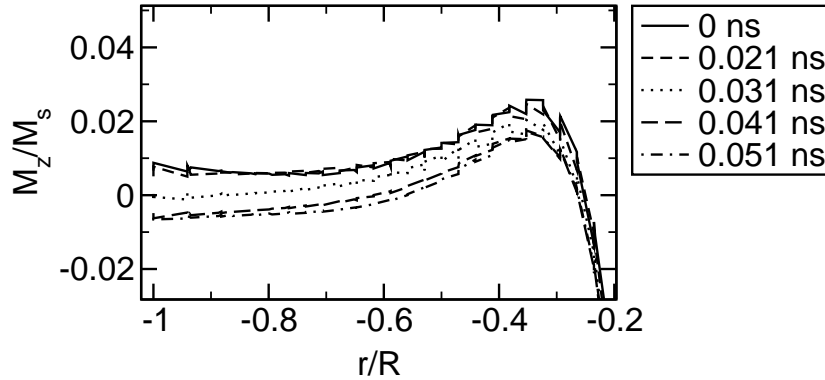
Figure 9.34: Snapshots of M_z as a function of the radius at different times during one oscillation period. The magnetization fluctuation outside the vortex core is very uniform, while the vortex core remains undisturbed ("rigid").

is plotted as a function of time for different radii. The oscillation is in phase for the chosen positions on the nanodot. The results for M_z are shown in Figs. 9.35 and 9.36. The main oscillation has a frequency of about 12 GHz, which is in excellent agreement with the analytical predictions. However, the error in the Fourier transforms is quite large, because the total sampling time covers only six oscillations. Thus, one can only estimate, that the true frequency is 12 ± 2 GHz.   Fig. 9.37 shows, that there is no phase shift or difference in amplitude between the oscillations of M_z at $(R|0)$ and $(0|R)$. The Fourier spectrum (Fig. 9.38) once again shows the peak at a frequency of 12 GHz.

Even more interesting than M_z is M_r for comparison with analytical results. Fig. 9.39 shows M_r as a function of the radius on the bottom circular plane, through the center and on the top circular plane of the nanodot. The oscillation of M_r is also very uniform (Fig. 9.40). However, a small decrease in the amplitude or a phase shift is observed close to the circumference. Still, the vortex core is once again hardly influenced. Fig. 9.41 shows the oscillation of M_r and M_z. As predicted by the rigid vortex model, there is a phase shift of 90°. The Fourier spectrum (Fig. 9.42) shows another time the peak at 12 GHz.   Also M_r is nicely in phase at different positions on the circumference (Fig. 9.43) and oscillates at the expected 12 GHz (Fig. 9.44). Finally, it is also worth to have a look at M_φ. Its variation is only very small
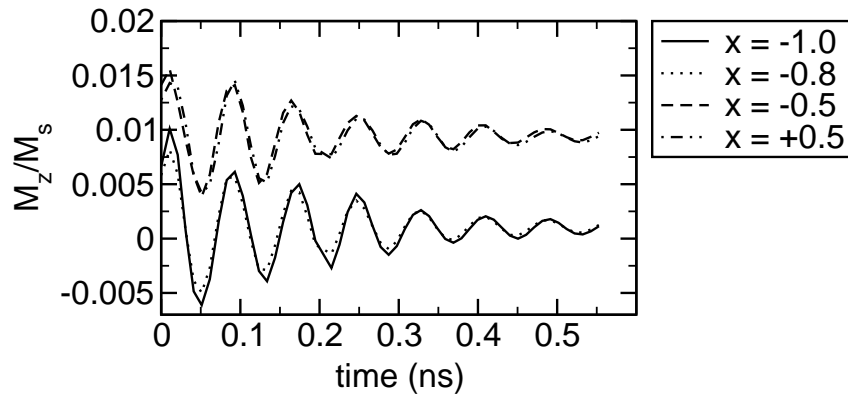
Figure 9.35: M_z as a function of time at different radii. The magnetization is perfectly in phase in all spots, which emphasizes the uniformity of the excitation mode.
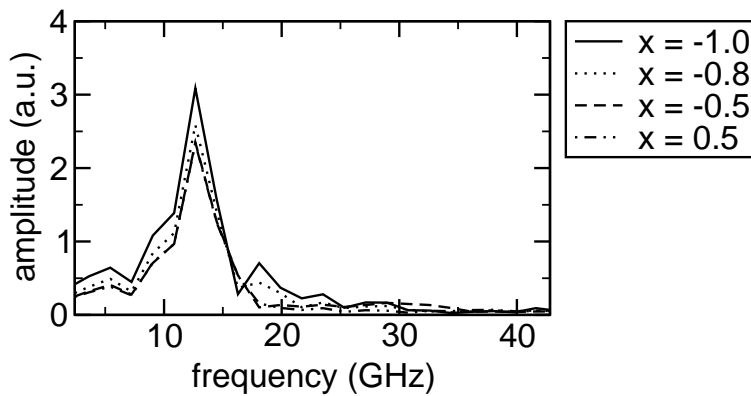
Figure 9.36: Fourier spectrum of M_z (of Fig. 9.35) at different radii.
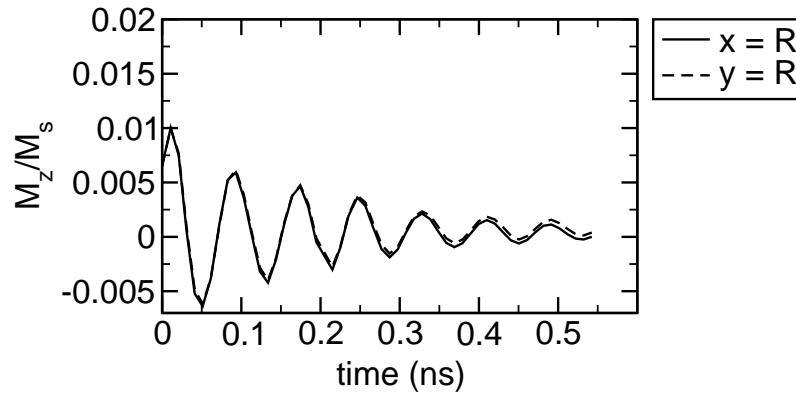
Figure 9.37: M_z as a function of time at $(R|0)$ and $(0|R)$.
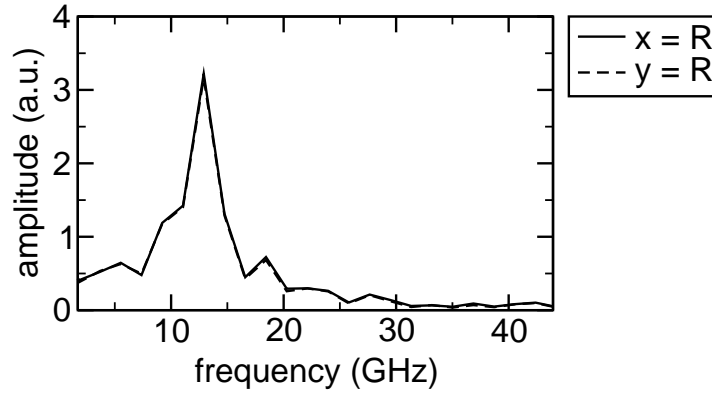
Figure 9.38: Fourier spectrum of M_z (of Fig. 9.37) at $(R|0)$ and $(0|R)$.
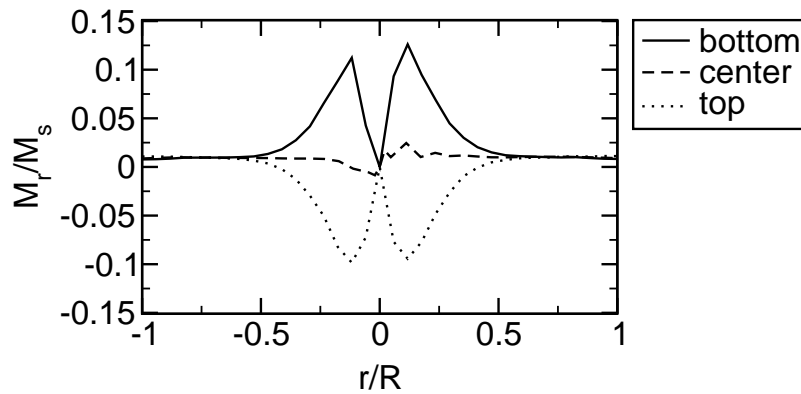
Figure 9.39: M_r as a function of the radius at different z positions.
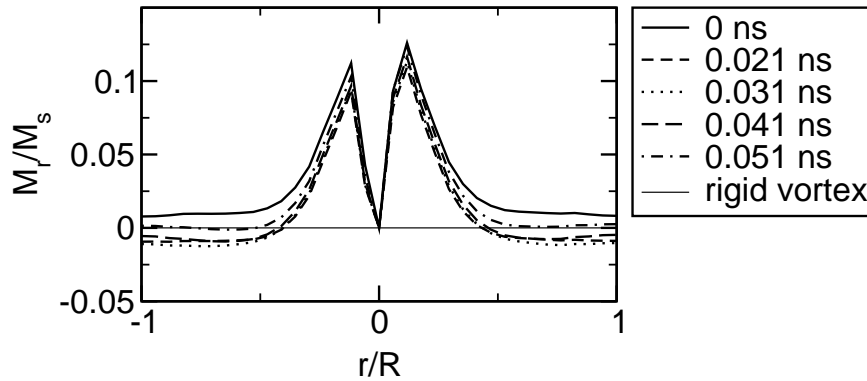
Figure 9.40: M_r as a function of the radius at different times.
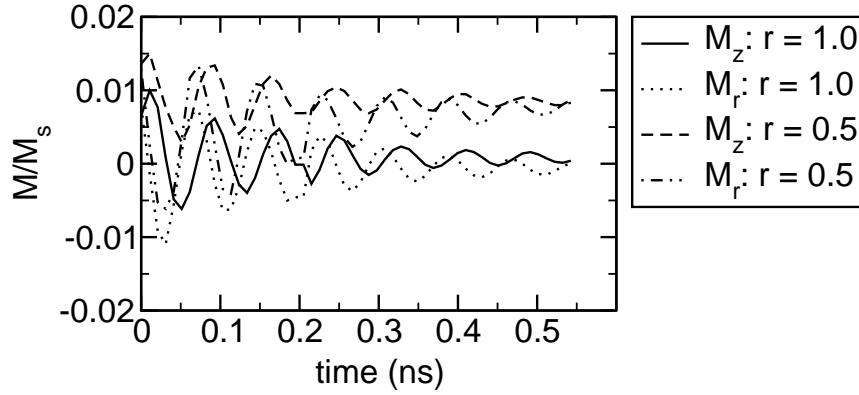
Figure 9.41: M_r and M_z as a function of time at different radii.
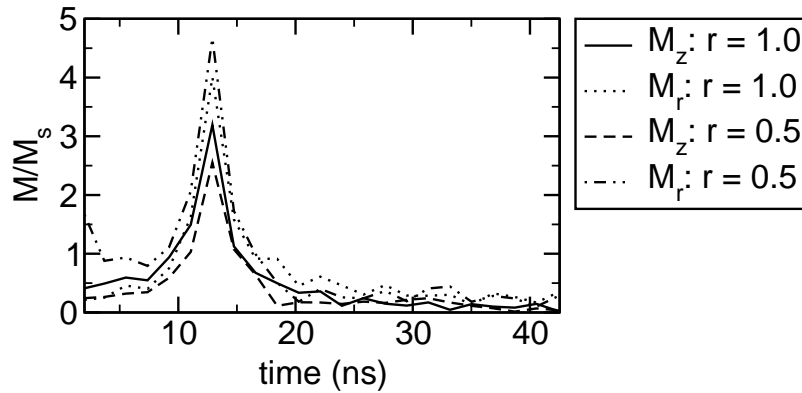
Figure 9.42: Fourier spectrum of M_r and M_z (of Fig. 9.41) at different radii.
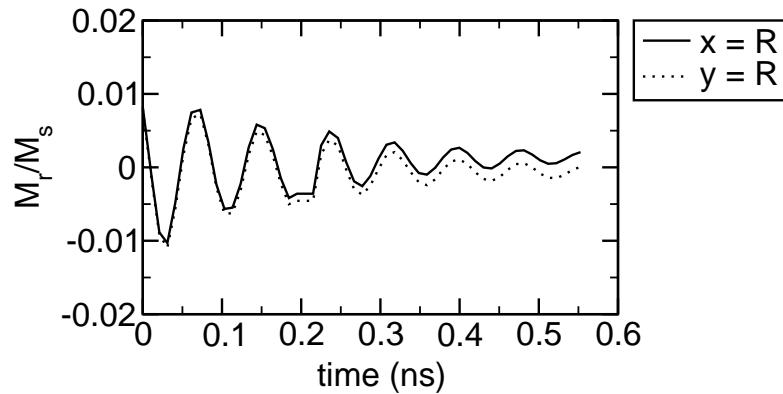
Figure 9.43: M_r as a function of time at $(R|0)$ and $(0|R)$.
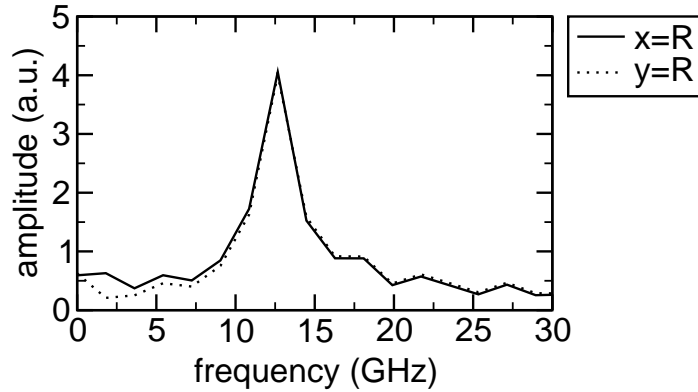
Figure 9.44: Fourier spectrum of M_r (of Fig. 9.43) at $(R|0)$ and $(0|R)$.
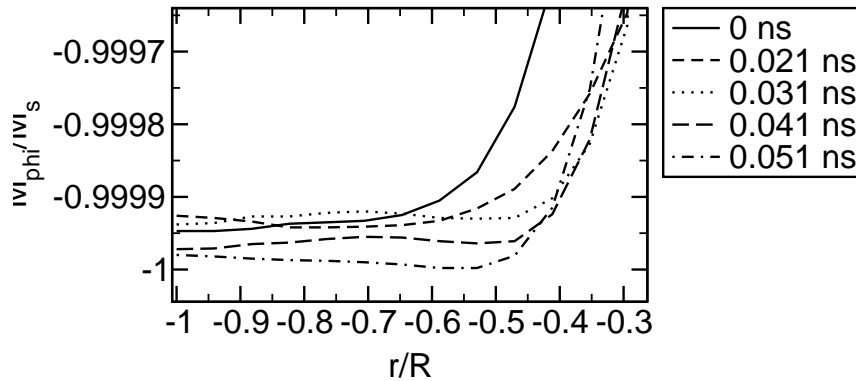
Figure 9.45: M_φ as a function of the radius at different times.

(Fig. 9.45), and oscillates at 12 GHz (Fig. 9.46).

In order to get a more accurate Fourier transform, another simulation with a very small damping constant of $\alpha = 0.0001$ has been made. With this small damping constant it takes many cycles until the oscillation is damped out. Thus, the measurement time is a lot longer, which leads to a Fourier transform with higher resolution.

The time dependence of the average magnetization $\langle M_z \rangle$ and the Fourier spectra for nanodots with an aspect ratio of $L/R = 20\ \text{nm}/100\ \text{nm} = 0.2$ and $L/R = 40\ \text{nm}/200\ \text{nm} = 0.2$ are given in Figs. 9.47(a) and (b) and 9.48(a) and (b), respectively.

For constant aspect ratio $L/R = 0.2$ we find an eigenfrequency of approximately 12.6 GHz. However, for a nanodot with $L/R = 40\ \text{nm}/200\ \text{nm} = 0.2$
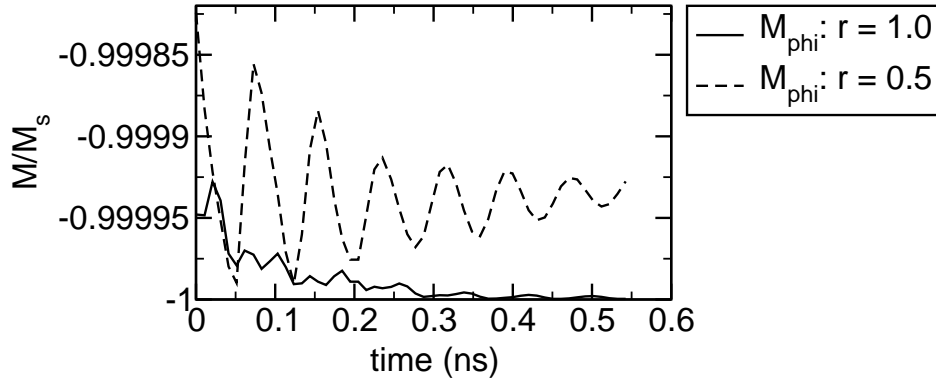
Figure 9.46: M_φ as a function of time at different radii.

a very pronounced beating is observed (Fig. 9.48). This is due to the fact, that there is another eigenfrequency of 11.6 GHz very close to the 12.6 GHz oscillation. However, the main peak position depends only on the combination ratio L/R. This confirms the magnetostatic origin of the mode. But the physical picture is more complicated for large L, when the magnetization dependence on z may be essential. Our numerical calculations confirmed that the eigenfunctions which correspond to low-lying part of the vortex dot excitation spectrum have radial symmetry.
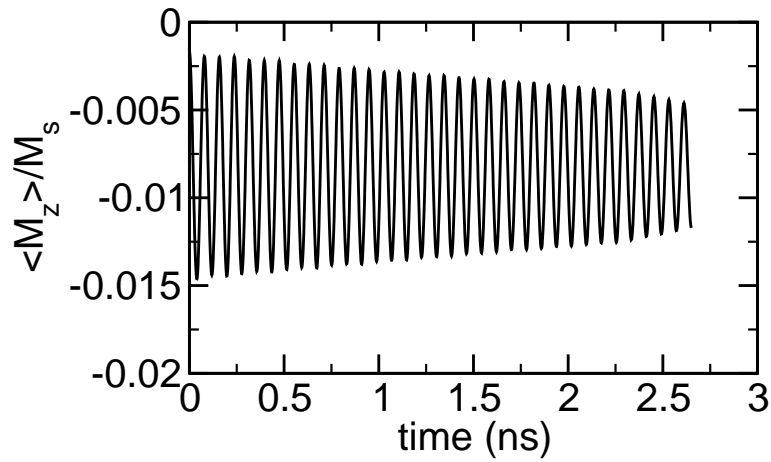
(a) Oscillation of $\langle M_z \rangle$ as a function of time.
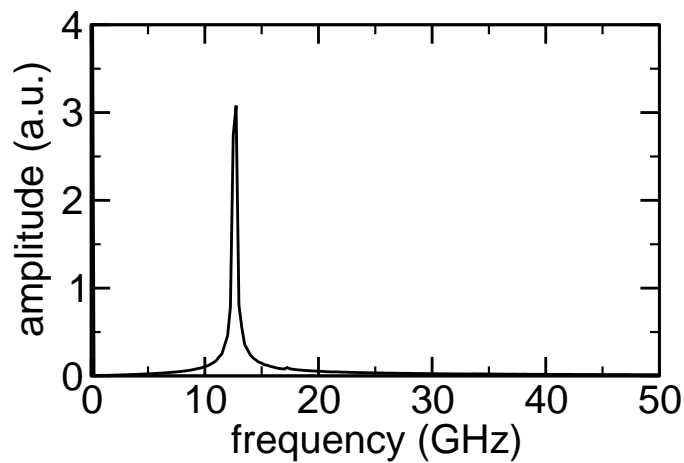
(b) Fourier spectrum

Figure 9.47: Simulation results for a nanodot with $L/R = 0.2$ under applied out-of-plane field $\mu_0 H_z = 0.005$ T.
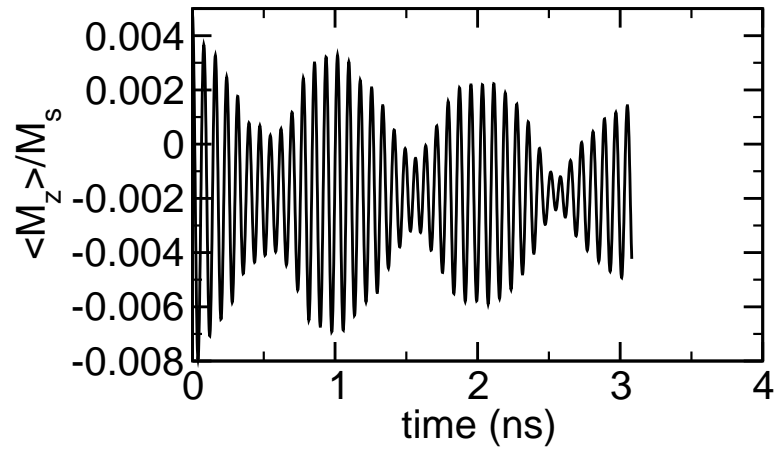
(a) $\langle M_z \rangle$ as a function of time.
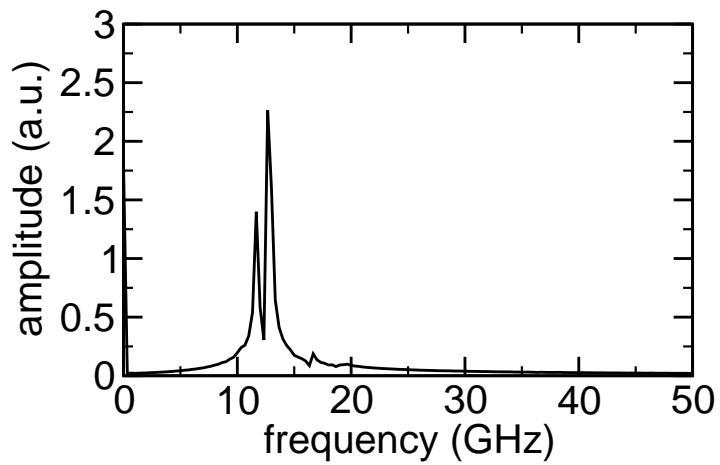
(b) Fourier spectrum

Figure 9.48: Simulation results for a nanodot with $L/R = 40$ nm/200 nm = 0.2.

9.5 Conclusions

A detailed comparison of the rigid vortex model for magnetic vortex states in soft magnetic nanodots with the finite element simulations has revealed some special features of the magnetic vortex state:

- The magnetization distribution near the vortex core radius ($r = a$) deviates essentially from Usov's analytical model. Especially a non-vanishing radial component M_ρ has been found (Fig. 9.39).

- In addition to the magnetic surface charges in the core of the vortex, the finite element simulations have revealed a ring of weak surface charges with opposite sign around the core of the nanodot.

- The shape of the vortex core and its exchange energy have been found to be very stable ("rigid") even for large vortex shifts in an external field.

- However, the surface charges on the circumference of the nanodot are overestimated by the rigid vortex model, because the magnetization distribution is distorted from the perfectly circular shape by the magnetostatic stray field. As a result, the surface charges and the magnetostatic energy are reduced as compared to the rigid vortex model.

- The phase diagram of magnetic ground states shows sharp transitions from the "in-plane" state to the perpendicular magnetization distribution and the magnetic vortex state, whereas the transition from the perpendicular magnetization to the magnetic vortex state is not well defined.

- Vortex precession in an in-plane external field has been observed and compared with finite difference simulation. Very good agreement for the precession frequency has been found for suitable finite element meshes.

- The radial mode has been studied in detail. The results show, that the core remains almost undisturbed and this (radially symmetric) mag-

netostatic eigenfunction can be approximately described as a uniform mode without side surface charges.

Chapter 10

Elliptical Permalloy Nanoparticles

Magnetic nanoparticles have seen growing interest in recent years due to advances in fabrication, observation [134], and computational techniques [135]. Since the typical size of these particles approach the magnetic domain wall width (nm to μm range) new effects appear and can be exploited for applications. Transport phenomena and magnetoresistance effects in particular are intensively studied. In experiments different magnetic domain configurations and domain walls have been found to influence MR effects [136, 137].

In this work magnetic nanoparticles of permalloy ($Ni_{80}Fe_{20}$) have been investigated. Micromagnetic simulations based on the Gilbert equation of motion of the magnetization have been carried out to study the magnetic reversal processes and domain configurations in single particles, arrays of isolated particles and connected (exchange coupled) particles with contact faces of different size.

The magnetic domain wall width in permalloy is approximately as large as the long axis of the particles, but effects of the magnetostatic stray field and small contact faces can stabilize certain domain configurations. The remaining domain walls can be used to investigate MR effects.
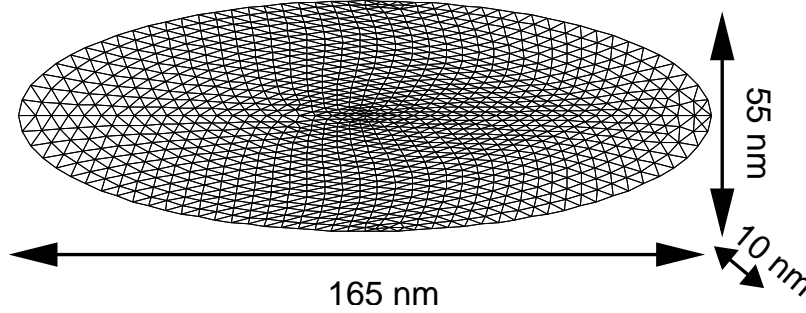
Figure 10.1: Shape and finite element mesh of an elliptical nanoparticle.

J_{s} (T)	1
A (pJ/m)	13
K_1 (MJ/m^3)	≈ 0
$l_{\mathrm{s}} = \sqrt{2\mu_0 A/J_{\mathrm{s}}^2}$ (nm)	5.7
$l_{\mathrm{K}} = \sqrt{A/K_1}$ (nm)	161

Table 10.1: Material parameters for permalloy.

10.1 Single Particle

10.1.1 Geometry and Material Parameters

The elliptic particles have a long axis of 165 nm, a short axis of 55 nm and a thickness of 10 nm. Their shape and the finite element mesh, which consists of 5068 nodes and 23188 elements, are given in Fig. 10.1. The material parameters of permalloy (Ni$_{80}$Fe$_{20}$), which have been used for the simulations, are given in Tab. 10.1.

10.1.2 Magnetization Reversal

When a single elliptical particle is initially magnetized parallel to its long axis, which is also the remanent state due to the shape anisotropy, it requires an (antiparallel) external field of 239 kA/m to reverse its magnetization. The magnetization reversal process is very inhomogeneous (cf. Fig. 10.2).
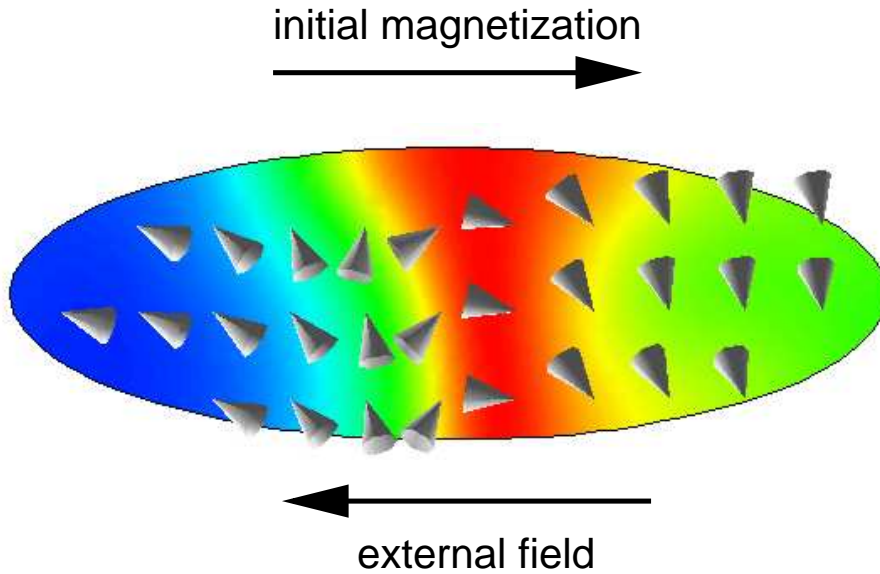
Figure 10.2: Snapshot of the magnetization reversal process of a single particle.

10.2   Chain of Particles

The behavior of a chain of isolated elliptical nanoparticles is strongly influenced by the magnetostatic stray fields. The demagnetization curves are given in Fig. 10.4. The external field is parallel to the long axis of the particles. If the particles are initially magnetized parallel to each other and the long axis of the particles, the magnetization reversal occurs at an external field of 72 kA/m. However, if the magnetization of each particle is initially antiparallel to that of its neighbors, that particle at one end of the chain, whose magnetization is antiparallel to the external field, reverses at 87 kA/m. The two other particles inside the chain, whose magnetization is antiparallel to the external field, reverse at 104 kA/m. Thus, the stray field stabilizes the antiparallel magnetized particles and increases the switching field by 44%. Snapshots of the magnetization reversal process are shown in Fig. 10.3.

10.2.1   Particles with Rectangular Shape

In order to study the influence of the shape of the nanoparticles another set with rectangular shape has been created. Each particle is a hexahedron

(a) Initially parallel magnetization.

(b) Initially antiparallel magnetization.
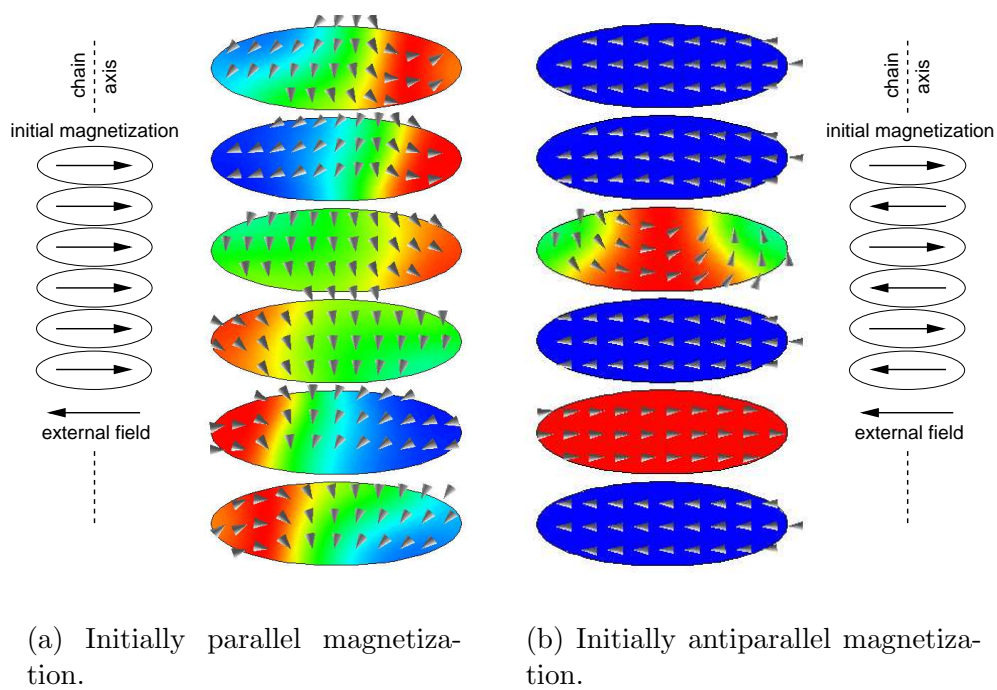
Figure 10.3: Snapshot of the magnetization reversal process of a chain of six elliptical particles.
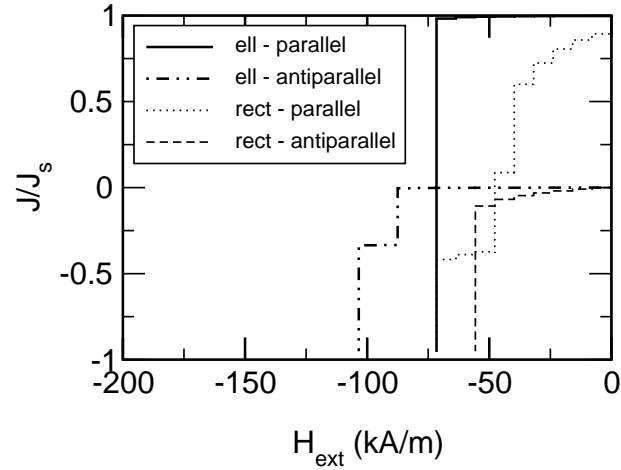
Figure 10.4: Demagnetization curves for a chain of elliptical and rectangular particles with parallel and antiparallel initial magnetization.

with $165 \times 55 \times 10$ nm edge length. The particles are separated by 5 nm. The demagnetization curve for parallel and antiparallel alignment and in comparison with elliptical particles is given in Fig. 10.4.

Due to the inhomogeneous magnetization of the rectangular particles in equilibrium, the chain of rectangular particles is not as stable as that of elliptical particles. Thus, the magnetization drops already for small external fields and the switching fields are considerably lower. The switching field is 56 kA/m for antiparallel initial magnetization. The demagnetizing curve of the initially parallel magnetized particles shows a plateau at $J/J_\text{s} = -0.38$, which is again caused by the stabilizing effect of the outer particles, which have switched already. Snapshots of the magnetization reversal process are given in Fig. 10.5. In contrast to the elliptical particles (cf. Fig. 10.3(a)), which reverse their magnetization almost at the same time, the rectangular particles do so consecutively. Thus, a stabilized antiparallel pattern is formed.
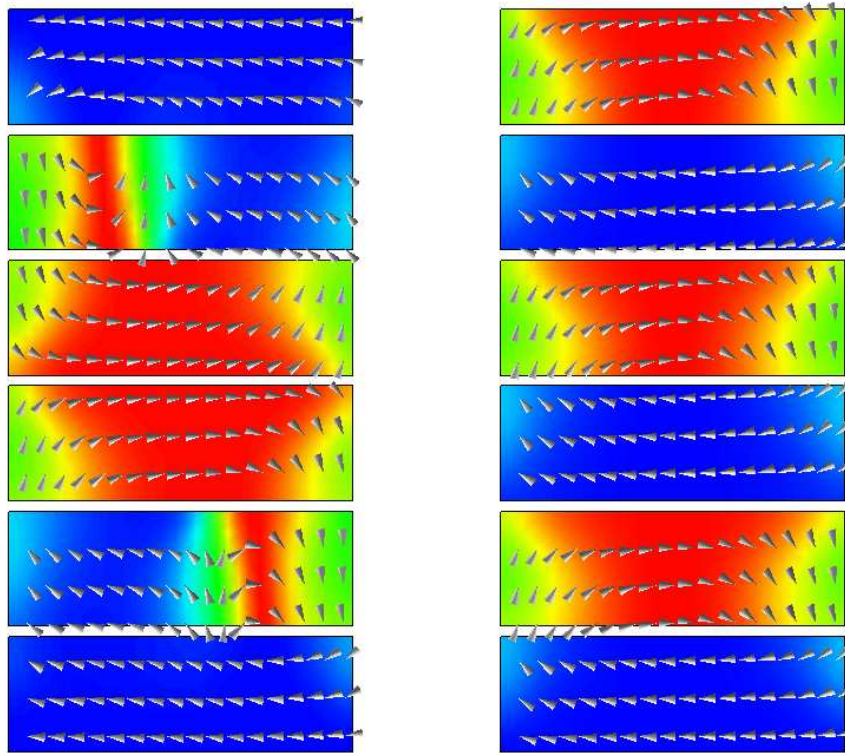
(a) Initially parallel magnetiza-
tion.

(b) Initially antiparallel magneti-
zation.

Figure 10.5: Snapshot of the magnetization reversal process of a chain of six
rectangular particles.
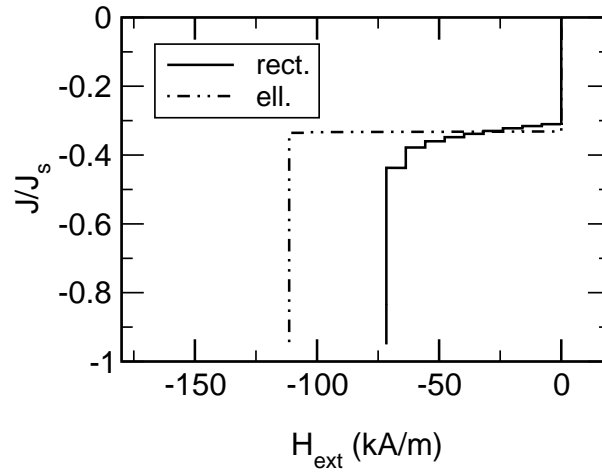
Figure 10.6: Chain of particles with the initial magnetization parallel to the chain axis.

10.2.2 Behavior in an External Field Parallel to the Chain Axis

If the initial magnetization of the particles is parallel to the axis of the chain and the short axis of the particles, the behavior in zero field is also dominated by the magnetostatic stray field. The demagnetization curves for elliptical and rectangular particles are given in Fig. 10.6. The snapshots of the particles given in Fig. 10.7 shows how the magnetization of the particles at the end of the chain tries to align parallel to the long axis. As soon as the symmetry of this metastable state breaks, the stray field leads to an antiparallel alignment of the magnetization of the neighboring particles. By chance, the particles at the end of the chain choose one or the other direction but in any case the stray field causes the antiparallel alignment of the neighboring particle. Since the particles at the end of the chain chose the same direction, the magnetization of those in the center is parallel.

10.2.3 Elliptical Particles with Contact Faces

Finally the influence of contact faces, which is necessary for electrical contact in MR experiments, between the particles has been investigated. This contact causes exchange coupling of the magnetization of the particles and has a
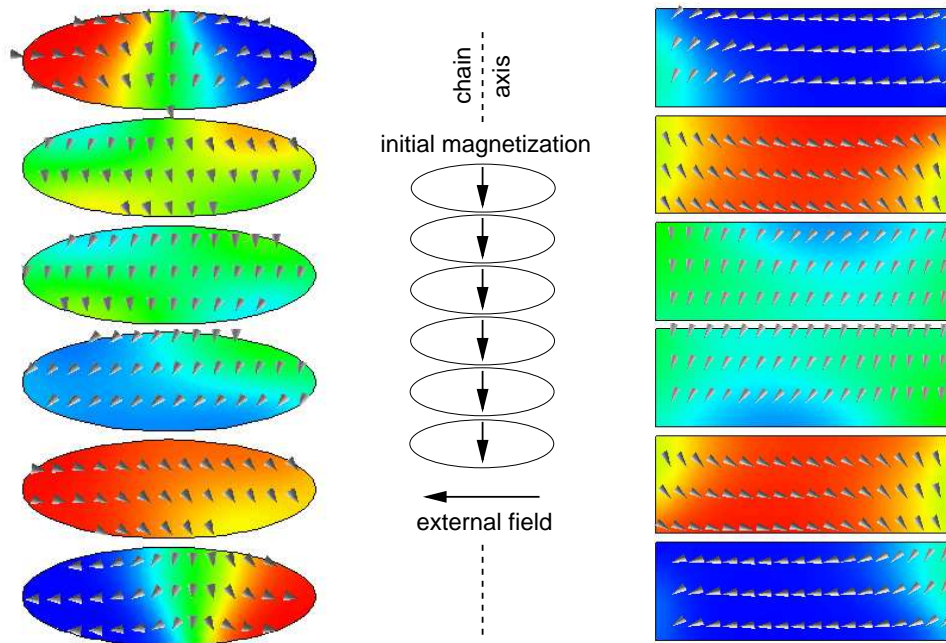
Figure 10.7: Snapshot of the relaxation process of a chain of six elliptical and rectangular particles with their initial magnetization parallel to the chain axis.
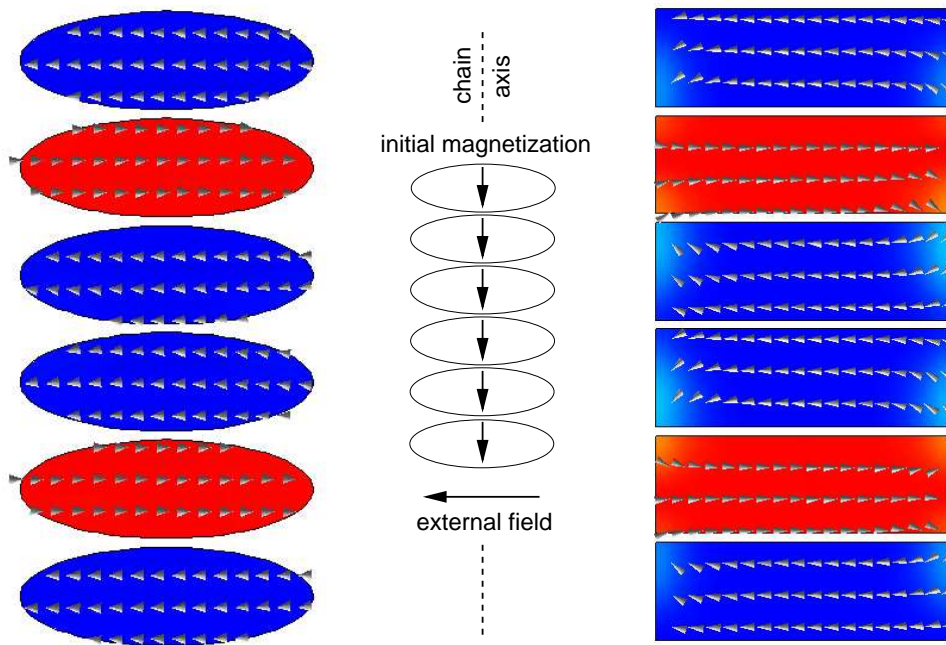
Figure 10.8: Equilibrium magnetization distribution in zero field of a chain of six elliptical and rectangular particles with their initial magnetization parallel to the chain axis.
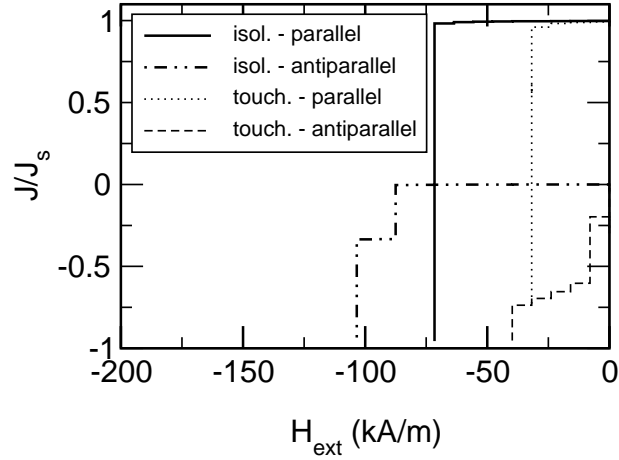
Figure 10.9: Demagnetization curves for a chain of elliptical particles with ("touch." – 50×10 nm) and without ("isol.") contact faces with parallel and antiparallel initial magnetization.

strong influence on the domain patterns.

First, a rather large contact face of 50×10 nm between the elliptical particles was assumed. The demagnetization curves in Fig. 10.9 show, that the switching field of the particles with initially parallel magnetization is reduced by more than 50%. For the particles with initially antiparallel magnetization we find a new behavior: The exchange coupling of the particles overrides the shape anisotropy and causes the formation of domains which extend over several particles. The equilibrium magnetization distributions are given in Fig. 10.10.

However, if we reduce the size of the contact faces to 10×10 nm we can "pin" these domain walls (we should rather call it an area of transition of the magnetization, since it is strictly speaking not a domain wall) at the contact faces. The demagnetization curves for these small contact faces in comparison with isolated particles are given in Fig. 10.11. A comparison of the demagnetization curves between small and large contact faces is given in Fig. 10.13. The magnetization distribution in equilibrium is shown in Fig. 10.12. If the particles are initially magnetized parallel to the chain axis, the exchange coupling is still strong enough to suppress the spontaneous formation of the antiparallel pattern (cf. Fig. 10.12(b)). When the external field is switched on, the magnetization of the inner particles rotates
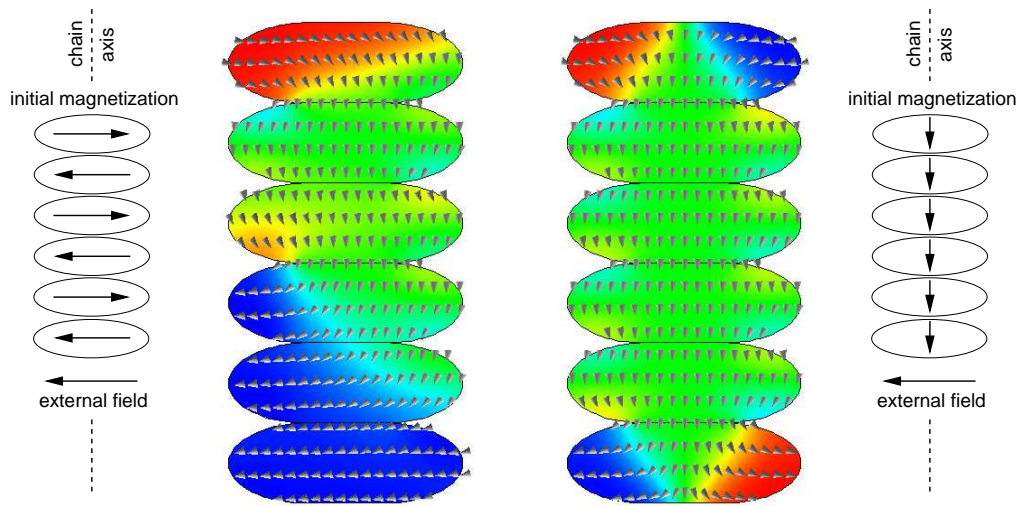
(a) Initially antiparallel magnetiza-
tion.

(b) Initial magnetization parallel to
the chain axis.

Figure 10.10: Equilibrium magnetization distribution in zero field of a chain
of 6 elliptical particles with a contact area of 50×10 nm.
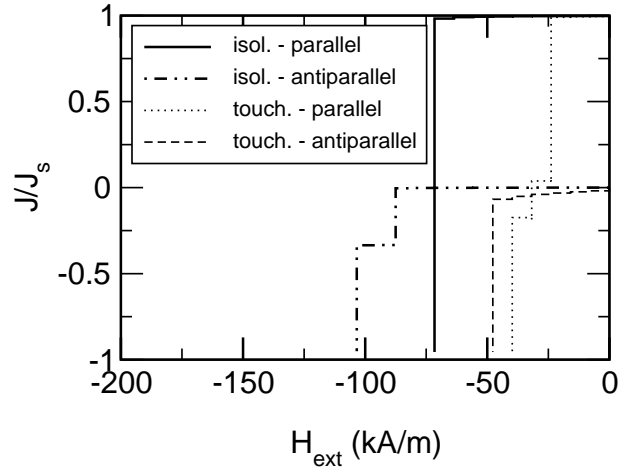
Figure 10.11: Demagnetization curves for a chain of elliptical particles with ("touch." – 10×10 nm) and without ("isol.") contact faces with parallel and antiparallel initial magnetization.

homogeneously into the direction of the external field.

10.3 Conclusions

In summary, we have studied magnetization reversal processes of permalloy nanoparticles of elliptical and rectangular shape by 3D dynamic finite element micromagnetic simulations. The results show the strong influence of the shape and the demagnetizing field on the behavior of the particles. Even without magnetocrystalline anisotropy stable domain configurations with the magnetization perpendicular to the axis of a chain of particles can be obtained. The shape anisotropy and demagnetizing field lead to a spontaneous antiparallel alignment of the magnetization of neighboring particles. If the particles have very small contact faces, a stable configuration with antiparallel magnetization in neighboring particles is found in spite of exchange coupling. This effect can be used in experiments to study magnetoresistive effects in nanoparticles of materials without magnetocrystalline anisotropy.
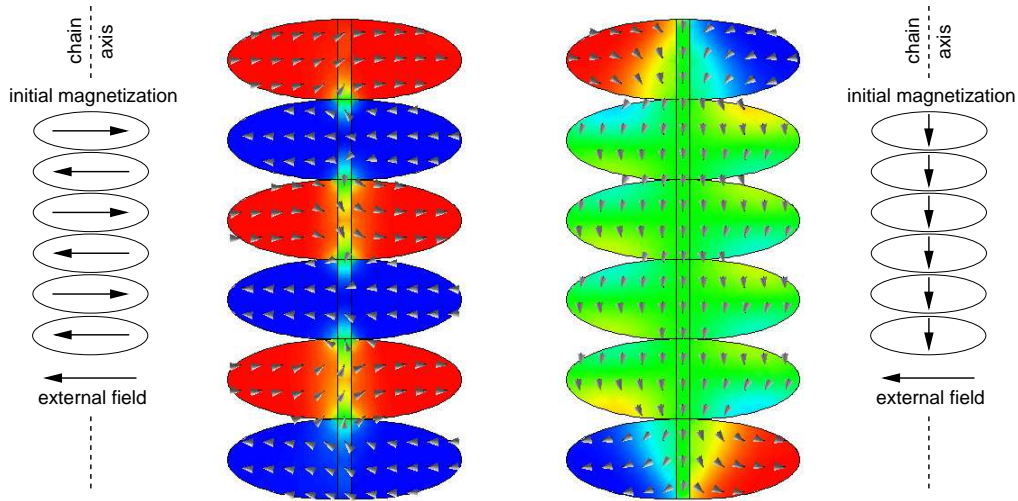
(a) Initially antiparallel magnetization.

(b) Initial magnetization parallel to the chain axis.

Figure 10.12: Equilibrium magnetization distribution in zero field of a chain of six elliptical particles with a contact area of 10×10 nm.
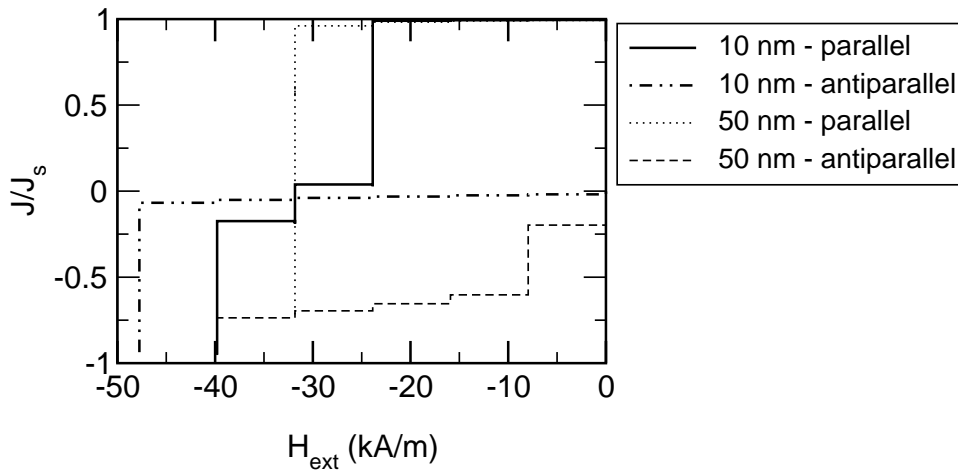
Figure 10.13: Demagnetization curves for a chain of elliptical particles with 10×10 nm and 50×10 nm contact faces with parallel and antiparallel initial magnetization.

Conclusions and Outlook

For this thesis a scalable parallel finite element micromagnetics package has been developed. It is entirely based on free open source software packages, which have been selected for performance, scalability, portability, and ease of use. The combination of static energy minimization, time integration, and the nudged elastic band method makes it a very efficient and versatile tool, which has been used for the investigation of magnetic nanostructures.

In SmCo precipitation hardened magnets the coercivity is dominated by domain wall pinning on the precipitation structure. The detailed study of the pinning process has shown the influence of the material properties, the intercellular phase, and the cell geometry. Exchange decoupling can considerably improve the coercivity, but the thickness of the intercellular phase has to be in the optimum range between one and four times the domain wall width.

Magnetic nanoparticles of FePt are possible candidates for future magnetic storage media. The dependence of the nucleation and coercive fields on the distribution of easy axes has been investigated. It has been found, that a single misaligned axis reduces the coercivity by a factor of three. The coercivity is further decreased if more misaligned axes are assumed and if the particle size gets in the order of the domain wall width.

Another interesting system are magnetic nanodots, which exhibit curling magnetic structures (vortices). The calculation of their static properties shows the competition between exchange and magnetostatic energy. A phase diagram of the magnetic ground states has been obtained and compared with analytical and experimental investigations. The dynamic properties, which are important for high-speed, high-frequency applications, of vortex precession and radial modes have also been studied.

The behavior of chains of soft magnetic elliptical nanoparticles is also strongly influenced by magnetostatic interactions. These lead to antiparallel magnetization distributions, which remain stable even in the presence of exchange coupling between the particles.

In summary, the parallel micromagnetics code has proved its performance and scalability and provided insight into the magnetization reversal processes of magnetic nanostructures. The different solvers have been applied to different problems of magnetic domain wall pinning, nucleation, and magnetization dynamics. The high spatial resolution, which is required in hard magnetic materials like SmCo and FePt with very thin domain walls, could be achieved owing to the parallelization, data distribution, and efficient energy minimization method. The magnetization dynamics have been studied with a preconditioned time integration method, which allows large time steps and long integration times. Improved experimental investigations with higher spatial resolution will be necessary to obtain more accurate material parameters for the simulation of permanent magnets, and a higher time resolution is also required for the detailed investigation of the magnetization dynamics in magnetic nanoelements.

Still, many interesting effects have been neglected, such as thermal activation and the influence of eddy currents, for example. Efficient time integration methods for Langevin micromagnetic simulations including thermal activation are an active research area [138]. However, new solvers can be easily added to the program to consider also thermal effects. Eddy currents are often calculated using a magnetic vector potential [30]. A module, which calculates this vector potential and the resulting eddy currents and demagnetizing field, could replace the current implementation of the hybrid finite element/boundary element method.

The ever increasing computing power and availability of large clusters of workstations and parallel machines will support these developments and allow even larger systems to be simulated. A challenging problem, for example, is the simulation of magnetic hard disk media including the read/write head and their interaction [139]. High-frequency magnetization reversal during the writing process should also include thermal and eddy current effects. All these aspects are very important for the design and development of per-

pendicular recording media, and the micromagnetic package developed for this thesis can be a starting point for such a comprehensive micromagnetic model.

Appendix A

Micromagnetics Packages

Commercial codes

- LLG Micromagnetics Simulator
  developed by M. R. Scheinfein
  `http://llgmicro.home.mindspring.com/`
  available for MS Windows (dual CPU supported)

- MagFEM3D
  developed by K. Ramstöck
  `http://www.ramstock.de/`
  available on Unix, MS Windows platforms

- Magsimus
  Euxine Technologies
  `http://www.euxine.com/`
  available for MS Windows platforms

- MicroMagus
  developed by D. V. Berkov, N. L. Gorn
  `http://www.micromagus.de/`
  available for MS Windows platforms

Free Open Source Codes

- PC Micromagnetic Simulator (SimulMag)
  developed by John Oti
  `http://math.nist.gov/oommf/contrib/simulmag/`
  available for MS Windows platforms

- General Dynamic Micromagnetics (GDM2)
  developed by Bo Yang
  `http://physics.ucsd.edu/∼drf/pub/`

- Object Oriented MicroMagnetic Framework (OOMMF)
  developed by Mike Donahue and Don Porter
  `http://math.nist.gov/oommf/`
  available on Unix, MS Windows platforms

Appendix B

Selected Software Packages

This is the list of software packages, which has been used in for the implementation of the finite element micromagnetics package. Along with the title and URLs are short citations from the websites, which summarize the contents and objective of each package.

- **PETSc**
  The Portable, Extensible Toolkit for Scientific Computation [58]
  PETSc is a suite of data structures and routines for the scalable (parallel) solution of scientific applications modeled by partial differential equations. It employs the MPI standard for all message-passing communication.

  `http://www-fp.mcs.anl.gov/petsc/`

- **BLAS, CBLAS**
  Basic Linear Algebra Subprograms [140, 141, 59]
  The BLAS are high quality "building block" routines for performing basic vector and matrix operations. Level 1 BLAS do vector-vector operations, Level 2 BLAS do matrix-vector operations, and Level 3 BLAS do matrix-matrix operations.

  `http://www.netlib.org/blas/`

- **LAPACK**
  Linear Algebra PACKage [60]
  LAPACK is written in Fortran77 and provides routines for solving systems of simultaneous linear equations, least-squares solutions of linear systems of equations, eigenvalue problems, and singular value problems.

  `http://www.netlib.org/lapack/`

- **LINPACK**
  LINear algebra PACKage [61]
  LINPACK is a collection of Fortran subroutines that analyze and solve linear equations and linear least-squares problems.

- **MPI, MPICH**
  The Message Passing Interface (MPI) standard [62]
  MPI is a library specification for message-passing, proposed as a standard by a broadly based committee of vendors, implementors, and users.

  `http://www-unix.mcs.anl.gov/mpi/`

  MPICH-A Portable Implementation of MPI [63]
  MPICH is a freely available, portable implementation of MPI, the Standard for message-passing libraries.

  `http://www-unix.mcs.anl.gov/mpi/mpich/`

- **Metis**
  Family of Multilevel Partitioning Algorithms [64]
  Metis is a family of programs for partitioning unstructured graphs and hypergraphs and computing fill-reducing orderings of sparse matrices. The underlying algorithms used by Metis are based on the state-of-the-art multilevel paradigm that has been shown to produce high quality results and scale to very large problems.

  `http://www-users.cs.umn.edu/∼karypis/metis/`

- **TAO**
  Toolkit for Advanced Optimization [46]
  The Toolkit for Advanced Optimization (TAO) is aimed at the solution of large-scale optimization problems on high-performance architectures. Our main goals are portability, performance, scalable parallelism, and an interface independent of the architecture.

  TAO is suitable for both single-processor and massively-parallel architectures. The current version of TAO has algorithms for unconstrained and bound-constrained optimization.

  `http://www-fp.mcs.anl.gov/tao/index.htm`

- **VODE**
  Scott D. Cohen and Alan C. Hindmarsh [142]

  Large non-stiff or stiff ordinary differential equation initial-value problem solver

`http://www.llnl.gov/CASC/people/hindmarsh/`

CVODE
Scott D. Cohen and Alan C. Hindmarsh,
"CVODE, a Stiff/Nonstiff ODE Solver in C" [51]
available from [143]

`http://www.netlib.org/`
`http://www.netlib.org/ode/cvode.tar.gz`

PVODE
PVODE is a portable solver for ordinary differential equation systems. It is based on robust mathematical algorithms, and targeted at large systems on parallel machines [48].

G. D. Byrne and A. C. Hindmarsh,
"PVODE, An ODE Solver for Parallel Computers" [49]

`http://www.llnl.gov/CASC/`
`http://www.llnl.gov/CASC/nsde/`
`http://www.llnl.gov/CASC/PVODE/`

- **zlib**
  A Massively Spiffy Yet Delicately Unobtrusive Compression Library
  zlib is designed to be a free, general-purpose, legally unencumbered – that is, not covered by any patents – lossless data-compression library for use on virtually any computer hardware and operating system [65].

  `http://www.gzip.org/zlib/`

- **libpng**
  libpng is the official PNG reference library [66].

  `http://www.libpng.org/pub/png/libpng.html`

Appendix C

Typical Material Parameters

In the following table a list of typical material parameters of magnetic materials is given in SI and cgs units, which have been (partly) used in the micromagnetic simulations of this thesis.

The symbols have the following meanings:

T	measurement temperature
Ms	saturation magnetization
Js	saturation polarization $(J_s = \mu_o M_s)$
Aexch	exchange constant
Kani1	first anisotropy constant K_1
Kani2	second anisotropy constant K_2
Hk	anisotropy field $H_k = \sqrt{2K_1/J_s}$
Tc	Curie temperature
E(Bloch)	domain wall energy of a Bloch wall $E_{\mathrm{Bloch}} = \pi\sqrt{AK_1}$
Lex(A,K)	Bloch exchange length $l_{\mathrm{bex}} = \sqrt{A/K_1}$
Lex(A,Ms)	Néel exchange length $l_{\mathrm{nex}} = \sqrt{2A/(\mu_0 M_s^2)}$

Material parameters

		SI units											cgs units						
	T	Ms	Js	Aexch	Kani1	Kani2	Hk	Tc	E(Bloch)	Lex(A,K)	Lex(A,Ms)	Ms	Js=4piMs	Aexch	Kani	Kani2	Hk	E(Bloch)
	K	A/m	T	J/m	J/m^3	J/m^3	A/m	K	J/m^2	nm	nm	G=emu/cm^3	G	erg/cm	erg/cm^3	erg/cm^3	Oe	erg/cm^2
alpha Fe (Kneller)		1,71E+06	2,15	2,50E-11	4,60E+04	1,50E+04	4,28E+04	1044	4,29E-03	23,31	3,69	1,71E+03	2,15E+04	2,50E-06	4,60E+05	1,50E+05	5,38E+02	
Co [15,16]		1,40E+06	1,76	1,30E-11	4,50E+05	1,50E+05	5,12E+05		9,67E-03	5,37	3,25	1,40E+03	1,76E+04	1,30E-06	4,50E+06	1,50E+06	6,43E+03	
Co [17]		1,40E+06	1,76	1,40E-11	5,00E+05		5,68E+05		1,06E-02	5,29	3,37	1,40E+03	1,76E+04	1,40E-06	5,00E+06		7,14E+03	
Ni [12]	0	5,10E+05	0,64									5,10E+02	6,41E+03					
Ni [13]	286	4,93E+05	0,62									4,93E+02	6,20E+03					
Nd2Fe14B (Emerge)		1,28E+06	1,61	1,25E-11	4,50E+06	6,60E+05	5,59E+06		3,00E-02	1,67	3,48	1,28E+03	1,61E+04	1,25E-06	4,50E+07	6,60E+06	7,02E+04	
Fe3B		1,29E+06	1,62	1,25E-11	3,22E+05		3,99E+05		8,02E-03	6,23	3,47	1,29E+03	1,62E+04	1,25E-06	3,22E+06		5,01E+03	
Sm2Co17 [14]	300	1,05E+06	1,32	1,40E-11	5,00E+06		7,58E+06	820	3,35E-02	1,67	4,49	1,05E+03	1,32E+04	1,40E-06	5,00E+07		9,52E+04	
SmCo5 [14]	300	6,37E+05	0,80	1,40E-11	1,90E+06		4,75E+06	720	2,06E-02	2,71	7,41	6,37E+02	8,00E+03	1,40E-06	1,90E+07		5,97E+04	
Sm2Co17 [18]	300	1,05E+06	1,32	1,40E-11	3,00E+06		4,55E+06	720	2,59E-02	2,16	4,49	1,05E+03	1,32E+04	1,40E-06	3,00E+07		5,71E+04	
SmCo5 [18]	300	1,05E+06	1,32	1,40E-11	1,50E+07		2,27E+07	720	5,80E-02	0,97	4,49	1,05E+03	1,32E+04	1,40E-06	1,50E+08		2,86E+05	
Ni80Fe20 (Permalloy) [11]		7,96E+05	1,00	1,30E-11							5,72	7,96E+02	1,00E+04	1,30E-06				
Klemmer, Weller data [19, 20]																		
CoPtCr		2,98E+05	0,37	9,99E-12	2,00E+05		1,07E+06	—	5,65E-03	7,07	13,38	2,98E+02	3,74E+03	9,99E-07	2,00E+06		1,34E+04	5,65
Co		1,40E+06	1,76	9,99E-12	4,50E+05		5,12E+05	1404	8,48E-03	4,71	2,85	1,40E+03	1,76E+04	9,99E-07	4,50E+06		6,43E+03	8,48
Co3Pt		1,10E+06	1,38	9,93E-12	2,00E+06		2,89E+06	—	1,78E-02	2,23	3,61	1,10E+03	1,38E+04	9,93E-07	2,00E+07		3,64E+04	17,83
FePd (L1_0)		1,10E+06	1,38	1,03E-11	1,80E+06		2,60E+06	760	1,72E-02	2,39	3,67	1,10E+03	1,38E+04	1,03E-06	1,80E+07		3,27E+04	17,19
FePt (L1_0) (K1_min)		1,14E+06	1,43	1,02E-11	6,60E+06		9,21E+06	750	3,28E-02	1,24	3,53	1,14E+03	1,43E+04	1,02E-06	6,60E+07		1,16E+05	32,77
FePt (L1_0) (K1_max)		1,14E+06	1,43	1,54E-11	1,00E+07		1,40E+07	750	4,97E-02	1,24	4,34	1,14E+03	1,43E+04	1,54E-06	1,00E+08		1,75E+05	49,66
CoPt (L1_0)		8,00E+05	1,01	1,01E-11	4,90E+06		9,75E+06	840	2,81E-02	1,43	5,00	8,00E+02	1,01E+04	1,01E-06	4,90E+07		1,23E+05	28,07
MnAl (L1_0)		5,60E+05	0,70	1,02E-11	1,70E+06		4,83E+06	650	1,67E-02	2,45	7,20	5,60E+02	7,04E+03	1,02E-06	1,70E+07		6,07E+04	16,67
Nd2Fe14B		1,27E+06	1,60	9,86E-12	4,60E+06		5,76E+06	585	2,69E-02	1,46	3,12	1,27E+03	1,60E+04	9,86E-07	4,60E+07		7,24E+04	26,94
SmCo5		9,10E+05	1,14	5,39E-12	1,10E+07		1,92E+07	1000	3,08E-02	0,70	3,22	9,10E+02	1,14E+04	5,39E-07	1,10E+08		2,42E+05	30,81
SmCo5		9,10E+05	1,14	1,82E-11	2,00E+07		3,50E+07	1000	7,64E-02	0,95	5,92	9,10E+02	1,14E+04	1,82E-06	2,00E+08		4,40E+05	76,39

References
[11] Fidler, JAP 91 (2002) 7974
[12] Kronmüller, Vorlesungsskriptum
[13] Landolt–Börnstein
[14] Durst, Phys. Stat. Sol. (a) 108 (1988) 403
[15] Yang, JAP 87 (2000) 6884
[16] Cullity, Introd. to Magn. Mat., Addison–Wesley 1972
[17] Buda, IEEE Trans. Magn. 37 (2001) 2061
[18] Tang, IEEE Trans. Magn. 37 (2001) 2515
[19] Klemmer, Script. Met. 33 no. 10/11 (1995) 1793–1805
[20] Weller, IEEE Trans. Magn. 36 (2000) 10–15

Table C.1: Table of material parameters of typical ferromagnets.

List of Figures

List of Tables

Bibliography

[1] K. J. Strnat, G. Hoffer, J. Oson, and W. Ostertag, "A family of cobalt-based permanent magnet materials," *J. Appl. Phys.*, vol. 38, pp. 1001–1002, 1967.

[2] D. Niarchos, R. Harris, D. Givord, C. Christodoulou, O. Gutfleisch, S. Kobe, M. Coey, J. Fidler, C. Tattam, M. Grönefeld, and G. Martinek, "HITEMAG - novel permanent magnets for high temperature applications." Project no. GRD1-1999-11125,
URL: `http://www.tcd.ie/Physics/Magnetism/Hitemag/`, 2000.

[3] M. Sagawa, S. Fujimura, N. Togawa, H. Yamamoto, and Y. Matsuura, "New material for permanent magnets on a base of nd and fe," *J. Appl. Phys.*, vol. 55, pp. 2083–2087, 1984.

[4] J. J. Croat, J. F. Herbst, R. W. Lee, and F. E. Pinkerton, "Pr-Fe and Nd-Fe-based materials: A new class of high-performance permanent magnets," *J. Appl. Phys.*, vol. 55, no. 6, pp. 2078–2082, 1984.

[5] G. C. Hadjipanayis, R. C. Hazelton, and K. R. Lawless, "Cobalt-free permanent magnet materials based on iron-rare-earth alloys," *J. Appl. Phys.*, vol. 55, no. 6, pp. 2073–2077, 1984.

[6] S. Sasaki, J. Fidler, and M. Sagawa, "High performance sintered magnets made by new RIP from SC alloys," in *Proc. XI. Int. Symp. on Magnetic Anisotropy and Coercivity in Rare Earth Transition Metal Alloys* (H. Kaneko, M. Homma, and M. Okada, eds.), pp. 109–118, The Japan Institute of Metals, 2000.

[7] R. Comerford, "Magnetic storage: The medium that wouldn't die," *IEEE Spectrum*, vol. 37, pp. 36–39, Dec. 2000.

[8] S. R. Das, "Coming soon: Terabit hard disk drives," *IEEE Spectrum*, vol. 40, pp. 19–21, Feb. 2003.

[9] C. H. Möller, O. Kronenwerth, D. Grundler, W. Hansen, C. Heyn, and D. Heitmann, "Extraordinary magnetoresistance effect in a microstructured metal–semiconductor hybrid structure," *Appl. Phys. Lett.*, vol. 80, no. 21, pp. 3988–3990, 2002.

[10] S. Tehrani, B. Engel, J. M. Slaughter, E. Chen, M. DeHerrera, M. Durlam, P. Naji, R. Whig, J. Janesky, , and J. Calder, "Recent developments in magnetic tunnel junction mram," *IEEE Trans. Magn.*, vol. 36, no. 5, pp. 2752–2757, 2000.

[11] J. Zhu, Y. Zheng, and G. A. Prinz, "Ultrahigh density vertical magnetoresistive random access memory," *J. Appl. Phys.*, vol. 87, pp. 6668–6673, May 2000.

[12] G. C. Hadjipanayis, W. Tang, Y. Zhang, S. T. Chui, J. F. Liu, C. Chen, and H. Kronmüller, "High temperature 2:17 magnets: Relationship of magnetic properties to microstructure and processing," *IEEE Trans. Magn.*, vol. 36, no. 5, pp. 3382–3387, 2000.

[13] J. Fidler and T. Schrefl, "Micromagnetic modelling - the current state of the art," *J. Phys. D: Appl. Phys.*, vol. 33, pp. R135–R156, 2000.

[14] T. R. Koehler and D. R. Fredkin, "Finite element methods for micromagnetics," *IEEE Trans. Magn.*, vol. 28, pp. 1239–1244, March 1992.

[15] J. Alberty, C. Carstensen, and S. A. Funken, "Remarks around 50 lines of MATLAB: Short finite element implementation," *Numerical Algorithms*, vol. 20, pp. 117–137, 1999.

[16] J. Bey, "Tetrahedral grid refinement," *Computing*, vol. 55, pp. 355–378, 1995.

[17] J. G. Zhu, "Micromagnetic modelling: theory and application in magnetic thin films," *MRS Bulletin*, vol. 20, pp. 49–54, 1995.

[18] P. G. Ciarlet, *The Finite Element Method for Elliptic Problems*. Amsterdam, New York, Oxford: North-Holland, 1978.

[19] M. Corporation, "MSC.Patran home page," 2002.
URL: `http://www.mscsoftware.com/support/prod_support/patran/`.

[20] R. Ribó, M. A. de Riera Pasenau, and E. Escolano, "GiD home page," 2002. International Center For Numerical Methods in Engineering (CIMNE),
URL: `http://gid.cimne.upc.es`.

[21] A. Hubert and R. Schäfer, *Magnetic Domains.* Berlin: Springer, 1998.

[22] V. D. Tsiantos, D. Suess, W. Scholz, T. Schrefl, and J. Fidler, "The effect of the cell size in langevin micromagnetic simulations," *J. Magn. Magn. Mater.*, vol. 242-245, pp. 999–1001, 2002.

[23] W. Rave, K. Ramstöck, and A. Hubert, "Corners and nucleation in micromagnetics," *J. Magn. Magn. Mater.*, vol. 183, pp. 329–333, 1998.

[24] C. Carstensen and F. Funken, "Coupling of nonconforming finite elements and boundary elements II: A posteriori estimates and adaptive mesh-refinement," *Computing*, vol. 62, no. 3, pp. 243–259, 1999.

[25] K. M. Tako, T. Schrefl, M. A. Wongsam, and R. W. Chantrell, "Finite element micromagnetic simulations with adaptive mesh refinement," *J. Appl. Phys.*, vol. 81, no. 8, pp. 4082–4084, 1997.

[26] R. Hertel and H. Kronmüller, "Adaptive finite element mesh refinement techniques in 3D micromagnetic modeling," *IEEE Trans. Magn.*, vol. 34, pp. 3922–3930, November 1998.

[27] W. Scholz, T. Schrefl, and J. Fidler, "Mesh refinement in FE-micromagnetics for multi-domain $Nd_2Fe_{14}B$ particles," *J. Magn. Magn. Mater.*, vol. 196-197, pp. 933–934, 1999.

[28] H. Forster, T. Schrefl, D. Suess, W. Scholz, V. Tsiantos, R. Dittrich, and J. Fidler, "Domain wall motion in nano-wires using moving grids," *J. Appl. Phys.*, vol. 91, pp. 6914–6919, 2002.

[29] H. Forster, *Reversal modes in mesoscopic structures.* Dissertation, TU Wien, 2003.

[30] A. Aharoni, "Magnetostatic energy calculation," *IEEE Trans. Magn.*, vol. 27, no. 4, pp. 3539–3547, 1991.

[31] Q. Chen and A. Konrad, "A review of finite element boundary techniqes for static and quasi-static electromagnetic field problems," *IEEE Trans. Magn.*, vol. 33, pp. 663–676, 1996.

[32] B. Streibl, "Dynamische mikromagnetische Simulation von μMAG Standardproblemen," Diplomarbeit, TU Wien, 1998.

[33] W. F. Brown, *Micromagnetics.* New York: Interscience, 1963.

[34] A. Aharoni, *Introduction to the Theory of Ferromagnetism.* Monographs on Physics, Oxford University Press, 1996.

[35] L. Berger, "Emission of spin waves by a magnetic multilayer traversed by a current," *Phys. Rev. B*, vol. 54, no. 13, pp. 9353–9358, 1996.

[36] S. Ingvarsson, L. Ritchie, X. Y. Liu, G. Xiao, J. C. Slonczewski, P. L. Trouilloud, , and R. H. Koch, "Role of electron scattering in the magnetization relaxation of thin $Ni_{81}Fe_{19}$ films," *Phys. Rev. B*, vol. 66, p. 214416, 2002.

[37] K. Capelle and B. L. Gyorffy, "Exploring dynamical magnetism with time-dependent density-functional theory: From spin fluctuations to gilbert damping," *Europhys. Lett.*, vol. 61, no. 3, pp. 354–360, 2003.

[38] T. Gilbert Armour Research Foundation, Report No. 11, 1955.

[39] T. L. Gilbert, "A Lagrangian formulation of gyromagnetic equation of the magnetization field," *Phys. Rev.*, vol. 100, p. 1243, 1955.

[40] C. W. Gardiner, *Handbook of stochastic methods: for physics, chemistry and the natural sciences.* Springer, 2nd ed., 1996.

[41] D. R. Fredkin and T. R. Koehler, "Hybrid method for computing demagnetizing fields," *IEEE Trans. Magn.*, vol. 26, no. 2, pp. 415–417, 1990.

[42] T. R. Koehler, "Hybrid FEM-BEM method for fast micromagnetic calculations," *Physica B: Condensed Matter*, vol. 233, no. 4, pp. 302–307, 1997.

[43] D. A. Lindholm, "Three-dimensional magnetostatic fields from point-matched integral equations with linearly varying scalar sources," *IEEE Trans. Magn.*, vol. MAG-20, pp. 2025–2032, September 1984.

[44] D. Süss, "Mikromagnetische Simulation der Keimbildung in SE Magneten," Diplomarbeit, TU Wien, 1999.

[45] D. Süss, T. Schrefl, and J. Fidler, "Micromagnetic simulation of high energy density permanent magnets," *IEEE Trans. Magn.*, vol. 36, no. 5, pp. 3282–3284, 2000.

[46] S. Benson, L. C. McInnes, J. J. Moré, and J. Sarich, "TAO home page," 2001.
URL: `http://www-unix.mcs.anl.gov/tao/`.

[47] S. Benson and J. J. Moré, "A limited memory variable metric method for bound constrained minimization," Tech. Rep. ANL-95/11 - Revision 2.1.3, Argonne National Laboratory, 2002.

[48] G. D. Byrne and A. C. Hindmarsh, "PVODE home page," 2002. URL: `http://www.llnl.gov/CASC/PVODE/`.

[49] G. D. Byrne and A. C. Hindmarsh, "PVODE, an ODE solver for parallel computers," *Int. J. High Perf. Comput. Appl.*, vol. 13, no. 4, pp. 354–365, 1999.

[50] S. D. Cohen and A. C. Hindmarsh, "CVODE user guide." Lawrence Livermore National Laboratory report UCRL-MA-118618, 1994.

[51] S. D. Cohen and A. C. Hindmarsh, "CVODE, a Stiff/Nonstiff ODE Solver in C," *Computers in Physics*, vol. 10, no. 2, pp. 138–143, 1996.

[52] P. N. Brown and A. C. Hindmarsh, "Reduced storage matrix methods in stiff ODE systems," *J. Appl. Math. and Comp.*, vol. 31, pp. 40–91, 1989.

[53] D. Suess, V. Tsiantos, T. Schrefl, J. Fidler, W. Scholz, H. Forster, R. Dittrich, and J. J. Miles, "Time resolved micromagnetics using a preconditioned finite element method," *J. Magn. Magn. Mater.*, vol. 248, pp. 298–311, 2002.

[54] A. C. Hindmarsh and L. R. Petzold, "Algorithms and software for ordinary differential equations and differential-algebraic equations," *Computers in Physics*, vol. 9, pp. 34–41, 148–155, 1995.

[55] G. Henkelman and H. Jónsson, "Improved tangent estimate in the nudged elastic band method for finding minimum energy paths and saddle points," *J. Chem. Phys.*, vol. 113, pp. 9978–9985, 2000.

[56] R. Dittrich, T. Schrefl, D. Suess, W. Scholz, H. Forster, and J. Fidler, "A path method for finding energy barriers and minimum energy paths in complex micromagnetic systems," *J. Magn. Magn. Mater.*, vol. 250, pp. 12–19, 2002.

[57] R. Dittrich. Dissertation, TU Wien, 2003.

[58] S. Balay, K. Buschelman, W. D. Gropp, D. Kaushik, M. Knepley, L. C. McInnes, B. F. Smith, and H. Zhang, "PETSc home page," 2001. URL: `http://www.mcs.anl.gov/petsc`.

[59] J. Dongarra, "BLAS," 2002.
URL: `http://www.netlib.org/blas/`.

[60] E. Anderson, Z. Bai, C. Bischof, S. Blackford, J. Demmel, J. Dongarra, J. Du Croz, A. Greenbaum, S. Hammarling, A. McKenney, and D. Sorensen, "LAPACK," 2002.
URL: `http://www.netlib.org/lapack/`.

[61] J. Dongarra, J. Bunch, C. Moler, and P. Stewart, "LINPACK," 2002.
URL: `http://www.netlib.org/linpack/`.

[62] M. committee, "MPI home page," 2002.
URL: `http://www-unix.mcs.anl.gov/mpi/`.

[63] W. Gropp and E. Lusk, "MPICH home page," 2002.
URL: `http://www-unix.mcs.anl.gov/mpi/mpich/`.

[64] G. Karypis, "METIS home page," 2002.
URL: `http://www-users.cs.umn.edu/∼karypis/metis/`.

[65] J. Gailly and M. Adler, "zlib home page," 2002.
URL: `http://www.gzip.org/zlib/`.

[66] G. Randers-Pehrson, "libpng home page," 2002.
URL: `http://www.libpng.org/pub/png/libpng.html`.

[67] G. Karypis and V. Kumar, "Multilevel k-way partitioning scheme for irregular graphs," *Journal of Parallel and Distributed Computing*, vol. 48, no. 1, pp. 96–129, 1998.

[68] *Multilevel algorithms for multi-constraint graph partitioning*, IEEE Computer Society Press, 1998.

[69] J. G. Lewis, "Implementation of the gibbs-poole-stockmeyer and gibbs-king algorithms," *ACM Transactions on Mathematical Software*, vol. 8, no. 2, pp. 180–189, 1982.

[70] P. Bastian, "Load balancing for adaptive multigrid methods," *SIAM Journal on Scientific Computing*, vol. 19, no. 4, pp. 1303–1321, 1998.

[71] P. Bastian, K. Birken, K. Johannsen, S. Lang, N. Neuss, H. Rentz-Reichert, and C. Wieners, "UG home page," 2003.
URL: `http://cox.iwr.uni-heidelberg.de/∼ug/`.

[72] P. Bastian, K. Birken, K. Johannsen, S. Lang, N. Neuss, H. Rentz-Reichert, and C. Wieners, "UG - A flexible software toolbox for solving partial differential equations," *Computing and Visualization in Science*, vol. 1, pp. 27–40, 1997.

[73] K. Birken, "DDD home page," 1997.
URL: `http://cox.iwr.uni-heidelberg.de/~ddd/`.

[74] E. P. Mücke, I. A. Saias, and B. Zhu, "Fast randomized point location without preprocessing in two- and three-dimensional delaunay triangulations," *Computational Geometry*, vol. 12, pp. 63–83, 1999.

[75] Advanced Visual Systems, "UCD file format," 2002.
URL: `http://help.avs.com/Express/doc/help/reference/dvmac/UCD_Form.htm`.

[76] Advanced Visual Systems, "AVS home page," 2002.
URL: `http://www.avs.com`.

[77] Kubota Graphics Technologies Inc., "MicroAVS home page," 2002.
URL: `http://www.kgt.co.jp/index_e.html`.

[78] G. Haase, *Parallelisierung numerischer Algorithmen für partielle Differentialgleichungen*. Stuttgart, Leipzig: Teubner, 1999.

[79] W. Scholz, T. Schrefl, and J. Fidler, "Aufbau eines geschützten Subnetzes im TUNET," *ZIDline, Informationen des zentralen Informatikdienstes der TU Wien*, pp. 29–37, June 2001.

[80] K.-D. Durst, H. Kronmüller, and W. Ervens, "Investigations of the magnetic properties and demagnetization processes of an extremely high coercive $Sm(Co,Cu,Fe,Zr)_{7.6}$ permanent magnet I. Determination of intrinsic magnetic material parameters," *phys. stat. sol. (a)*, vol. 108, pp. 403–416, 1988.

[81] K. J. Strnat, "Rare earth-cobalt permanent magnets," in *Ferromagnetic Materials* (E. P. Wohlfarth and K. H. J. Buschow, eds.), vol. 4, pp. 131–209, North-Holland, 1988.

[82] K. D. Durst and H. Kronmüller, "Magnetic hardening mechanisms in sintered Nd-Fe-B and $Sm(Co,Cu,Fe,Zr)_{7.6}$ permanent magnets," in *Proceedings of the Eighth International Workshop on Rare-Earth Magnets and their Applications and the Fourth International Symposium on Magnetic Anisotropy and Coercivity in Rare Earth-Transition Metal*

Alloys (K. J. Strnat, ed.), pp. 725–735, Univ. Dayton, Dayton, OH, USA, 1985.

[83] H. Kronmüller, "Nucleation and propagation of reversed domain in RE-Co-magnets," in *Proceedings of the 6th International Workshop on Rare Eart-Cobalt Permanent Magnets and their Applications and 3rd International Symposium on Magnetic Anisotropy and Coercivity in Rare Earth-Transition Metal Alloys* (J. Fidler, ed.), pp. 555–565, Tech. Univ. Vienna, Vienna, Austria, 1985.

[84] J. D. Livingston and D. L. Martin, "Microstructure of aged $(Co,Cu,Fe)_7Sm$ magnets," *J. Appl. Phys.*, vol. 48, pp. 1350–1354, 1977.

[85] R. K. Mishra, G. Thomas, T. Yoneyama, A. Fukuno, and T. Ojima, "Microstructure and properties of step aged rare earth alloy magnets," *J. Appl. Phys.*, vol. 52, pp. 2517–2519, 1981.

[86] J. Fidler and P. Skalicky, "Microstructure of precipitation hardened cobalt rare earth permanent magnets," *J. Magn. Magn. Mater.*, vol. 27, pp. 127–134, 1982.

[87] J. Fidler, "Coercivity of precipitation hardened cobalt rare earth 17:2 permanent magnets," *J. Magn. Magn. Mater.*, vol. 30, pp. 58–70, 1982.

[88] W. Tang, Y. Zhang, A. M. Gabay, M. F. de Campos, and G. C. Hadjipanayis, "Anomalous temperature dependence of coercivity in rare earth cobalt magnets," *J. Magn. Magn. Mater.*, vol. 242-245, pp. 1335–1337, 2002.

[89] T. Matthias, J. Fidler, G. Zehetner, T. Schrefl, D. Schobinger, and G. Martinek, "TEM-analysis of $Sm(Co,Fe,Cu,Zr)_z$ magnets for high temperature applications," *J. Magn. Magn. Mater.*, vol. 242-245, pp. 1353–1355, 2002.

[90] T. Schrefl, *Numerical Simulation of Magnetization Reversal Processes in Hard Magnetic Materials.* Dissertation, TU Wien, 1993.

[91] H. Kronmüller and D. Goll, "Micromagnetic theory of the pinning of domain walls at phase boundaries," *Physica B: Condensed Matter*, vol. 319, pp. 122–126, 2002.

[92] E. D. Torre and C. M. Perlov, "A one-dimensional model for wall motion coercivity in magneto-optic media," *J. Appl. Phys.*, vol. 69, pp. 4596–4598, April 1991.

[93] W. Tang, A. M. Gabay, Y. Zhang, G. C. Hadjipanayis, and H. Kronmüller, "Temperature dependence of coercivity and magnetization reversal mechanism in $Sm(Co_{bal}Fe_{0.1}Cu_yZr_{0.04})_{7.0}$ magnets," *IEEE Trans. Magn.*, vol. 37, pp. 2515–2517, 2001.

[94] E. Lectard, C. H. Allibert, and R. Ballou, "Saturation magnetization and anisotropy fields in the $Sm(Co_{1-x}Cu_x)_5$," *J. Appl. Phys.*, vol. 75, pp. 6277–6279, May 1994.

[95] A. Aharoni, "Domain wall pinning at planar defects," *J. Appl. Phys.*, vol. 58, pp. 2677–2680, October 1985.

[96] B. Streibl, J. Fidler, and T. Schrefl, "Domain wall pinning in high temperature $Sm(Co,Fe,Cu,Zr)_{7-8}$ magnets," *J. Appl. Phys.*, vol. 87, no. 9, pp. 4765–4767, 2000.

[97] E. Estevez-Rams, *TEM study of the correlation between microstructure and magnetic properties of novel hard and soft magnetic materials.* Dissertation, TU Wien, 1996.

[98] R. Skomski, "Domain-wall curvature and coercivity in pinning type Sm-Co magnets," *J. Appl. Phys.*, vol. 81, pp. 5627–5629, April 1997.

[99] D. Weller, A. Moser, L. Folks, M. E. Best, W. Lee, M. F. Toney, M. Schwickert, J.-U. Thiele, and M. F. Doerner, "High K_u materials approach to 100 Gbits/in^2," *IEEE Trans. Magn.*, vol. 36, pp. 10–15, 2000.

[100] T. Shima, K. Takanashi, Y. K. Takahashi, and K. Hono, "Preparation and magnetic properties of highly coercive FePt films," *Appl. Phys. Lett.*, vol. 81, pp. 1050–1052, 2002.

[101] B. Bian, D. E. Laughlin, K. Sato, and Y. Hirotsu, "Fabrication and nanostructure of oriented FePt particles," *J. Appl. Phys.*, vol. 87, pp. 6962–6964, 2000.

[102] T. Klemmer, D. Hoydick, H. Okumura, B. Zhang, and W. A. Soffa, "Magnetic hardening and coercivity mechanisms in $L1_0$ ordered FePd ferromagnets," *Scripta Metallurgica et Materialia*, vol. 33, no. 10/11, pp. 1793–1805, 1995.

[103] P. Candeloro, A. Gerardino, E. Di Fabrizio, S. Cabrini, G. Giannini, L. Mastrogiacomo, M. Ciria, R. C. O'Handley, G. Gubbiotti, and G. Carlotti, "Patterned magnetic permally nickel films: Fabrication

by electron beam and x-ray lithographic techniques," *Jpn. J. Appl. Phys.*, vol. 41, pp. 5149–5152, August 2002.

[104] C. A. Ross, "Patterned magnetic recording media," *Annu. Rev. Mater. Res.*, vol. 31, pp. 203–235, 2000.

[105] C. A. Ross, M. Hwang, M. Shima, J. Y. Cheng, M. Farhoud, T. A. Savas, H. I. Smith, W. Schwarzacher, F. M. Ross, M. Redjdal, and F. B. Humphrey, "Micromagnetic behavior of electrodeposited cylinder arrays," *Phys. Rev. B*, vol. 65, p. 144417, 2002.

[106] R. P. Cowburn, "Property variation with shape in magnetic nanoelements," *J. Phys. D: Appl. Phys.*, vol. 33, pp. R1–R16, 2000.

[107] T. Shinjo, T. Okuno, R. Hassdorf, K. Shigeto, and T. Ono, "Magnetic vortex core observation in circular dots of permalloy," *Science*, vol. 289, pp. 930–932, 2000.

[108] A. Wachowiak, J. Wiebe, M. Bode, O. Pietzsch, M. Morgenstern, and R. Wiesendanger, "Direct observation of internal spin structure of magnetic vortex cores," *Science*, vol. 298, pp. 577–580, 2002.

[109] M. Schneider, H. Hoffmann, and J. Zweck, "Magnetization reversal of thin submicron elliptical permalloy elements," *J. Magn. Magn. Mater.*, vol. 257, pp. 1–10, 2003.

[110] R. P. Cowburn, D. K. Koltsov, A. O. Adeyeye, M. E. Welland, and D. M. Tricker, "Single-domain circular nanomagnets," *Phys. Rev. Lett.*, vol. 83, pp. 1042–1045, August 1999.

[111] G. Gubbiotti, G. Carlotti, F. Nizzoli, R. Zivieri, T. Okuna, and T. Shinjo, "Magnetic properties of submicron circular permalloy dots," *IEEE Trans. Magn.*, vol. 38, pp. 2532–2534, September 2002.

[112] V. Novosad, M. Grimsditch, K. Y. Guslienko, P. Vavassori, Y. Otani, and S. D. Bader, "Spin excitations of magnetic vortices in ferromagnetic nanodots," *Phys. Rev. B*, vol. 66, p. 052407, 2002.

[113] N. A. Usov and S. E. Peschany, "Magnetization curling in a fine cylindrical particle," *J. Magn. Magn. Mater.*, vol. 118, pp. L290–L294, 1993.

[114] N. A. Usov and S. E. Peschany *Fiz. Met. Metalloved (transl.: The Physics of Metals and Metallography)*, vol. 12, pp. 13–24, 1994.

[115] T. M. Hengstmann, D. Grundler, C. Heyn, and D. Heitmann, "Stray-field investigation in permalloy nanodisks," *J. Appl. Phys.*, vol. 90, pp. 6542–6544, December 2001.

[116] K. Y. Guslienko, V. Novosad, Y. Otani, H. Shima, and K. Fukamichi, "Field evolution of magnetic vortex state in ferromagnetic disks," *Appl. Phys. Lett.*, vol. 78, pp. 3848–3850, June 2001.

[117] K. Y. Guslienko, V. Novosad, Y. Otani, H. Shima, and K. Fukamichi, "Magnetization reversal due to vortex nucleation, displacement, and annihilation in submicron ferromagnetic dot arrays," *Phys. Rev. B*, vol. 65, p. 024414, 2002.

[118] M. Schneider, H. Hoffmann, and J. Zweck, "Lorentz microscopy of circular ferromagnetic permalloy nanodisks," *Appl. Phys. Lett.*, vol. 77, pp. 2909–2911, October 2000.

[119] A. Fernandez and C. J. Cerjan, "Nucleation and annihilation of magnetic vortices in submicron-scale Co dots," *J. Appl. Phys.*, vol. 87, pp. 1395–1401, February 2000.

[120] V. Novosad, K. Y. Guslienko, H. Shima, Y. Otani, K. Fukamichi, N. Kikuchi, O. Kitakami, and Y. Shimada, "Nucleation and annihilation of magnetic vortices in sub-micron permalloy dots," *IEEE Trans. Magn.*, vol. 37, no. 4, pp. 2088–2090, 2001.

[121] A. Aharoni, "Upper bound to a single-domain behavior of a ferromagnetic cylinder," *J. Appl. Phys.*, vol. 68, pp. 2892–2900, September 1990.

[122] K. L. Metlov and K. Y. Guslienko, "Stability of magnetic vortex in soft magnetic nano-sized circular cylinder," *J. Magn. Magn. Mater.*, vol. 242-245, pp. 1015–1017, 2002.

[123] J. d'Albuquerque e Castro, D. Altbir, J. C. Retamal, and P. Vargas, "Scaling approach to the magnetic phase diagram of nanosized systems," *Phys. Rev. Lett.*, vol. 88, p. 237202, May 2002.

[124] M. Hehn, K. Ounadjela, J.-P. Bucher, F. Rousseaux, D. Decanini, B. Bartenlian, and C. Chappert, "Nanoscale magnetic domains in mesoscopic magnets," *Science*, vol. 272, pp. 1782–1785, 1996.

[125] G. A. Prinz, "Magnetoelectronics," *Science*, vol. 282, pp. 1660–1663, 1998.

[126] A. Lyberatos, G. Ju, R. J. M. van de Veerdonk, and D. Weller, "Micromagnetic study of subnanosecond magnetic switching in perpendicular multilayers," *J. Appl. Phys.*, vol. 91, pp. 2236–2242, February 2002.

[127] O. Chubykalo, J. D. Hannay, M. Wongsam, R. W. Chantrell, and J. M. Gonzalez, "Langevin dynamic simulation of spin waves in a micromagnetic model," *Phys. Rev. B*, vol. 65, p. 184428, 2002.

[128] W. K. Hiebert, A. Stankiewicz, and M. R. Freeman, "Direct observation of magnetic relaxation in a small permalloy disk by time-resolved scanning Kerr microscopy," *Phys. Rev. Lett.*, vol. 79, pp. 1134–1137, August 1997.

[129] Y. Acremann, C. H. Back, M. Buess, O. Portmann, A. Vaterlaus, D. Pescia, and H. Melchior, "Imaging precessional motion of the magnetization vector," *Science*, vol. 290, pp. 492–495, October 2000.

[130] K. Y. Guslienko, B. A. Ivanov, V. Novosad, Y. Otani, H. Shima, and K. Fukamichi, "Eigenfrequencies of vortex state excitations in magnetic submicron-size disks," *J. Appl. Phys.*, vol. 91, pp. 8037–8039, May 2002.

[131] K. Y. Guslienko and A. N. Slavin, "Spin-waves in cylindrical magnetic dot arrays with in-plane magnetization," *J. Appl. Phys.*, vol. 87, pp. 6337–6339, May 2000.

[132] J. P. Park, P. Eames, D. M. Engebretson, J. Berezovsky, and P. A. Crowell, "Imaging of spin dynamics in closure domain and vortex structures," *Phys. Rev. B*, vol. 67, p. 020403R, 2003.

[133] W. H. Press, S. A. Teukolsky, W. T. Vetterling, and B. P. Flannery, *Numerical Recipes in Fortran 77: The Art of Scientific Computing.* Cambridge University Press, 1997.

[134] K. J. Kirk, J. N. Chapman, and C. D. W. Wilkinson, "Lorentz microscopy of small magnetic structures," *J. Appl. Phys.*, vol. 85, pp. 5237–5242, April 1999.

[135] D. Süss, T. Schrefl, J. Fidler, and J. N. Chapman, "Micromagnetic simulation of the long range interaction between NiFe nano-elements using the BE-method," *J. Magn. Magn. Mater.*, vol. 196-197, pp. 617–619, 1999.

[136] Y. B. Xu, C. A. F. Vaz, A. Hirohata, C. C. Yao, W. Y. Lee, J. A. C. Bland, F. Rousseaux, E. Cambril, and H. Launois, "Domain wall trapping probed by magnetoresistance and magnetic force microscopy in submicron ferromagnetic wire structures," *J. Appl. Phys.*, vol. 85, pp. 6178–6180, April 1999.

[137] U. Ruediger, J. Yu, S. Zhang, A. D. Kent, and S. S. P. Parkin, "Negative domain wall contribution to the resistivity of microfabricated Fe wires," *Phys. Rev. Lett.*, vol. 80, pp. 5639–5642, June 1998.

[138] V. Tsiantos, T. Schrefl, W. Scholz, H. Forster, D. Suess, R. Dittrich, and J. Fidler, "Thermal fluctuations in magnetic sensor elements," *J. Sensors and Actuators.* in press.

[139] S. Batra, M. Covington, T. M. Crawford, B. Crue, P. A. A. van der Heijden, J. Jayashankar, E. C. Johns, M. Kryder, K. Minor, R. Rottmayer, U. Tran, and J. West, "A perpendicular write head design for high-density recording," *IEEE Trans. Magn.*, vol. 38, pp. 157–162, January 2002.

[140] J. J. Dongarra, J. D. Croz, S. Hammarling, and R. J. Hanson, "An extended set of FORTRAN Basic Linear Algebra Subprograms," *ACM Transactions on Mathematical Software*, vol. 14, pp. 1–17, Mar. 1988. See also [144].

[141] C. L. Lawson, R. J. Hanson, D. R. Kincaid, and F. T. Krogh, "Basic Linear Algebra Subprograms for Fortran usage," *ACM Transactions on Mathematical Software*, vol. 5, pp. 308–323, Sept. 1979.

[142] A. C. Hindmarsh, "Alan Hindmarsh's home page," 2002. URL: `http://www.llnl.gov/CASC/people/hindmarsh/`.

[143] S. D. Cohen and A. C. Hindmarsh, "CVODE page at `netlib`," 2002. URL: `http://www.netlib.org/ode/cvode.tar.gz`.

[144] J. J. Dongarra, J. D. Croz, S. Hammarling, and R. J. Hanson, "Corrigenda: "An extended set of FORTRAN Basic Linear Algebra Subprograms"," *ACM Transactions on Mathematical Software*, vol. 14, pp. 399–399, Dec. 1988. See [140].

Talks

[1] W. Scholz, "Adaptive mesh micromagnetics of RE hard magnets." Talk, 1999. HMM'99, International Symposium on Hysteresis and Micromagnetic Modeling, June 7-9, 1999, Perugia, Italy.

[2] W. Scholz, H. Forster, J. Fidler, and T. Schrefl, "Micromagnetic simulation of domain wall pinning and domain wall motion." Talk, paper: Comp. Mat. Sci. 25 (2002) 540-546, 2001. COST P3 Action Conference: Simulation of Physical Phenomena in Technological Applications, September 24-26, 2001, Madrid, Spain.

[3] W. Scholz, D. Suess, T. Schrefl, and J. Fidler, "Domain structures and domain wall pinning in arrays of elliptical NiFe nanoelements." Talk, paper: J. Appl. Phys. 91 (2002) 7047-7049, 2001. MMM'01 conference, November 12-16, 2001, Seattle, WA, USA.

[4] W. Scholz, J. Fidler, T. Schrefl, D. Suess, and T. Matthias, "Micromagnetic 3D simulation of the pinning field in high temperature $Sm(Co,Fe,Cu,Zr)_z$ magnets." Talk, paper: J. Appl. Phys. 91 (2002) 8492-8494, 2001. MMM'01 conference, November 12-16, 2001, Seattle, WA, USA.

[5] W. Scholz, "High performance linux clusters - design / configuration / maintenance." Talk, 2002. Seagate Research, Pittsburgh, PA, USA, 03.01.02.

[6] W. Scholz, K. Y. Guslienko, V. Novosad, D. Suess, T. Schrefl, R. W. Chantrell, and J. Fidler, "Transition from single-domain to vortex state in soft magnetic cylindrical nanodots." Talk, paper: J. Magn. Magn. Mater. (2003), submitted, 2002. ICFPM 2002, 4th International Conference on Fine Particle Magnetism, August 14-16, 2002, Pittsburgh, PA, USA.

Posters

[1] W. Scholz, T. Schrefl, and J. Fidler, "Mesh refinement in FE-micromagnetics for multi-domain $Nd_2Fe_{14}B$ particles." Poster, paper: J. Magn. Magn. Mater. 196-197 (1999) 933-934, 1998. EMMA'98 conference, September 9-12, 1998, Zargoza, Spain.

[2] D. Suess, H. Forster, W. Scholz, R. Dittrich, V. Tsiantos, T. Schrefl, and J. Fidler, "Numerical methods in micromagnetic simulations." Poster, 2001. Joint Summer Workshop 2001, June 30 - July 5, 2001, Santorini, Greece.

[3] R. Dittrich, W. Scholz, T. Schrefl, J. Fidler, D. Suess, H. Forster, and V. Tsiantos, "Thermal activation in micromagnetics." Poster, 2001. Joint Summer Workshop 2001, June 30 - July 5, 2001, Santorini, Greece.

[4] W. Scholz, J. Fidler, T. Schrefl, and D. Suess, "Micromagnetic simulation of domain wall pinning in $Sm(Co,Fe,Cu,Zr)_z$ magnets." Poster, paper: J. Magn. Magn. Mater. 242-245 (2002) 1356-1358, 2001. JEMS'01 conference, August 28 - September 1, 2001, Grenoble, France.

[5] D. Suess, W. Scholz, T. Schrefl, and J. Fidler, "Fast switching of small magnetic particles." Poster, paper: J. Magn. Magn. Mater. 242-245 (2002) 426-429, 2001. JEMS'01 conference, August 28 - September 1, 2001, Grenoble, France.

[6] T. Matthias, G. Zehetner, J. Fidler, W. Scholz, T. Schrefl, D. Schobinger, and G. Martinek, "TEM-analysis of $Sm(Co,Fe,Cu,Zr)_z$ magnets for high temperature applications." Poster, paper: J. Magn. Magn. Mater. 242-245 (2002) 1353-1355, 2001. JEMS'01 conference, August 28 - September 1, 2001, Grenoble, France.

[7] J. Fidler, T. Schrefl, V. Tsiantos, and W. Scholz, "Ultrafast switching of magnetic elements using a rotating field." Poster, paper: J. Appl. Phys. 91 (2002) 7974-7976, 2001. MMM'01 conference, November 12-16, 2001, Seattle, WA, USA.

[8] D. Suess, V. Tsiantos, T. Schrefl, W. Scholz, and J. Fidler, "Nucle-ation in polycrystalline thin films using a preconditioned finite element method." Poster, paper: J. Appl. Phys. 91 (2002) 7977-7979, 2001. MMM'01 conference, November 12-16, 2001, Seattle, WA, USA.

[9] T. Matthias, J. Fidler, W. Scholz, T. S. Rong, I. P. Jones, I. R. Harris, D. Schobinger, and G. Martinek, "TEM study of (Cu,Zr)-enriched SmCo 2:17 magnets used for high temperature applications." Poster, 2001. MMM'01 conference, November 12-16, 2001, Seattle, WA, USA.

[10] J. Fidler, T. Schrefl, W. Scholz, R. Dittrich, H. Forster, and D. Suess, "FE-simulation of fast switching behavior of magnetic nanoelements." Poster, paper: Proceedings, Eds: M. Laudon and B. Romanowicz, 2002, pp. 348-351, 2002. 5th Int. Conference on Modeling and Simulation of Microsystems, April 22-25, 2002, Puerto Rico.

[11] R. Dittrich, T. Schrefl, H. Forster, D. Suess, W. Scholz, J. Fidler, and V. Tsiantos, "Finite element simulation of discrete media with granu-lar structure." Poster, paper: IEEE Trans Magn. 38 (2002) 1967-1969, 2002. Intermag Europe 2002, April 28 - May 2, 2002, Amsterdam, Netherlands.

[12] J. Fidler, T. Schrefl, V. D. Tsiantos, H. Forster, D. Suess, W. Scholz, and R. Dittrich, "FE-simulation of fast switching behavior of granular nanoelements." Poster, paper: IEEE Trans Magn. 38 (2002) 2520-2522, 2002. Intermag Europe 2002, April 28 - May 2, 2002, Amsterdam, Netherlands.

[13] J. Fidler, T. Matthias, W. Scholz, T. Schrefl, T. S. Rong, I. Jones, and I. R. Harris, "The role of the precipitation structure on the coerciv-ity of $Sm(Co,Fe,Cu,Zr)_z$ magnets for ht applications." Poster, paper: Proceedings, ed: G. Hadjipanayis and M. J. Bonder, 2002, pp. 853-860, 2002. XVII Rare Earth Magnets Workshop, August 18-22, 2002, Newark, Delaware, USA.

[14] J. Fidler, T. Schrefl, P. E. Wigen, W. Scholz, and D. Suess, "Excitation of spin waves in square nanoelements by rotating field." Poster, paper: J. Appl. Phys. (2003), submitted, 2002. MMM'02 conference, November 11-15, 2002, Tampa, FL, USA.

Publications

[1] T. Schrefl, J. Fidler, R. Dittrich, D. Suess, W. Scholz, V. Tsiantos, and H. Forster, "Fast switching of mesoscopic magnets," in *Spin Dynamics in Confined Magnetic Structures II* (B. Hillebrands and K. Ounadjela, eds.), 2003. in press.

[2] W. Scholz, K. Y. Guslienko, V. Novosad, D. Suess, T. Schrefl, R. W. Chantrell, and J. Fidler, "Transition from single-domain to vortex state in soft magnetic cylindrical nanodots," *J. Magn. Magn. Mater.*, 2003. in press.

[3] V. Tsiantos, T. Schrefl, W. Scholz, H. Forster, D. Suess, R. Dittrich, and J. Fidler, "Thermal fluctuations in magnetic sensor elements," *J. Sensors and Actuators.* in press.

[4] H. Forster, T. Schrefl, R. Dittrich, W. Scholz, and J. Fidler, "Fast boundary methods for magnetostatic interactions in micromagnetics," *IEEE Trans. Magn.* submitted.

[5] D. Suess, T. Schrefl, W. Scholz, and J. Fidler, "Micromagnetic calculation of coercivity and remanence of self assembled FePt nanoparticle arrays," *J. Appl. Phys.* in press.

[6] R. Dittrich, T. Schrefl, D. Suess, W. Scholz, H. Forster, and J. Fidler, "Thermally induced magnetization reversal in AFC media," *J. Appl. Phys.* in press.

[7] V. Tsiantos, T. Schrefl, W. Scholz, and J. Fidler, "Thermal magnetization noise in submicron spin valve sensors," *J. Appl. Phys.* in press.

[8] D. Suess, M. Kirschner, T. Schrefl, W. Scholz, R. Dittrich, H. Forster, and J. Fidler, "Micromagnetic calculations of bias field and coercivity of compensated ferromagnetic/antiferromagnetic bilayers," *J. Appl. Phys.* in press.

[9] R. Dittrich, T. Schrefl, V. Tsiantos, H. Forster, D. Suess, W. Scholz, and J. Fidler, "Micromagnetic simulation of thermal effects in magnetic nanostructures," in *Magnetoelectronics and Magnetic Materials – Novel Phenomena and Advanced Characterization* (S. Zhang, W. Kuch, G. Guentherodt, C. Broholm, A. Kent, M. R. Fitzsimmons, I. Schuller, J. B. Kortright, T. Shinjo, and Y. Zhu, eds.), The Materials Research Society, 2003. in press.

[10] D. Suess, T. Schrefl, W. Scholz, and J. Fidler, "Fast switching of small magnetic particles," *J. Magn. Magn. Mater.*, vol. 242-245, pp. 426–429, 2002.

[11] V. D. Tsiantos, W. Scholz, D. Suess, T. Schrefl, and J. Fidler, "The effect of the cell size in langevin micromagnetic simulations," *J. Magn. Magn. Mater.*, vol. 242-245, pp. 999–1001, 2002.

[12] T. Matthias, G. Zehetner, J. Fidler, W. Scholz, T. Schrefl, D. Schobinger, and G. Martinek, "TEM-analysis of $Sm(Co,Fe,Cu,Zr)_z$ magnets for high temperature applications," *J. Magn. Magn. Mater.*, vol. 242-245, pp. 1353–1355, 2002.

[13] W. Scholz, J. Fidler, T. Schrefl, D. Suess, and T. Matthias, "Micromagnetic simulation of domain wall pinning in $Sm(Co,Fe,Cu,Zr)_z$ magnets," *J. Magn. Magn. Mater.*, vol. 242-245, pp. 1356–1358, 2002.

[14] J. Fidler, T. Schrefl, V. D. Tsiantos, W. Scholz, and D. Suess, "Micromagnetic simulation of the magnetic switching behaviour of mesoscopic and nanoscopic structures," *Comp. Mat. Sci.*, vol. 24, pp. 163–174, 2002.

[15] R. Grössinger, M. Küpferling, P. Kasperkovitz, A. Wimmer, M. Taraba, W. Scholz, J. Dudding, P. Leithuillier, J. C. Toussaint, B. Enzberg-Mahlke, W. Fernengel, and G. Reyne, "Eddy currents in pulsed field measurements," *J. Magn. Magn. Mater.*, vol. 242-245, pp. 911–914, 2002.

[16] W. Scholz, D. Suess, T. Schrefl, and J. Fidler, "Domain structures and domain wall pinning in arrays of elliptical nife nanoelements," *J. Appl. Phys.*, vol. 91, pp. 7047–7049, 2002.

[17] W. Scholz, J. Fidler, T. Schrefl, D. Suess, and T. Matthias, "Micromagnetic 3d simulation of the pinning field in high temperature $Sm(Co,Fe,Cu,Zr)_z$ magnets," *J. Appl. Phys.*, vol. 91, pp. 8492–8494, 2002.

[18] H. Forster, T. Schrefl, D. Suess, W. Scholz, V. Tsiantos, R. Dittrich, and J. Fidler, "Domain wall motion in nano-wires using moving grids," *J. Appl. Phys.*, vol. 91, pp. 6914–6919, 2002.

[19] J. Fidler, T. Schrefl, V. D. Tsiantos, W. Scholz, D. Suess, and H. Forster, "Ultrafast switching of magnetic elements using a rotating field," *J. Appl. Phys.*, vol. 91, pp. 7974–7976, 2002.

[20] D. Suess, V. Tsiantos, T. Schrefl, W. Scholz, and J. Fidler, "Nucleation in polycrystalline thin films using a preconditioned finite element method," *J. Appl. Phys.*, vol. 91, pp. 7977–7979, 2002.

[21] R. Dittrich, T. Schrefl, H. Forster, D. Suess, W. Scholz, J. Fidler, and V. Tsiantos, "Finite element simulation of discrete media with granular structure," *IEEE Trans. Magn.*, vol. 38, pp. 1967–1969, 2002.

[22] D. Suess, T. Schrefl, W. Scholz, J.-V. Kim, R. L. Stamps, and J. Fidler, "Micromagnetic simulation of antiferromagnetic/ferromagnetic structures," *IEEE Trans. Magn.*, vol. 38, pp. 2397–2399, 2002.

[23] H. Forster, T. Schrefl, R. Dittrich, D. Suess, W. Scholz, V. Tsiantos, J. Fidler, K. Nielsch, H. Hofmeister, H. Kronmller, and S. Fischer, "Magnetization reversal in granular nanowires," *IEEE Trans. Magn.*, vol. 38, pp. 2580–2582, 2002.

[24] T. Matthias, W. Scholz, J. Fidler, T. Schrefl, T. S. Rong, I. P. Jones, and I. R. Harris, "Sm(Co,Fe,Cu,Zr)$_z$ magnets for high-temperature applications: Microstructural and micromagnetic analysis," *IEEE Trans. Magn.*, vol. 38, pp. 2943–2945, 2002.

[25] W. Scholz, H. Forster, D. Suess, T. Schrefl, and J. Fidler, "Micromagnetic simulation of domain wall pinning and domain wall motion," *Comp. Mat. Sci.*, vol. 25, pp. 540–546, 2002.

[26] J. Fidler, T. Schrefl, V. D. Tsiantos, W. Scholz, and D. Suess, "Fast switching behaviour of nanoscopic NiFe- and Co-elements," *Comp. Mat. Sci.*, vol. 25, pp. 554–561, 2002.

[27] D. Suess, V. Tsiantos, T. Schrefl, J. Fidler, W. Scholz, H. Forster, R. Dittrich, and J. Miles, "Time resolved micromagnetics using a preconditioned time integration method," *J. Magn. Magn. Mater.*, vol. 248, pp. 298–311, 2002.

[28] J. Fidler, T. Matthias, W. Scholz, T. Schrefl, T. S. Rong, I. Jones, and I. R. Harris, "The role of the precipitation structure on the coercivity of Sm(Co,Fe,Cu,Zr)$_z$ magnets for ht applications," in *Proc. of XVII Rare Earth Magnets Workshop, University of Delaware* (G. Hadjipanayis and M. J. Bonder, eds.), pp. 853–860, 2002.

[29] T. Schrefl, H. Forster, J. Fidler, R. Dittrich, D. Suess, and W. Scholz, "Magnetic hardening of exchange spring multilayers," in *Proc. of XVII Rare Earth Magnets Workshop, University of Delaware* (G. Hadjipanayis and M. J. Bonder, eds.), pp. 1006–1026, 2002.

[30] T. Schrefl, J. Fidler, D. Suess, W. Scholz, and V. Tsiantos, "Micromagnetic simulation of dynamic and thermal effects," in *Advanced magnetic materials* (D. J. Sellmyer and D. Shindo, eds.), Springer-Verlag, 2002. in press.

[31] R. Dittrich, T. Schrefl, D. Suess, W. Scholz, H. Forster, and J. Fidler, "A path method for finding energy barriers and minimum energy paths in complex micromagnetic systems," *J. Magn. Magn. Mater.*, vol. 250, pp. L12–L19, 2002.

[32] H. Forster, T. Schrefl, W. Scholz, D. Suess, V. D. Tsiantos, and J. Fidler, "Micromagnetic simulation of domain wall motion in magnetic nanowires," *J. Magn. Magn. Mater.*, vol. 249, pp. 181–186, 2002.

[33] W. Scholz, T. Schrefl, and J. Fidler, "Micromagnetic simulation of thermally activated switching in fine particles," *J. Magn. Magn. Mater.*, vol. 233, pp. 296–304, 2001.

[34] T. Schrefl, W. Scholz, D. Suess, and J. Fidler, "Computational micromagnetics: Prediction of time dependent and thermal properties," *J. Magn. Magn. Mater.*, vol. 226-230, pp. 1213–1219, 2001.

[35] J. Fidler, T. Schrefl, D. Suess, and W. Scholz, "Dynamic micromagnetic simulation of the configurational anisotropy of nanoelements," *IEEE Trans. Magn.*, vol. 37, pp. 2058–2060, 2001.

[36] T. Schrefl, H. Forster, D. Suess, W. Scholz, V. D. Tsiantos, and J. Fidler, "Micromagnetic simulation of switching events," in *Advances in Solid State Physics 41* (B. Kramer, ed.), pp. 623–635, Springer Verlag, 2001.

[37] T. Schrefl, D. Suess, H. Forster, V. D. Tsiantos, W. Scholz, J. Fidler, and R. Dittrich, "Micromagnetic simulations and applications," in *Proc.*

5th Int. Workshop on Mathematical Methods in Scattering Theory and Biomedical Technology, pp. 141–158, World Scientific, 2001.

[38] J. Fidler, T. Schrefl, W. Scholz, D. Suess, and V. D. Tsiantos, "Micromagnetic simulation of magnetisation reversal in rotational magnetic fields," *Physica B: Condensed Matter*, vol. 306, pp. 112–116, 2001.

[39] V. D. Tsiantos, T. Schrefl, D. Suess, W. Scholz, J. Fidler, and J. M. Gonzales, "Micromagnetic simulation of magnetization reversal in Co/Ni multilayers," *Physica B: Condensed Matter*, vol. 306, pp. 38–43, 2001.

[40] J. Fidler, T. Schrefl, W. Scholz, and D. Suess, "Micromagnetic modelling and properties of nanocomposite magnets," in *Proc. of 22nd RISO Int. Symposium on Materials Science, Science of metastable and nanocrystalline alloys*, pp. 1–14, 2001.

[41] V. D. Tsiantos, T. Schrefl, D. Suess, W. Scholz, H. Forster, and J. Fidler, "Time integration methods in micromagnetic simulations: Stiffness on granular media-patterned media and μmag standard problem #4 - speed up of simulations," in *Proc. 5th Hellenic European Conference on Computer Mathematics & its Applications (HERCMA)* (E. A. Lipitakis, ed.), pp. 163–166, 2001.

[42] T. Schrefl, J. Fidler, D. Süss, and W. Scholz, "Hysteresis and switching dynamics of patterned magnetic elements," *Physica B: Condensed Matter*, vol. 275, pp. 55–58, 2000.

[43] W. Scholz, D. Suess, T. Schrefl, and J. Fidler, "Micromagnetic simulation of structure-property relations in hard and soft magnets," *Comp. Mat. Sci.*, vol. 18, pp. 1–6, 2000.

[44] W. Scholz, J. Fidler, D. Suess, and T. Schrefl, "Langevin dynamics of small ferromagnetic particles and wires," in *Proceedings of 16th IMACS World Congress on Scientific Computation, Applied Mathematics and Simulation*, 2000. in press.

[45] T. Schrefl, D. Suess, W. Scholz, and J. Fidler, "Finite element simulation of hard magnetic properties," in *Proc. PAMM Conference*, 2000. in press.

[46] T. Schrefl, J. Fidler, and W. Scholz, "Modeling and limits of advanced HT-magnets," *IEEE Trans. Magn.*, vol. 36, pp. 3394–3398, 2000.

[47] T. Schrefl, W. Scholz, D. Süss, and J. Fidler, "Langevin micromagnetics of recording media using subgrain discretization," *IEEE Trans. Magn.*, vol. 36, pp. 3189–3191, 2000.

[48] R. Groessinger, M. Kuepferling, A. Wimmer, M. Taraba, W. Scholz, J. Dudding, P. Lethuillier, B. Enzberg-Mahlke, W. Fernengel, and G. Reyne, "The pulsed field magnetometer – a tool for characterizing permanent magnets," in *Proc. XVI. Int. Workshop on Rare Earth Magnets and their Applications* (M. O. H. Kaneko, M. Homma, ed.), pp. 1129–1138, The Japan Institute of Metals, 2000.

[49] J. Fidler, T. Schrefl, W. Scholz, and D. Suess, "Rotational magnetization processes in meso- and nanoscopic magnets," in *Proceedings 6th Int. Workshop on 1&2-dimensional Magnetic Measurement and Testing* (H. Pfützner, ed.), pp. 163–171, 2000.

[50] W. Scholz, T. Schrefl, and J. Fidler, "Mesh refinement in FE-micromagnetics for multi-domain $Nd_2Fe_{14}B$ particles," *J. Magn. Magn. Mater.*, vol. 196-197, pp. 933–934, 1999.

Acknowledgment

The work on this thesis has been an inspiring, often exciting, sometimes challenging, but always interesting experience. It has been made possible by many other people, who have supported me.

I am very grateful to my supervisor Josef Fidler who has given me the chance to participate in several interesting research projects and attend various international conferences. He has supported me with his encouragement and many fruitful discussions. I would also like to express my sincere thanks to Thomas Schrefl for his invaluable experience and advice. The close cooperation with Thorsten Matthias, Dieter Süss, Hermann Forster, Rok Dittrich, and Vassilios Tsiantos as well as many other students was a great experience, which lead to many joint publications. The internship at Seagate Research in Pittsburgh was a unique experience and I would like to thank Roy Chantrell, head of the theory group, for this great opportunity.

Finally, I wish to thank my parents for their continuous support and encouragement.

Curriculum Vitæ

Werner Scholz

Lebenslauf

Werner Scholz